Dynamical coupling of plasma motions and neutral winds in the presence of short time-scale (10-90 min) wavelike structures in the auroral ionosphere

Shin-ichiro Oyama

Communications Research Laboratory

2001

Acknowledgments

I would like to express my gratitude for being able to undertake my doctor thesis in the Solar-Terrestrial Environment Laboratory (STEL) of Nagoya University, in particular to the members of the advisory committee, the chairman, Professor Ryoichi Fujii, Professor Gordon Rostoker, Professor Tadahiko Ogawa, and Associate Professor Hiroyuki Shinagawa.

I would like to thank the staff and students of STEL for their encouragement of my work on this thesis and to express my sincere appreciation to Professor Emeritus Nobuo Matuura, Dr. Satonori Nozawa, and Associate Professor Stephan Buchert who took time to help with data collection, and to complete the thesis. I also deeply appreciate the helpful discussions and encouragement of Dr. Mamoru Ishii, Dr. Yasuhiro Murayama, and Dr. Minoru Kubota of Communications Research Laboratory (CRL).

I would like to acknowledge the contributions of Professor Wlodek Kofman, Professor Jean Lilensten, Professor Chantal Lathuillere, Dr. Beatrice Pibaret, and Dr. Olivier Witasse of Laboratoire de Planetologie de Grenoble, France, for their helpful advice on how to complete the survey. Their friendly support during my stay in Grenoble, 1997, provides unforgettable memories.

I am indebted to the director and staff of the EISCAT for operating the facility and supplying data. EISCAT is an international association supported by Finland (SA), France (CNRS), the Federal Republic of Germany (MPG), Japan (NIPR), Norway (NFR), Sweden (NFR), and the United Kingdom (PPARC). My thanks are also due to the Finnish Meteorological Institute, for providing data from their all-sky auroral cameras and IMAGE magnetometers. This study was also supported in part by the U.S.-Japan International Research Project to Observe the Middle Atmosphere, CRL.

Finally, I would like to extend my heartfelt gratitude to my wife, Kyoko, daughter, Wakana, my mother, Kishiko Oyama, and my grand mother, Sumako Takesawa, for their kind help, without which I could not have completed this thesis.

Notation

General Notation

$\boldsymbol{E}$	electric field vector
$\boldsymbol{B}$	geomagnetic field vector
$\boldsymbol{g}$	gravitational acceleration vector
κ	Boltzmann constant ($= 1.38 \times 10^{-23}$ J/K)
q	electric charge
C	speed of sound
t	time
m	mass
N	number density
T	temperature
p	pressure

Specific Notation

$\boldsymbol{V}$	ion velocity vector
$\boldsymbol{U}$	neutral-wind vector
I	geomagnetic dip angle
Ω	gyrofrequency
ν	collision frequency

Subscript

e	electrons
i	ions
n	neutrals
$/\!/$	parallel to the geomagnetic field line

Abstract

Ions in the ionosphere drift through the process of the cross product of the electric and magnetic fields, momentum transfer from neutrals to ions through collisions, and diffusion caused by the pressure gradient mainly along geomagnetic field lines. At high latitudes, the electric field and precipitating particles originated in the magnetosphere significantly affect motions of ions. Motions of ions during geomagnetically active intervals can disturb those of neutrals in the auroral thermosphere through collisions between ions and neutrals. For example, wavelike structures in the motions of neutrals at oscillation periods from a few tens minutes to a few hours are generated by enhancements of plasma flow, or the electric field [*Hunsucker*, 1982 and references therein]. For more than four decades, wavelike structures such as gravity waves in the thermosphere have been the subject of many theoretical and experimental studies on thermospheric and ionospheric motions during auroral activity. There are, however, many unresolved aspects of the wavelike structures in the auroral ionosphere and thermosphere. Two of them are, (1) dynamical coupling of plasma motions and neutral winds in the presence of wavelike structures in short time-scale (10-90 min) in the auroral ionosphere, and (2) relationships between wavelike structures and ionospheric disturbances in association with auroral arcs. We conduct three analyses on these topics using data observed mainly with the European Incoherent Scatter (EISCAT) radar, a scanning Fabry-Perot interferometer (FPI), and an all-sky auroral camera:

- Dynamical coupling between oscillations of ions and neutrals in short time-scale from simultaneous observations between the EISCAT radar and the scanning FPI (λ = 630.0 nm),
- Statistical analysis of the ion velocity, along the geomagnetic field line, observed with the KST (Kiruna-Sodankylä-Tromsø) EISCAT radar and ESR (EISCAT Svalbard Radar),
- Relationship between wavelike structures and ionospheric disturbances in association with auroral arcs using data from simultaneous observations between the EISCAT radar and the all-sky auroral camera.

Field-aligned velocities of ions and neutrals in almost the same volume in the *F*-region have been obtained at the same time with the EISCAT radar and the scanning FPI during the night of 8 February 1997 at Tromsø, Norway. Our observation is the first experiment simultaneously using optical and radio techniques for targeting short-time-scale oscillations of ions and neutrals in the auroral *F*-region. In general, it is difficult to obtain optical data of sufficient quality, but the field-aligned velocities obtained during this campaign have good quality with

time-resolution of about 1.5 min and can be used to investigate dynamical coupling between oscillations of ions and neutrals in short time-scale. The summary of the EISCAT–FPI comparison is that the amplitude and the phase of $U_{//\mathrm{FPI}}$ have been correctly estimated using EISCAT radar data as long as the height range covered by EISCAT radar data in use overlaps the emission layer. It is concluded that the plasma oscillations observed with the EISCAT radar at different heights in the *F*-region are due to the motion of neutrals.

The main conclusion of the statistical study of the field-aligned ion motions using KST radar and ESR data is that diurnal variations in the field-aligned ion motion are likely driven by a large-scale pressure gradient of the temperature of neutrals. Sporadic/burst upward ion motions along geomagnetic field lines are observed during enhancements of southward electric field. Plasma diffusion velocities during large upward ion-motion events are significantly smaller than the magnitude of the observed upward velocity, which suggests that neutral winds in the *F*-region should strongly affect the generation of the large upward ion velocities. However, we do not yet understood the driving mechanisms of those upward ion motions and the relation between motions of neutrals and ionospheric heating caused by enhancement of the electric field.

The simultaneous observations using the EISCAT radar and the all-sky camera were conducted in northern Scandinavia on 1 March 1995 and revealed wavelike structures of the neutral-wind velocity in the auroral *F*-region and ionospheric disturbances in association with auroral arcs. Although we cannot find conclusive evidence that the observed oscillations are gravity waves (GWs), the wave parameters, such as frequency, phase, and wavelength, of observed oscillations are typical of those for medium-scale GWs according to *Hunsucker* [1982]. From the wave parameters, we estimate when and where the observed oscillations have been generated using the dispersion relation for GWs. Around the estimated position and time, the auroral arc extended in an almost zonal direction according to all-sky auroral images obtained at Kilpisjärvi. This implies that geomagnetic activity at high latitudes is important to generate GWs, as indicated by previous theoretical studies.

Contents

Chapter 1

General introduction

The terrestrial atmosphere is very thin compared with the radius of the solid earth. In this thin layer, there are many gaseous species, which are controlled to the first order by the gravitational force and are horizontally stratified. Height profiles of the temperature, concentration, and atmospheric motion have been investigated using theoretical calculations and various instruments, and it is found that the height profiles depend on solar and geomagnetic activity through complicated chemical reactions and dynamical coupling between neutrals and ions. At high latitudes, electromagnetic energy can penetrate from the magnetosphere to the ionosphere and the thermosphere by fluctuations in the electric field and particle precipitation. This energy directly affects thermospheric motions at high latitudes and indirectly at middle and low latitudes through propagation of neutral-wind wave action.

In this chapter, we focus on vertical structures of temperature and concentration in the thermosphere and the ionosphere. Dynamics in the thermosphere and ionosphere, mainly targeting on high-latitude phenomena, are explained using fundamental equations for the motions of ions and neutrals and results from previous observations.

1.1 Vertical structure of the thermosphere and the ionosphere

Figure 1.1a shows the height profile of the number density of the major gaseous species. Below and around altitudes of 100 km, the major species are molecules of nitrogen and oxygen. Above about 120 km, the concentration of atomic oxygen exceeds that of molecular oxygen. This is due to the photodissociation of molecular oxygen by solar extreme ultra-violet (EUV) and ultra-violet (UV) radiation. Atomic oxygen is the major species above about 200 km up to the region where light species such as helium and hydrogen become major components, above about 600 km.

Figure 1.1b shows the height profile of daily mean temperatures of neutrals in the ther-

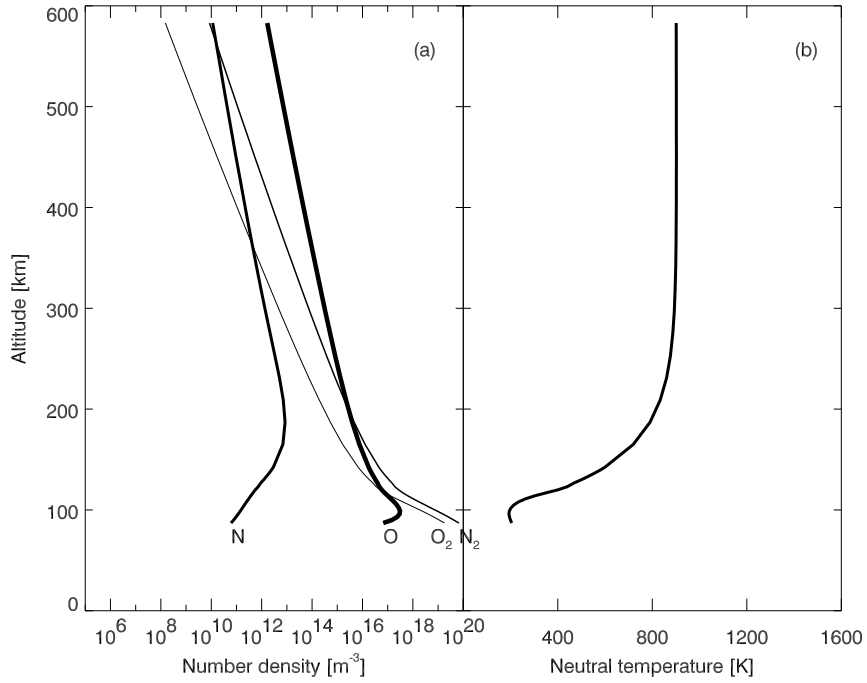

Figure 1.1: *Height profile of (a) the density and (b) temperature of neutral gases above Tromsø on 29 March, 1995, as calculated using the MSIS model [Hedin, 1991].*

mosphere, above Tromsø, Norway (69.6° N, 19.2° E), calculated using the Mass Spectrometer and Incoherent Scatter (MSIS) neutral atmosphere model [*Hedin*, 1991]. The temperature varies more dramatically in the vertical direction compared to the horizontal one. The height gradient in the temperature is positive in the thermosphere. It gradually decreases with height becoming negligibly small above about 200 km. The temperature profile is significantly dependent on solar activity. Effects of the solar activity seem to appear clearly in the upper rather than the lower thermosphere [*Roble and Emery*, 1983].

The major heat source in the thermosphere is absorption of solar EUV and UV radiation (in the range 130 nm $< \lambda <$ 175 nm) through the photodissociation of molecular oxygen and photoionization. Atomic oxygen produced by photodissociation moves downward through thermal diffusion due to the positive height-gradient in the thermospheric temperature. Atomic oxygen diffuses into the lower thermosphere and changes to molecular oxygen through three-body recombination. Three-body recombination releases the thermal energy into the neutral atmosphere and thus contributes to the heat balance in the lower thermosphere and the upper mesosphere.

While the airglow and auroral emission dissipate energy into the thermosphere by radiating at visible wavelengths (in the range $\sim$400 nm $< \lambda <$ $\sim$800 nm), the major loss process in the thermosphere involves infrared radiation, in particular, at wavelength of 5.3 μm from nitric oxide above 120 km height. The dissipation of tidal motions and gravity waves

is a minor heat source in the upper thermosphere, but is important in the lower thermosphere and the mesosphere, not only as a heat source but also as a source of momentum.

At high latitudes, the electromagnetic energy deposited into the ionosphere from the magnetosphere is an additional and important heat source for dynamics and chemical reactions in the thermosphere. The electric field originating in the magnetosphere varies greatly with time and space depending on geomagnetic conditions. Charged particles drift perpendicular to geomagnetic field lines through the process of convection at velocities defined by the cross product of the electric and magnetic fields. This process increases the relative velocities of charged and neutral particles and thus the frictional energy. The frictional energy is dissipated to ions and neutrals at the same time through collisions but unequally because the density of neutrals is much larger than that of ions. Incoherent Scatter (IS) radars at high latitudes frequently observe ion temperature enhancements (> 1000 K) during electric-field enhancements. Dynamic Explorer 2 satellite observed significant enhancements of the temperature of neutrals (> 200 K) at an altitude about 350 km [*Spencer et al.*, 1982], but ground-based instruments scarcely observe such large increases in the temperature of neutrals. Quantitative relationships between temperature of ions and neutrals during geomagnetically disturbed intervals are an important subjects of experimental and theoretical studies to understand the thermosphere-ionosphere dynamical coupling at high latitudes.

The vertical structure of the ionosphere is mainly described by the ion continuity equation, which involves three principal mechanisms; transport, production (P), and loss (L) through the process of recombination of positive ions and electrons:

$$\frac{\partial N_i}{\partial t} = -\nabla(N_i \boldsymbol{V}) + P_i - L_i. \tag{1.1}$$

The major contributor to production is photoionization by solar EUV and UV radiation. The altitude at which the plasma density has its peak tends to be the F-region (150-300 km). At high latitudes, however, the region can be shifted downward into the E-region (90-120 km) during enhancement of precipitation of auroral particles in an energy range approximately from 1 to 20 keV. Relative to the ionization induced by cosmic rays, which has a diurnal variation, the effects of auroral precipitation are unpredictable and are dependent on geomagnetic activity, particularly in the E-region.

The ion pressure gradient along geomagnetic field lines transports ions, which is the principal process in the upper ionosphere, whereas the processes of ionization and recombination are insignificant. All three processes contribute to the vertical structure in the F-region. In the E-region, the transport process is insignificant compared with the other two processes.

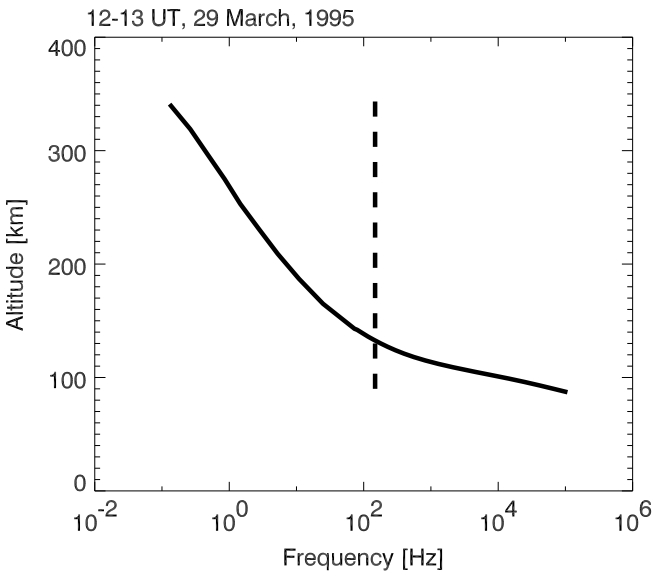

Figure 1.2: *The height profile of the ion-neutral collision frequency (solid line) above Tromsø. Also indicated, for comparison, is the ion gyrofrequency (dashed line).*

1.2 Ionospheric and thermospheric dynamics in the auroral region

Dynamic coupling between thermosphere and ionosphere can be characterized by the collision frequency between ions and neutrals. The frequency is a function of the density of neutrals and thus of altitude. In the ionosphere, the momentum of neutrals can be transferred to ions within a second. On the other hand, the time constant for the transfer of the momentum of ions to neutrals is comparatively long but does have an effect on the motions of neutrals, especially in the auroral *F*-region. Effects of the force through the collision process as well as other forces on motions of ions are expressed by the ion momentum equation.

1.2.1 Fundamental equation for the motions of ions and neutrals

The ion momentum equation that is used in this thesis is

$$m_i N_i \frac{d\boldsymbol{V}}{dt} = -\nabla p_i + m_i N_i \boldsymbol{g} + q_i N_i \left(\boldsymbol{E} + \boldsymbol{V} \times \boldsymbol{B}\right) - m_i N_i \nu_{in} (\boldsymbol{V} - \boldsymbol{U}). \tag{1.2}$$

The average mass and the density of ions are respectively given by

$$m_i = \frac{\sum_j m_j N_j}{\sum_j N_j}, \tag{1.3}$$

and

$$N_i = \sum_j N_j, \tag{1.4}$$

where j stands for ion species. The left-hand side of Eq. (1.2) is the rate at which momentum is exchanged in a volume with a given ion density. The first term on the right-hand side is the force due to the ion pressure gradient. The external forces on ions are the gravitational force and the electric and magnetic forces, represented by the second and the third terms on the right-hand side, respectively. The last term on the right-hand side represents the momentum transfer through collisions between ions and neutrals. As long as the time scale under consideration is longer than ν_{in}^{-1}, the left-hand side can be neglected and then Eq. (1.2) may be expressed as,

$$\boldsymbol{U} = \boldsymbol{V} - \frac{1}{m_i N_i \nu_{in}}(-\nabla p_i + m_i N_i \boldsymbol{g}) - \frac{\Omega_i}{B\nu_{in}}(\boldsymbol{E} + \boldsymbol{V}\times\boldsymbol{B}). \tag{1.5}$$

The geomagnetic field-aligned neutral-wind velocity, $U_{//}$, can be obtained from the field-aligned ion velocity, $V_{//}$, and the diffusion and ambipolar diffusion velocities [*Winser et al.*, 1988 and references therein]:

$$U_{//} = V_{//} - \frac{g\ sin\ I}{\nu_{in}} - \frac{\kappa}{m_i N_i \nu_{in}}\frac{\partial}{\partial s}[N_i(T_i + T_e)]. \tag{1.6}$$

Variations in the gyrofrequency with height are smaller than those in the ion-neutral collision frequency, which decreases exponentially with height (Fig. 1.2). Below about 120 km, the ion-neutral collision frequency is higher than the gyrofrequency: on average, ions will collide with neutrals more than once within a single gyration around a geomagnetic field line. Above about 120 km, the ion-neutral collision frequency is lower than the gyrofrequency.

Figure 1.3 suggests that this boundary height seems to depend on the magnitude of the electric field [*Fujii et al.*, 1998]. When a strong electric field is present (E > 25 mV/m), ions move almost perpendicular to geomagnetic field line above about 117 km. When the electric field is weak (5 mV/m < E < 10 mV/m), neutrals tend to drag ions horizontally through collisions in the whole *E*-region, and even in the *F*-region. We can use Eqs. (1.5) and (1.6) to obtain the neutral-wind velocity throughout the ionosphere. However, there are some caveats on using these equations to estimate neutral-wind velocities. They are discussed in the following subsections for the *E*- and *F*-regions.

1.2.2 *E*-region

The high ion-neutral collision frequency allows us to ignore the pressure and gravitational terms of Eq. (1.5) [*Rino et al.*, 1977] and obtain

$$\boldsymbol{U} = \boldsymbol{V} - \frac{\Omega_i}{B\nu_{in}}(\boldsymbol{E} + \boldsymbol{V}\times\boldsymbol{B}). \tag{1.7}$$

This equation has been used to derive the neutral-wind velocity at a few altitudes in the *E*-region on the basis of data from tristatic measurements made with the European Incoherent

Figure 1.3: *Distributions in the angle between the velocity vector for the ions and the geomagnetic field line, at different altitudes (after Fujii et al., 1998).*

Scatter (EISCAT) radar [e.g. *Nozawa and Brekke*, 1999]. Because in the *E*-region the ion-neutral collision frequency is much larger than the ion gyrofrequency, the second term on the right-hand side of Eq. (1.7) is smaller than the first term but can not be ignored. During geomagnetically disturbed periods, the electric field originating in the magnetosphere can penetrate into the *E*-region along geomagnetic field lines, and it accelerates ions perpendicular to geomagnetic field lines; then neutrals are set in motion through collisions with ions. The diffusion and ambipolar diffusion velocities in Eq. (1.6) are significantly smaller than the field-aligned ion velocity in the *E*-region, so that $U_{//} = V_{//}$. The field-aligned component of the neutral-wind velocity is estimated from that of the ion velocity. The ion-neutral collision frequency is not needed, and the approach is thus not dependent on any neutral atmospheric models.

1.2.3 *F*-region

In the auroral *F*-region, the ion drag force due to the electric field can play an important role in controlling dynamics of neutrals. This suggests that the second and third term on the right-hand side of Eq. (1.5) should be considered in deriving the neutral-wind velocity. The magnitude of the last term of Eq. (1.5) is frequently larger than that of the first term above about 110 km, during enhancement of the electric field. Discrepancies between real and modeled neutral atmospheric parameters cause significant ambiguities in the ion-neutral collision frequency and thus in the neutral-wind velocity calculated using Eq. (1.5). Although the diffusion and ambipolar diffusion velocities in Eq. (1.6) are functions of the ion-neutral collision frequency, the field-aligned neutral-wind velocity derived from Eq. (1.6) depends very little on neutral atmosphere models because the magnitude of the diffusion velocities are generally smaller than those of the field-aligned ion velocity below heights of about 300 km. Equation (1.6) has been used to estimate the neutral-wind velocity in the *F*-region [e.g. *Lilensten et al.*, 1992; *Oyama et al.*, 2000].

1.2.4 Observational and modeled results for thermosphere-ionosphere dynamics

Global phenomena in thermospheric motions.
One of the fundamental mechanisms in atmospheric dynamics is the meteorological concept of geographic balance. An approximate balance between the pressure gradient of neutrals and the Coriolis forces exists, especially in the upper troposphere and the mesosphere, as shown in Fig. 1.4. The horizontal pressure gradient is mainly caused by differences in the absorption of solar EUV and UV radiation. The zonal averages of the temperature of neutrals and mean molecular mass, as a first approximation, gradually decrease from the summer pole to the winter pole except during equinox [*Roble et al.*, 1977]. This indicates that an average zonal summer-to-winter meridional flow should develop in response to the pressure gradient between the poles, even though this meridional flow would diverge from the equator to the poles at the noon meridian.

The summer-to-winter meridional flow that arises from the pressure gradient between the poles is deflected by the Coriolis force, which would be expected to result in a westward flow in the summer hemisphere and an eastward flow in the winter hemisphere. The wind system in the mesosphere is a consequence of the balance between the pressure gradient and the Coriolis force [*Manson and Meek*, 1984; *Tetenbaum et al.*, 1986; *Avery et al.*, 1989; *Manson et al.*, 1989]. The results of observations of the lower thermosphere, however, clearly show an intervening region from 90 to 120 km [*Manson et al.*, 1981; *Johnson et al.*, 1987; *McLandress*, 1998; *Nozawa and Brekke*, 1999]. In this region, the mean direction of the zonal winds changes so that it is eastward in the summer hemisphere and westward in the winter

Figure 1.4: *A schematic drawing of the dynamic balance at different levels of the thermosphere. U is the neutral-wind velocity vector, ∇P is the pressure vector of neutrals, C is the Coriolis force, and I is ion drag. The pressure of neutrals in region L is lower than that in region H.*

hemisphere, but reverts back above 120 km. This reversal of the mean zonal flow is believed to result from the deposition of momentum from gravity waves and tides in the mesosphere and the lower thermosphere, though the horizontal scales of these reversed flows are much less than the scales of those flows which dominate the general circulation [*Garcia and Solomon*, 1985].

Effects of ion drag on thermospheric motions at high latitudes.

In the upper thermosphere, ion drag affects the dynamics of neutrals through a so-called fly-wheel process. If the ion drag is greater than the Coriolis force, the neutral-wind vector is approximately parallel to the force produced by the pressure gradient, as shown in Fig. 1.4. Thermospheric general circulation models show that, at the boundary of the polar cap, ions tend to flow against the pressure gradient while neutrals seem to respond to the pressure gradient force [*Killeen and Roble*, 1984]. The meridional neutral-wind velocity in the upper thermosphere is poleward in the daytime and equatorward in the nighttime, throughout the year [*Witasse et al.*, 1998]. The equatorward component of the mean meridional neutral-wind in summer is greater than that in winter. These results suggest that the diurnal tide in the upper thermosphere is generated mainly by the pressure gradient between the day- and night-side as well as by the gradient between the summer and winter poles.

At high latitudes, ion drag is no longer a sink for momentum in the upper thermosphere, or even in the lower thermosphere. The neutral-wind system in the upper thermosphere responds primarily to the momentum transfer from ions to neutrals that is associated with magnetospheric convection [*Killeen and Roble*, 1988 and references therein]. The neutrals move antisunward within the geomagnetic polar cap and sunward on the equatorward side of

the polar cap in the auroral zone (Fig. 1.5). Because the pattern of ion-convection strongly depends on the interplanetary magnetic field (IMF), the sensitivity of the neutral-wind system to the magnitude and orientation of the IMF has been the subject for several investigations [*Killeen et al.*, 1985; *McCormac et al.*, 1985; *Rees et al.*, 1986; *Thayer et al.*, 1987].

Ions moving perpendicular to geomagnetic field lines almost immediately respond to changes in magnitude and orientation of the electric field. There is, however, a considerable time lag before the neutral-wind velocity responds to such changes; this case is close to an inertial response [*Killeen et al.*, 1985]. The neutral-wind signatures resemble those of the ion velocities with, however, a reduction in magnitude and with much less evidence of spatial structure. The discrepancy between velocities of ions and neutrals results in enhancement of the frictional energy dissipation and thus of the ion temperature. Figure 1.6 shows that large relative velocities between ions and neutrals occur in the dawnside region, where the ion flow is sunward and neutrals reverse from antisunward to sunward [*Killeen et al.*, 1984]. It is obvious that the ion temperatures in this region will be increased. Numerical simulation of the thermospheric dynamics shows that enhancement of the frictional energy dissipation drives upwelling motions that are associated with the strong equatorward flow [*Richmond and Matsushita*, 1975; *Hajkowicz and Hunsucker*, 1987; *Fujiwara et al.*, 1996]. *Spencer et al.* [1982] showed that the neutral-wind velocity had a strong vertical component, reaching 100-150 m/s at times, and this was accompanied by temperature perturbations of neutrals of about 300 K.

Thermospheric motions during auroral activity – wavelike structures

Observations with various instruments at auroral *E*- and *F*-region heights frequently show wavelike structures, at periods from a few tens of minutes to a few hours, in ionospheric parameters. These waves have been studied both experimentally and theoretically since publication of *Hines*' [1960] landmark paper using the dispersion relation for gravity waves (GWs) (see Appendix A).

There are many probable sources for generating GWs in the atmosphere, both artificial (nuclear explosions, spacecraft launch, *etc.*) and natural (auroral phenomena, tropospheric turbulence, mountains, *etc.*). At high latitude, enhancement of the frictional energy dissipation as well as heating caused by precipitation of highly energetic particles and rapid motions in the aurora are believed to be significant sources of GWs [*Chimonas and Hines*, 1970; *Francis*, 1974; *Walterscheid and Lyons*, 1992; *Bristow et al.*, 1994, 1996; *Sun et al.*, 1995].

Perturbations in the electrojet current result in fluctuations in the amount of energy dissipated by friction and action of the Lorentz force. HF radars frequently observe wavelike structures in ground-scatter echoes, which are thought to be caused by the neutral atmospheric pressure-variations because the GWs couple to the bottomside ionosphere [*Samson et al.*, 1990; *Bristow et al.*, 1994, 1996; *Sofko and Huang.*, 2000]. Most of the observed

GWs reported in these papers are thought to be generated by auroral sources, mainly by enhancements of auroral electrojet current. *Bristow et al.* [1996] report that different HF radars simultaneously observed equatorward propagating GWs that extended along the zonal direction for about 1/6 of the Earth's circumference at 60° latitude.

Theoretical analyses have led to the conclusion that auroral activity can cause GWs through thermal expansion and ion drag [*Chimonas and Hines*, 1970; *Francis*, 1974; *Walterscheid and Lyons*, 1992; *Sun et al.*, 1995; *Fujiwara et al.*, 1996]. The wave front generated mainly by thermal expansion due to the Joule heating propagates toward low latitudes with a velocity slightly less than the local sound speed at each height. After equatorial crossing, the waves continue to propagate poleward, and then dissipate as they reach the polar regions [*Fujiwara et al.*, 1996]. Wavelike structures generated at high latitudes propagate both meridionally and zonally. However, the zonal propagation rate is relatively small compared with the meridional propagation rate [*Sun et al.*, 1995; *Fujiwara et al.*, 1996].

The relative importance of Lorentz and frictional effects in the generation of GWs has also been investigated [*Chimonas and Hines*, 1970; *Brekke*, 1979; *Balthazor et al.*, 1997]; it is, however, not yet fully understood [*Williams et al.*, 1998].

The energetic precipitating particles that produce increases in ionization also deposit heat in the thermosphere through ion recombination. The heating rate by particle precipitation can be greater than that by frictional energy dissipation in the polar thermosphere [*Banks*, 1977; *Wedde et al.*, 1977]. While the effects of particle precipitation in GW generation have not yet been modeled theoretically, they certainly cannot be ignored at high latitudes.

The effects of moving sources on GW generation were investigated theoretically, on the assumption of auroral arcs moving rapidly [*Swift*, 1973; *Kato et al.*, 1977]. GWs are apparently produced when arcs expand poleward and subsequently move equatorward [*Wilson*, 1972].

Some of the wavelike structures observed in the auroral thermosphere and ionosphere are almost certainly generated above about 100 km height, as mentioned above. Others, however, can be generated near ground level by meteorological sources. Some statistical analysis on observational probability of the medium-scale traveling ionospheric disturbances (TIDs) at high latitudes suggest that the medium-scale TIDs appear quite often during geomagnetically quiet periods rather than during disturbed ones [*Evans et al.*, 1983; *Ogawa et al.*, 1987]. *Evans et al.* [1983] found no evidence for a K_p dependence of the incidence or amplitude of the medium-scale TIDs at middle latitudes. *Bertin et al.* [1975] report that sources to generate some of the medium-scale TIDs observed at middle latitudes are located in a geographic area in the vicinity of a weather disturbances associated with depressions. It is, in general, difficult to identify the source of the wavelike structures because of the lack of complete measurements of the neutral wind in the troposphere, stratosphere, and mesosphere.

The background dynamical conditions affect the gravity wave-activity (the incidence and the amplitude) and the propagation and attenuation processes. *Whiteway et al.* [1997] suggest that the gravity wave-activity is a maximum within the eastward jet at the edge of the stratospheric polar vortex, and a minimum near the center of the vortex.

Thermospheric motion during auroral activity – vertical motions of ions and neutrals

Several techniques, such as satellite, sounding rocket, and IS radar, frequently observe upward motions of ions in the polar ionosphere, which is called ion upflow [*Yau and André*, 1997 and references therein]. Neither characteristics of the ion upflow/downflow not its driving mechanisms, however, have been understood fully as yet. For example, it is still an open question as to how the ion upflow in the topside ionosphere relates to the ion outflow observed in the magnetosphere [*Abe et al.*, 1993]. It is also not, as yet, known whether the neutral wind plays a substantial role in driving the ion upflow/downflow.

Recent observations of the vertical wind velocity with a Fabry-Perot Interferometer (FPI, λ = 630.0 nm) show that vertical motions of neutrals in the auroral thermosphere are more dramatic than those predicted by theoretical calculations [*Rees et al.*, 1984; *Conde and Dyson*, 1995; *Price et al.*, 1995; *Smith and Hernandez*, 1995; *Innis et al.*, 1997; *Smith*, 1998]. *Conde and Dyson* [1995] show their data in a histogram which indicates that most observations at Mawson, Antarctica fall within 30 m/s of zero even when K_p is higher than 3.0. Conversely, about 1 % of all observations were more than 75 m/s different from zero, which suggests that vertical winds of more than 75 m/s were very rare. On the contrary, *Innis et al* [1997] report that large vertical winds (up to $\simeq$ 80 m/s) at Mawson are not associated with high geomagnetic activity.

1.3 Purpose of this thesis

In this thesis, we investigate two aspects of the thermosphere-ionosphere coupling at high latitudes; ion-neutral interaction and the effects of auroral activity on the motion of neutrals.

The ion momentum equation should describe the underlying theoretical process for all interactions between motions of ions and neutrals. Neutral winds estimated from IS radar data using the ion momentum equation agree fairly well with the results from simultaneous observations that were made with optical instruments, at least in terms of long-term tides [*Rees et al.*, 1984; *Wickwar et al.*, 1984; *Lilensten et al.*, 1992]. However, in terms of short-time-scale oscillations in the neutral wind (10-90 min), there are significant discrepancies between simultaneous observations with the two types of instruments. Results from numerical calculations also agree fairly well with those from observations with IS radars in terms of long-time-scale tides, but again there are discrepancies in terms of short-time-scale oscillations [*Johnson and Virdi*, 1991; *Killeen et al.*, 1991; *Lilensten and Lathuillere*, 1995].

There are at least two candidate explanations of the discrepancies in the short time-scale

oscillations observed with IS radars and optical instruments; (1) horizontal and/or vertical shears of the neutral-wind velocity in the field-of-view of the both instruments, and (2) fluctuations in the altitude of the peak emission rate and in the full width half maximum of the emission layer in association with fluctuations in the energy flux of the precipitating electrons. Discrepancies caused by explanation (1) may become serious for the comparison of short-time-scale oscillations when the field-of-view covered with the IS radar differs considerably from the field-of-view of the optical instrument. To make those discrepancies in explanations (1) and (2) small for simultaneous observation, we should make the field-of-view of both instruments the same in order to monitor almost the same volume and estimate height regions integrated with the optical instrument using the height profile of the emission rate calculated from ionospheric data acquired with the IS radar. To investigate the dynamic coupling between ions and neutrals in the presence of short-time-scale wavelike structures, especially along geomagnetic field line in the auroral *F*-region, we used data simultaneously obtained with two independent instruments; the EISCAT UHF radar and a scanning FPI, during the night of 8 February 1997, at Tromsø, Norway. Our observation is the first simultaneous experiment using optical and radio techniques for targeting short-time-scale oscillations of ions and neutrals in auroral *F*-region heights. In general, it is difficult to obtain optical data with sufficient quality, but field-aligned velocities obtained during this campaign have good quality with a time resolution of about 1.5 min and can be used to investigate dynamical coupling between oscillations of ions and neutrals on the short time-scales (Chapter 3).

Because the magnetic dip-angle at high latitudes is close to 90° (*e.g.*, $\simeq 78°$ at Tromsø), field-aligned motions of ions induced by vertical motions of neutrals through collisions have almost the same magnitudes as the vertical velocities of neutrals. The EISCAT radar frequently observes large amplitudes of field-aligned ion velocity at the *F*-region heights, which may relate to the generation of ion upflow. Field-aligned neutral-wind velocities from the EISCAT radar-FPI simultaneous observation also show relatively large amplitudes ($\simeq$ 25 m/s) in the presence of short-time-scale wavelike structures. We investigate the effects of auroral activity on the field-aligned ion velocities using data using the KST (Kiruna-Sodankylä-Tromsø) radar and ESR (EISCAT Svalbard radar) (Chapter 4).

Enhancement of the electromagnetic energy dissipated in the polar thermosphere is considered to disturb local motions of neutrals through a process of thermal expansion. This is one of the sources of GWs, and theoretical investigations of the relationship between auroral activity and the generation of GWs have been undertaken, as mentioned in Section 1.2.4. It may, however, be difficult to use the results of previous model-based calculations to estimate the response to such increases in terms of thermospheric motion. This is because peaks in the distribution of electromagnetic energy assigned in the models are more widely distributed than the scale of actual auroral arcs and last longer than the typical life-time of an actual arc. The simultaneous observations of motions of neutrals and knowledge of auroral morphology

are necessary for a proper investigation of this response, and for testing hypotheses on the relation between GWs and auroral activity.

An investigation of the effects of geomagnetic activity on wavelike structures in motions of neutrals at *F*-region heights, using data from the EISCAT radar and an all-sky auroral camera at Kilpisjärvi, Finland (69.0° N, 20.8° E), is also presented as part of this thesis. In particular, we focus on identifying the region in which observed wavelike structures were generated (Chapter 5).

Figure 1.5: *Neutral wind and ion velocity vectors observed with instrumentation on Dynamics Explorer 2. The neutral-wind velocity vectors are drawn as yellow arrows, and the ion ones as red bars. The curved lines represent the location of the solar terminator. The symbol S indicates the location of the invariant pole (after Killeen et al., 1984).*

Figure 1.6: *Geophysical observables measured along the track of DE2 during orbit 1161. The ion and neutral-wind velocities are shown in the top two traces plotted against time, and the altitude and latitude of the spacecraft. The second panel shows the temperatures of electrons, ions, and neutrals measured along the track, and the third panel shows the atomic oxygen, molecular nitrogen, and electron number densities. The bottom panel shows the ion-neutral coupling time constant measured along the track (after Killeen et al., 1984).*

Chapter 2

Instrumentation and data

Data used in this thesis are mainly from the EISCAT radar, the scanning FPI, and the all-sky auroral camera.

The geographic positions and operating parameters of the KST (Kiruna-Sodankylä-Tromsø) EISCAT radar and ESR (EISCAT Svalbard Radar) facility are given in Table 2.1. There are two independent radars at the KST radar site; a tristatic UHF radar and a monostatic VHF radar. The transmitters for both radars are at Ramfjordmoen, near Tromsø, Norway. The receivers for both radars are at the Tromsø radar site. For the UHF radar, there are additional receivers at Kiruna, Sweden, and Sodankylä, Finland. *Folkestad et al.* [1983] have outlined technical characteristics of the system and the procedures designed for preparing and running experiments. The principles of the incoherent scatter spectrum are described in Appendix B. CP-1L is an observational mode of the ESR that also uses a fixed transmitting direction along the geomagnetic field line at Longyearbyen to measure electron density, electron and ion temperatures and velocity along the radar beam as functions of altitude, but no electric field measurements are made.

The EISCAT radar is in operation for more than 1500 hours a year. These operations are categorized as either of two types; Special Program (SP) or Common Program (CP). The SP is designed by scientists of the EISCAT Association for the study of particular phenomena in the polar ionosphere. The CP is designed for the development of a long-term data base. It is usually scheduled to run for more than 24 hours at a time. There are currently seven CPs for KST radar observations, CP-1 to CP-7.

CP-1 observations provide values of ionospheric parameters – the electron density, ion and electron temperatures, and the ion velocity – along geomagnetic field lines from an alternating-code signal-modulation, which covers the region from 86 to 268 km with an altitude resolution of about 3 km, and from a long pulse which covers the region from 146 to 586 km with an altitude resolution of about 22 km. The data set used in this thesis is from CP-1.

Table 2.1: *Parameters of the EISCAT radar*

Location	**Tromsø**		**Kiruna**	**Sodankylä**	**ESR**
Geographic coordinates	69.6° N		67.9° N	67.4° N	78.1° N
	19.2° E		20.4° E	26.6° E	16.0° E
Geomagnetic inclination	77.5° N		76.8° N	76.7° N	82.1° N
Invariant latitude	66.2° N		64.5° N	63.6° N	75.2 ° N
Band	VHF	UHF	UHF	UHF	UHF
Center operating frequency (MHz)	224	931	931	931	500
Max. bandwidth (MHz)	3	8	8	8	10
Channels	8	8	8	8	6
Peak power (MW)	2×1.5	1.5	–	–	0.5
Average power (MW)	2×0.14	0.28	–	–	0.125
Pulse duration (ms)	0.001∼2.0	0.001∼1.0	–	–	0.001∼2.0
Gain (dB)	43.1	48.1	–	–	42.5
System temperature (K)	250-350	90-110	30-35	30-35	80-85

The scanning-type FPI was developed by Communications Research Laboratory, CRL, and details on the design of the FPI are given by *Ishii et al.* [1997]. The FPI has a full-view angle of 1.4°, which is almost the same as the full-power beam width of the EISCAT UHF antenna (about 1.2°). The FPI simultaneously measured auroral emissions at wavelengths of 557.7 nm (green-line) and 630.0 nm (red-line) using a dichroic mirror to divide the incident auroral light to follow two separate paths. The fringe images obtained with the FPI were integrated over 60 sec. in this study. It took about 30 sec. to transfer each image from the instrument to a hard disk, so the neutral-wind velocity was obtained roughly every 90 sec. The principles of the FPI are outlined in Appendix C.

The FPI etalon is very sensitive to temperature and humidity. Variations in temperature and humidity in the room where it is sited cause variations in the width of the etalon gap, which in turn induce false drifts in the neutral-wind velocity. To determine the artificial drift, we calculated a running-average of the squared radius of the fringe over two hours. The drifts tend to have a comparatively long oscillation period of a few hours. We assumed that the effects of the etalon gap were negligible after subtracting the running-averaged data from measured data.

Doppler shifts due to the neutral-wind velocity cause variations of the fringe radius, however do not, in theory, change the center position of the fringe, as long as there are no horizontal gradients in the motion of neutrals and auroral intensity in the volume that the

FPI is observing. Thus, the radius of the fringe should not have any dependence on azimuth. We have assumed that the neutral-wind velocity can be derived from the FPI observations by averaging the Doppler shift over azimuth. However, some observed fringes displayed a significant variation in radius over azimuth, and this increased the statistical and systematic deviations in the measured neutral-wind velocity. The variation in the radius might have been caused by a horizontal gradient in the intensity of that part of the aurora in the field-of-view of the FPI. Considering the variations in radius of the observed fringes, we assumed that integration over about 7 min (corresponding to five fringes) would be enough to derive the neutral-wind velocity. The neutral-wind velocities from the original fringe obtained about every 90 sec were computed using a running-average over five data points.

Chapter 3

Effects of atmospheric oscillations on the field-aligned ion motions

3.1 Introduction

In this chapter, the focus is on interactions between ionosphere and thermosphere, and in particular on the comparison of the field-aligned oscillations of neutrals in the F-region with oscillation periods from 14 to 55 minutes derived independently with the EISCAT UHF radar and the scanning FPI at Tromsø. Section 3.2 describes the data set. Section 3.3 describes the model for calculation of the auroral red-line emission rate ($\lambda = 630.0$ nm) and the two methods we used to interpret the neutral-wind velocity. Section 3.4 describes the observational results. The processes involved in the momentum transfer between ions and neutrals are discussed in Section 3.5.

3.2 Data

Over the period of observation, from January 11 to February 13, 1997, the scanning-type FPI was installed at the EISCAT radar site in Tromsø. The FPI was fixed to look along the geomagnetic field line at Tromsø during the night of February 8, as was the EISCAT UHF antenna. The same approximate cross-section in the layer of auroral red-line emission was thus monitored by both instruments. When comparing data from these simultaneous observations, we do not need to make any assumptions about the horizontal or vertical components of neutral wind because both instruments looked along the same field line at almost the same full-view angle. We were focusing on the motions of neutrals in the F-region, so we used red-line emission data from the FPI.

In general, the red-line emission occurs at altitudes from about 150 to 350 km, so we used EISCAT radar data from this height range. There are, however, some caveats when

EISCAT radar data are used. The first gate of the long pulse, at 143 km for this observational mode, might give biased ionospheric data, because the altitude gradient of the electron density is frequently steep over the range covered by the first-gate pulse. There were a few gaps in EISCAT radar data from the long-pulse code at altitudes higher than 297 km due to the low SN ratio of the IS spectrum. Data from the alternating code signal at altitudes between 150 and 160 km had large fitting errors. We thus used data for altitudes from 165 to 275 km; that is, from six gates.

With an increase in geomagnetic activity, we would expect an increase in the input of energy from the magnetosphere to the ionosphere. This increase enhances the vertical motion of neutrals, which may alter the height profile of ion composition. It is thus more difficult to derive the ion and electron temperatures and the electron density from IS spectra during geomagnetically disturbed intervals than during geomagnetically quiet ones.

The intensity of the red-line emission was measured using a photometer with a narrow view angle, 2°. The photometer was also fixed to look along the geomagnetic field line. The integration time was 0.1 sec. While there was a small discrepancy in the view angle, the volume observed with the photometer was assumed to be almost the same as the volume observed with the other instruments.

3.3 Analysis

The neutral-wind velocity along the geomagnetic field line is given by Eq. (1.6). The MSIS model [*Hedin*, 1991] was used to estimate ν_{in}. The ion composition model used to derive N_i, T_i, T_e, and $V_{//}$ from the EISCAT radar spectrum was used to estimate m_i.

The results of *Strickland et al.* [1989] were used to calculate the red-line emission rate on the basis of data from the EISCAT radar and the MSIS model. The two major processes by which $O(^1D)$ is produced are assumed to be the excitation of atomic oxygen by electron impact and the dissociative recombination of molecular oxygen ions. The emission rate due to electron impact is proportional to the electron precipitation flux. The flux in the energy range from 10 eV to 10 keV has been estimated using a model equation [*Meier et al.*, 1989]. To determine the characteristic energy and total energy flux, the least squares method was used to fit the model flux to the flux derived from a method for calculating spectra from the height profiles of electron density observed with the EISCAT radar. We used the CARD method [*Brekke et al.*, 1989] to estimate the incident energy spectra of precipitating electrons. Least squares fitting was performed over the energy range from 2 keV to 10 keV.

Meier et al. [1989] obtained relatively good agreement between the computed height profile of ion and electron densities and the height profile observed with a rocket. The model densities were calculated with ionization due to primary and secondary electrons taken into account. The electron transport model used was described by *Strickland et al.* [1976].

The relatively good agreement that was found suggests that ionization due to primary and secondary electrons is the major process involved in producing electrons, and this ionization is directly related to the emission rate. The emission rate model thus included the effects of both primary and secondary electrons.

The altitude resolution of FPI data is inevitably limited by the shape of the emission profile. The field-aligned component of the neutral-wind velocity derived from the FPI, $U_{//\mathrm{FPI}}$, depends on the motions of neutrals over the entire emission-height range monitored with the FPI, though the motion of neutrals at altitudes at which the emission rate has its peak will affect $U_{//\mathrm{FPI}}$ more significantly than such motion at other altitudes. We will use two methods, I and II, to interpret $U_{//\mathrm{FPI}}$:

I) $U_{//}^{(I)}$ is the height-integrated velocity over the emission layer ($z_1 \leq z \leq z_2$). The weighting function for the integration is the emission rate normalized to the peak value:

$$U_{//}^{(I)} = \int_{z_1}^{z_2} \sigma(z) U_{//\mathrm{EISCAT}}(z) dz / \int_{z_1}^{z_2} \sigma(z) dz, \tag{3.1}$$

where σ(z) is the emission rate of the auroral red-line as a function of height, z_1 and z_2 stand for the altitudes of 165 and 275 km, respectively, and $U_{//\mathrm{EISCAT}}$ is the field-aligned neutral-wind velocity derived from EISCAT radar data and the MSIS model according to Eq. (1.6).

II) $U_{//}^{(II)}$ corresponds to the neutral-wind velocity solely around an altitude where the emission rate has its peak:

$$U_{//}^{(II)} = U_{//\mathrm{EISCAT}}|_{z=height\ of\ max.\ emission}. \tag{3.2}$$

3.4 Observational results

Figure 3.1 shows temporal variations of the electron densities (a) and the ion temperatures (b) observed with the EISCAT radar at two heights within the *F*-region (231 and 253 km) during the interval of simultaneous observations on February 8. It should be noted that the EISCAT radar data inevitably includes errors. There are some error sources that are not possible to be evaluated quantitatively. Error bars in Fig. 3.1 are estimated from residual between observed and modeled IS spectrum. Between 1900 and 2000 UT and 2330 and 0100 UT, the electron densities at both heights fluctuated with variabilities of greater than 6×10^{10} m^{-3}, presumably due to electron precipitation. The ion temperatures at both heights also fluctuated due to Joule and frictional heating. The graphs show that the strong increases seen in the ion temperatures (at 1912, 1922, 1940, 2349, and 0036 UT) coincided with reductions in the electron density. After these decreases in the electron density, the ion temperature

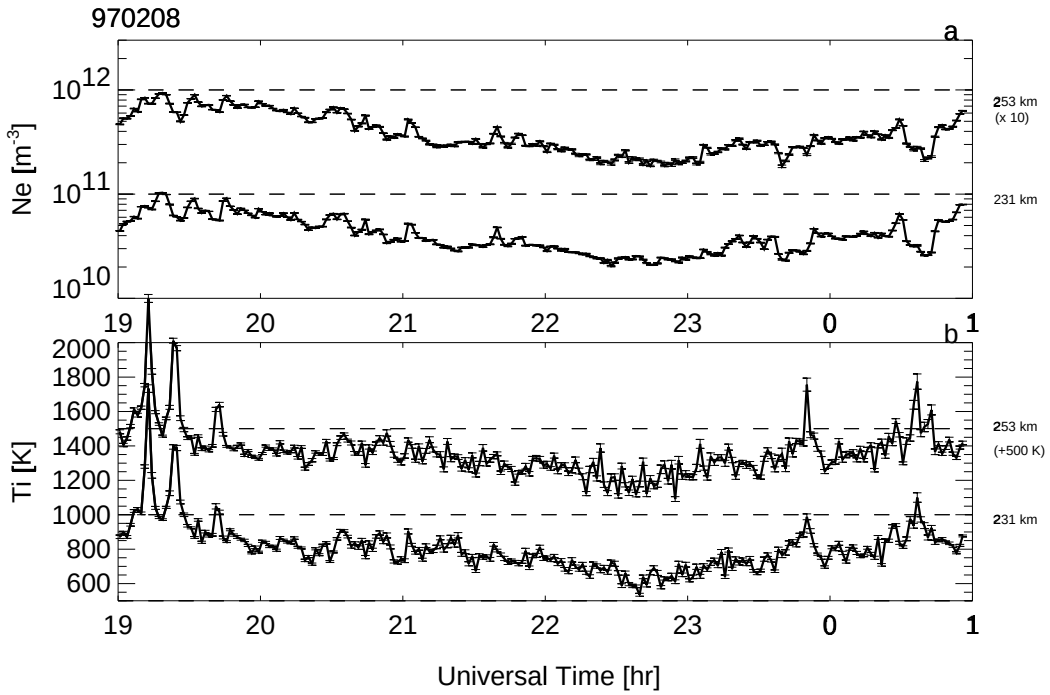

Figure 3.1: *(a) EISCAT electron density and (b) ion temperature as a function of time at altitudes of 231 and 253 km. The electron density at 253 km is multiplied by 10, and the ion temperature at 253 km is shifted by 500 K to avoid overlapping.*

increased immediately. This asymmetry between the ion temperature and the electron density appear to be associated with heating and electron precipitation in the vicinity of an auroral arc [*Opgenoorth et al.*, 1990, and references therein]. It appears that energy is dissipated in the ionosphere due to Joule/frictional heating as well as due to particle heating during geomagnetically active intervals. Because the derivation of the neutral-wind velocity from EISCAT radar data is less accurate during such active intervals, we must be careful when using EISCAT radar data when strong fluctuations in density and temperature are observed. The electron densities and ion temperatures observed from 2000 to 2330 UT showed smaller fluctuations than the densities and temperatures during the disturbed intervals. While there were brief enhancements of the electron densities at around 2030, 2102, and 2138 UT, the relative smallness of these fluctuations suggests that we can more reliably derive neutral-wind velocities during quiet periods.

Figure 3.2a shows $U_{//\mathrm{FPI}}$ including some data gaps. Error bars in Fig. 3.2 are estimated from the residuals between observed and modeled FPI fringe. A running average was taken over sets of five data points after interpolating data in the gaps using a linear function, so that the gaps are not visible on the curve. The intervals in which there were gaps are shaded with the darker gray. The intervals over which the variations in fringe radii, as noted in

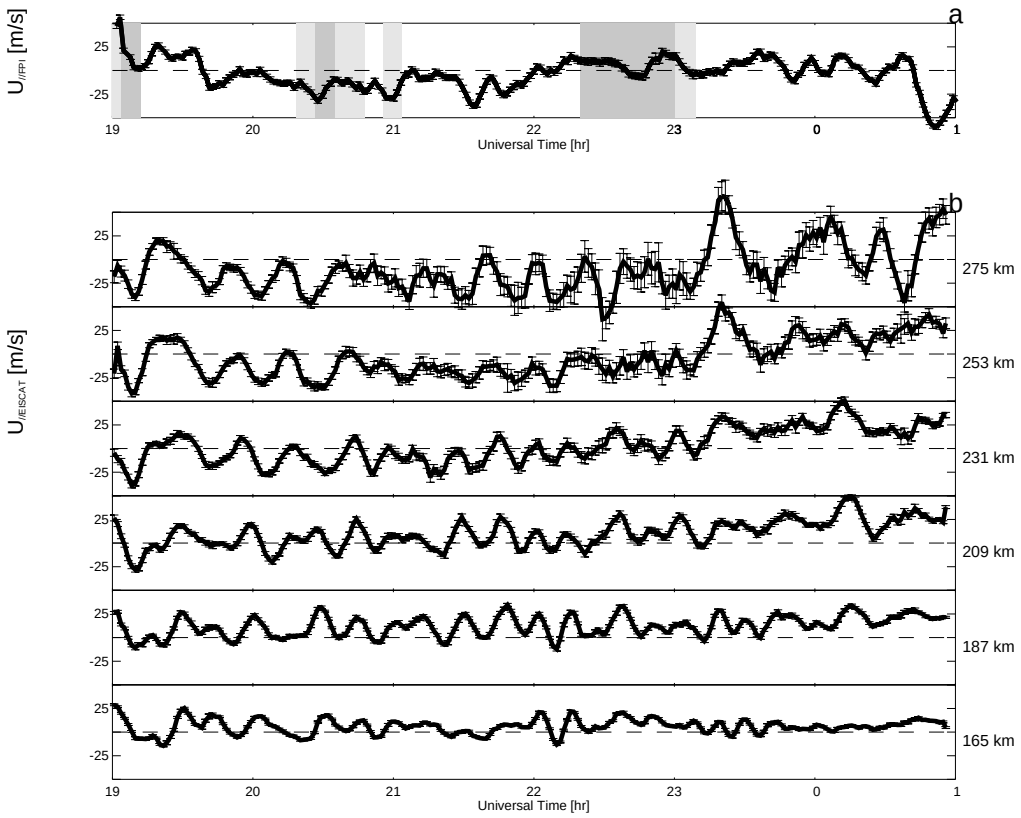

Figure 3.2: *(a) Field-aligned neutral-wind velocity observed with the scanning FPI, and (b) derived from EISCAT UHF radar data with height range from 165 to 275 km. Winds are positive upward along the field line. The shaded parts in the upper panel are explained in the text.*

Chapter 2, were shaded with the lighter gray. We compared the neutral-wind velocity in three intervals in the analysis: (A) 1912-2020 UT, (B) 2106-2218 UT, and (C) 2310-0100 UT. A wind is shown flowing upward along the geomagnetic field line.

Figure 3.2b shows $U_{//\mathrm{EISCAT}}$ at altitudes from 165 to 275 km. There are two major error sources for $U_{//\mathrm{EISCAT}}$ to be considered. First, each ionospheric parameter from the EISCAT radar has an error at the time of measurement and the data processing. Second, neutral atmospheric-parameters from MSIS model have a discrepancy from the actual value. Because it is not possible to evaluate the discrepancy in the neutral atmosphere parameters, we calculate error values of $U_{//\mathrm{EISCAT}}$ using error values of EISCAT radar data. Over the relevant interval there were no gaps in EISCAT radar data from 165 to 275 km, and the errors of fit were small. If the ion composition model used for the IS spectrum analysis has a relatively large ambiguity in geomagnetically disturbed conditions, $U_{//\mathrm{EISCAT}}$ in such disturbed conditions would be expected to have larger errors than during the quiet conditions.

Table 3.1: *Cross-correlation coefficients and time lags between $U_{//EISCAT}$ at an altitude of 275 km and at other heights, for interval A (1912-2020 UT).*

Altitude [km]	165	187	209	231	253
Cross-correlation coefficient	0.56	0.65	0.70	0.85	0.95
Time lag [min]	12.0	10.5	7.5	4.5	1.5

This is because the larger fitting error of EISCAT radar data introduces a greater degree of uncertainty for the diffusion velocities. However, the sizes of the error bars in Fig. 3.2b do not change greatly over the interval of observation. This suggests that uncertainty in the ion composition model did not strongly affect $U_{//\mathrm{EISCAT}}$ in this height range. Using Fourier analysis, the oscillation periods of the neutral-wind velocities at these altitudes were found to range from 14 to 32 min, and were longer than the Brunt-Väisälä period in this height range. Fourier analysis also showed that the mean amplitudes of the oscillations of $U_{//\mathrm{EISCAT}}$ increased with height. Cross-correlation analysis of the values for $U_{//\mathrm{EISCAT}}$ at an altitude of 275 km and at other altitudes showed that the phase was dependent on height (Table 3.1). The decrease in the time lag with height is consistent with the results of simulations obtained by *Kirchengast* [1997]. A downward propagation of phase with time was not seen. The phase propagation will be seen, however, in $U_{//\mathrm{EISCAT}}$ derived for altitudes below 160 km. This is because, in general, it becomes easier to detect the phenomena with decreasing altitude. The wavelike structures observed with the EISCAT radar using Fourier and cross-correlation analysis are probably associated with GWs.

Figure 3.3a shows the height profile of the red-line emission rate calculated using data from the EISCAT radar and the MSIS model. The emission rate was normalized to the maximum value obtained at 1945 UT at an altitude of 231 km. The thick line shows the altitude of the peak emission rate. This altitude was used to derive the neutral-wind velocity for method II. The altitude of the peak emission rate was 231 km before 2100 UT. After 2100 UT, the altitude fluctuates between two gates; however, it is difficult to discuss the height variation of the peak emission rate from this fluctuation. During the observations, it is expected that the altitude would be quite constant, at around 231 km. The thickness of the emission layer was defined as the width over which the emission rate is greater than 1/e of its peak value. Solid circles show the upper and lower boundaries of the emission layer. The boundaries sometimes moved below and/or above the height range, from 165 to 275 km, covered by EISCAT radar data used here. Solid circles outside the height range indicate such cases. When the upper and lower boundaries of the emission layer were within the height range, we were able to use method I to estimate the FPI neutral-wind velocity from EISCAT

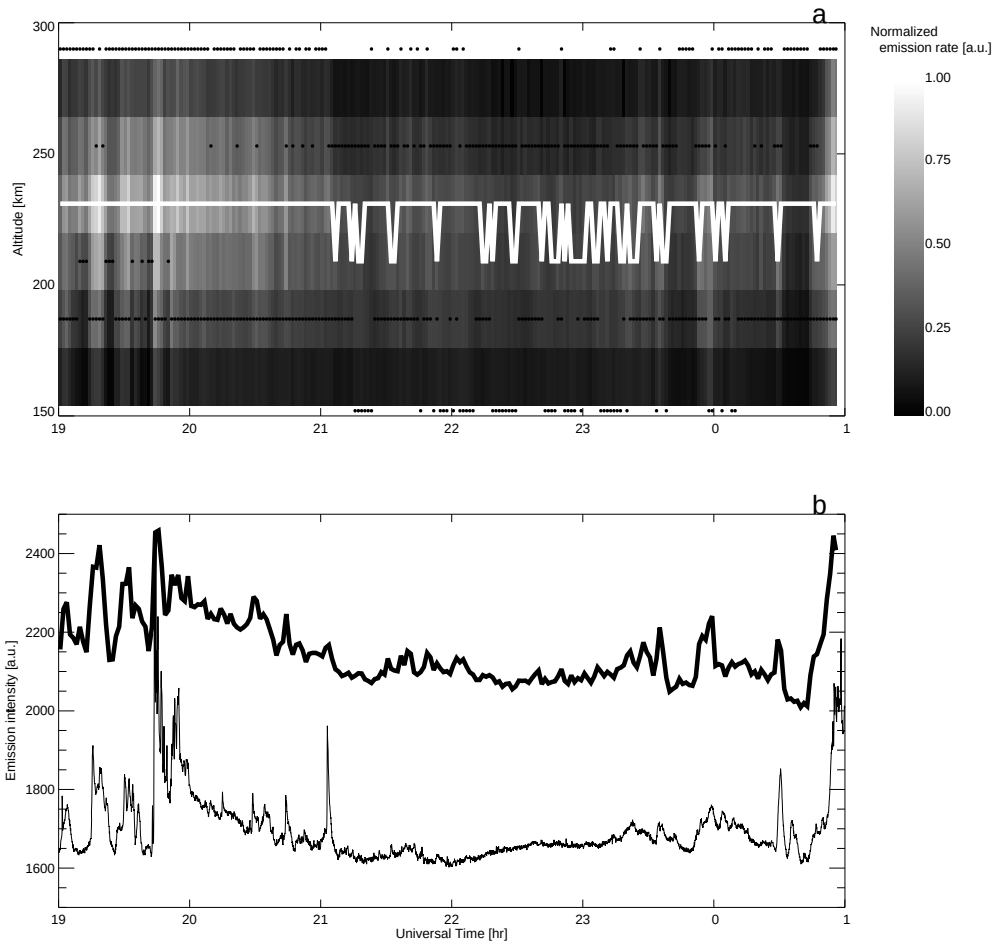

Figure 3.3: *(a) Height profile of red-line emission rate calculated using EISCAT radar data. The thick line shows the altitude where the emission rate has its peak. The solid circles show the upper and lower boundaries of the emission layer, and those beyond the height range (165 to 275 km) indicate upper or lower boundaries that are not within the height range. (b) 630.0 nm count profile observed by the photometer along the field line (thin line), and the integrated emission rate over the height range from 165 to 275 km (thick line).*

radar data. However, when the boundaries were beyond the height range, larger ambiguities may have been present in the amplitude and phase of the neutral-wind velocity estimated from EISCAT radar data. The effects of the thickness of the emission layer on the amplitude and the phase relation will be discussed in Section 3.5.

Figure 3.3b shows the photometer count and the emission rate integrated over the height range from 165 to 275 km on the basis of the normalized rate indicated by Fig. 3.3a. Photometer data are plotted every 5 sec as indicated with the thin line. The integrated emission rate is plotted with the thick line, which has been shifted and multiplied by a factor to avoid overlapping. The cross-correlation coefficient between the photometric measurements and the derived total emission is 0.81, with the maximum at zero time lag. This relatively

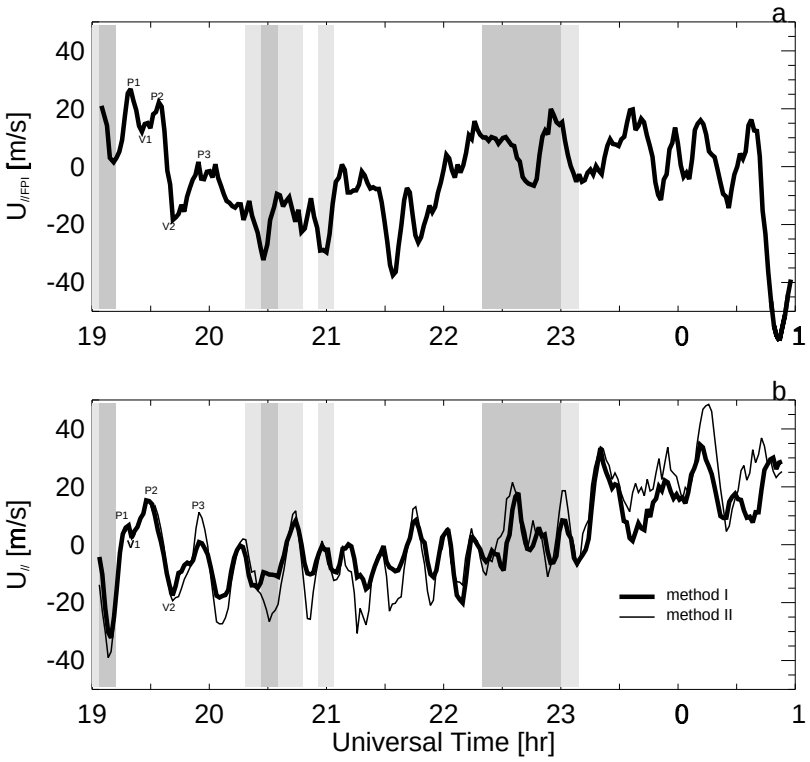

Figure 3.4: *(a) Field-aligned neutral-wind velocity derived from the scanning FPI, and (b) from EISCAT radar data for both methods I and II.*

strong correlation suggests that our emission model, in combination with observed ionospheric data, quite accurately reflects the behavior of the real emissions.

Figure 3.4 shows (a) $U_{//\mathrm{FPI}}$ and (b) $U_{//}^{(I)}$ (thick line) and $U_{//}^{(II)}$ (thin line). The shading is the same as in Fig. 3.2a. There are discrepancies in the amplitudes between $U_{//}^{(I)}$ and $U_{//}^{(II)}$; however, both neutral winds have similar wavelike structures.

We performed a Fourier analysis on $U_{//}^{(I)}$, $U_{//}^{(II)}$, and $U_{//\mathrm{FPI}}$ for intervals A, B, and C, to investigate the amplitude and the phase in more detail. The thick lines with solid circles in Fig. 3.5 are the spectra of $U_{//\mathrm{FPI}}$. The thick lines with open circles are the spectra of $U_{//}^{(I)}$, and the dashed lines with open circles are those of $U_{//}^{(II)}$. The shortest oscillation-period in which we are interested is 14 min because of the data integration over about 7 min, and the longest period corresponds to half the length of the observing intervals: 34 min for interval A, 36 min for interval B, and 55 min for interval C. The shortest and longest periods are marked with the vertical dashed lines. This spectrum analysis, including the phase relation,

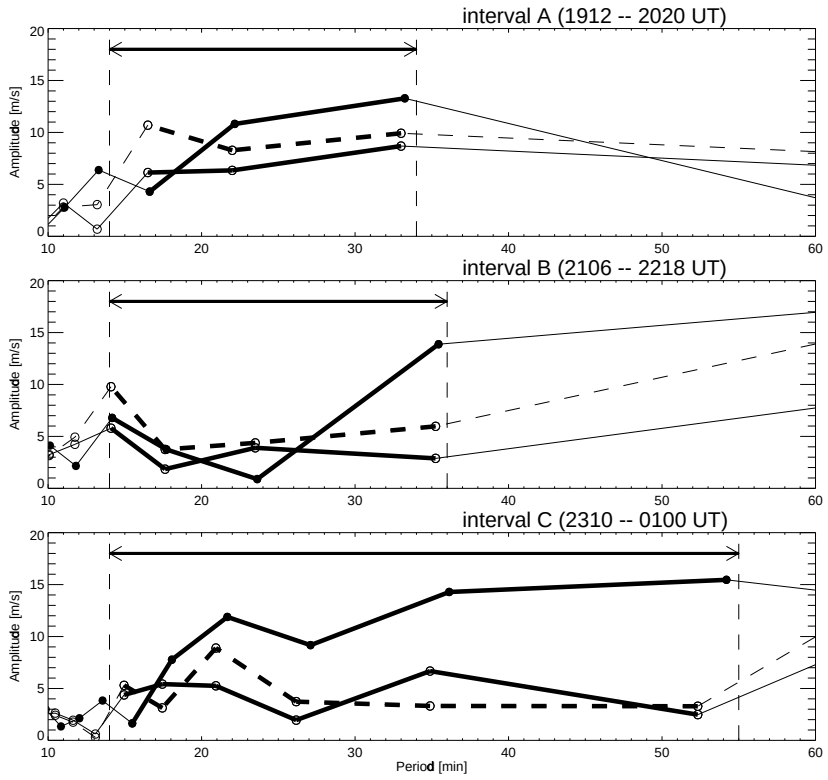

Figure 3.5: *Results of spectrum analysis of the field-aligned neutral-wind velocities shown in Fig. 3.4. Thick lines with solid circles are the spectra of the neutral-wind velocity observed with the FPI. Thick lines with open circles are the spectra of the neutral-wind velocity for method I, and dashed lines with open circles are for method II. The vertical dashed lines show the shorter and longer periods used to compare the spectra: 14 and 34 min for interval A, 14 and 36 min for interval B, and 14 and 55 min for interval C.*

produced the following results.

1. *Period and amplitude of the oscillations*

   Table 3.2 shows the amplitudes integrated over the selected oscillation periods: 14–34 min for interval A, 14–36 min for interval B, and 14–55 min for interval C. For intervals A and B, the amplitudes of $U_{//}^{(II)}$ were closer to those of $U_{//\mathrm{FPI}}$ than those of $U_{//}^{(I)}$. For interval C, the amplitudes of $U_{//}^{(I)}$ and $U_{//}^{(II)}$ were smaller than that of $U_{//\mathrm{FPI}}$.

   Figure 3.5 shows that, for interval A, the spectrum of $U_{//}^{(I)}$ was similar to that of $U_{//}^{(II)}$, though there was a difference in the amplitude at about 17 min. For interval B, while there was also a difference in the amplitude at about 35 min, the spectrum of $U_{//}^{(I)}$ agreed well with that of $U_{//}^{(II)}$. These good agreements suggest that the neutral-wind velocity at around the altitude of the peak emission rate approximately represents the

Table 3.2: *Integrated amplitude of $U_{//FPI}$ and $U_{//}^{(I)}$, and $U_{//}^{(II)}$ over selected oscillation-periods for each interval.*

	A	B	C
$U_{//\mathrm{FPI}}$	28 m/s	25 m/s	60 m/s
$U_{//}^{(I)}$	21 m/s	14 m/s	26 m/s
$U_{//}^{(II)}$	28 m/s	23 m/s	27 m/s

velocity for method I. For interval C, the amplitudes for methods I and II showed relatively large differences at about 21 and 35 min, although the amplitudes at periods of about 15 and 52 min were in good agreement.

For interval A, discrepancies in the amplitude between $U_{//\mathrm{FPI}}$ and $U_{//}^{(I)}$ and between $U_{//\mathrm{FPI}}$ and $U_{//}^{(II)}$ can be seen in the spectra. At about 17 min, the amplitude of $U_{//}^{(II)}$ was greater than that of $U_{//\mathrm{FPI}}$, by a factor of three. At about 22 and 33 min, the amplitudes of $U_{//}^{(I)}$ and $U_{//}^{(II)}$ were both less than that of $U_{//\mathrm{FPI}}$. For interval B, the spectra of $U_{//}^{(I)}$ and $U_{//}^{(II)}$ agreed fairly well with the spectrum of $U_{//\mathrm{FPI}}$, except for the amplitudes at about 23 and 35 min. The three spectra had peak amplitudes at about 14 min. For interval C, the spectra of $U_{//\mathrm{FPI}}$ and $U_{//}^{(I)}$ had similar trends in amplitude from about 21 to about 35 min, though there were large discrepancies in the magnitudes (a factor of about three). The spectra of $U_{//\mathrm{FPI}}$ and $U_{//}^{(II)}$ had peaks at about 21 min. The reasons for the discrepancies in amplitude as well as the phase relation will be discussed in Section 3.5.

Table 3.3: *Cross-correlation coefficients and time lags between $U_{//}^{(I)}$ and $U_{//FPI}$ and between $U_{//}^{(II)}$ and $U_{//FPI}$. The significance of the cross-correlation coefficient is also tabulated.*

	A		B		C	
	I	II	I	II	I	II
Cross-correlation coefficient	0.792	0.718	0.525	0.633	0.150	0.153
Time lag [min]	3.0	1.5	13.5	15.0	15.0	3.0
Significance	> 0.99	> 0.99	> 0.99	> 0.99	> 0.70	> 0.70

2. *Cross-correlation and phase relation*

Table 3.3 shows the cross-correlation coefficients and time lags. For interval A, the cross-correlation coefficients were relatively high, and the time lags were short. The significance was quite high and it thus appears that the oscillations in $U_{//}^{(I)}$ and $U_{//}^{(II)}$ are synchronized with those of $U_{//\mathrm{FPI}}$. For interval B, while the significances remained high, the cross-correlation coefficients and time lags probably do not reflect synchronization of the oscillations in $U_{//}^{(I)}$ and $U_{//\mathrm{FPI}}$ and in oscillations in $U_{//}^{(II)}$ and $U_{//\mathrm{FPI}}$. For interval C, the oscillations in $U_{//}^{(I)}$ and $U_{//}^{(II)}$ are not thought to be correlated with those in $U_{//\mathrm{FPI}}$ because of the low cross-correlation coefficients, long time lags, and low levels of significance.

3.5 Discussion and conclusions

We have compared the field-aligned motions of ions and neutrals obtained from simultaneous EISCAT and FPI observations. The spectra of $U_{//}^{(I)}$, $U_{//}^{(II)}$, and $U_{//\mathrm{FPI}}$ indicated oscillation periods from 14 to 55 min, as shown in Fig. 3.5. One dominant oscillation period is about 14 min, which is close to the Brunt-Väisälä period in the F-region. The observed wavelike structures in other dominant oscillation periods appear to result from gravity waves because the periods are greater than the Brunt-Väisälä period in the F-region.

There are two processes involved in the momentum transfer between ions and neutrals. One is momentum transfer from ions to neutrals, which takes more than one hour in the F-region. The other is momentum transfer from neutrals to ions, which only takes a few seconds in the F-region. The former process makes the neutrals oscillate with the same periods as the ions if the ions are oscillating at periods of more than one hour. $U_{//\mathrm{FPI}}$ from 1900 UT, shown in Fig. 3.4a, gradually shifted from upward to downward along the field line, and its minimum value was -37 m/s at 2134 UT. The amplitude of $U_{//\mathrm{FPI}}$ then decreased until the end of interval B. For interval C, significant long-period oscillations are not seen. While there were discrepancies in the amplitudes, the oscillations in $U_{//}^{(I)}$ and $U_{//}^{(II)}$ were similar to those in $U_{//\mathrm{FPI}}$. This indicates that motions of neutrals at periods of longer than one hour may be estimated using EISCAT radar data. This agreement is consistent with the results of the comparison of meridional wind velocities observed with the EISCAT radar and with the MICADO interferometer [*Thuillier et al.*, 1990]. This similarity, however, does not mean that the momentum transfer process from ions to neutrals is dominant in the motions at periods of longer than one hour because the momentum transfer from neutrals to ions can also make ions oscillate with periods longer than one hour if neutrals oscillate at longer periods.

In the case of the momentum transfer process from neutrals to ions, ions are capable of oscillating at almost the same amplitudes as the neutrals, propagating in phase with the neutrals. Thus, this process should produce a high cross-correlation coefficients with no time lags between $U_{//}^{(I)}$ and $U_{//\mathrm{FPI}}$ and between $U_{//}^{(II)}$ and $U_{//\mathrm{FPI}}$.

For interval A, the upper boundaries of the emission layer were above 275 km height most of the time as shown in Fig. 3.3a. The lack of neutral-wind velocity at altitudes higher than 275 km results in an underestimation of the amplitude of $U_{//}^{(I)}$ because, in general, the neutral-wind amplitude increases with height in the F-region [*Witasse et al.*, 1998]. This is because the integrated amplitudes of $U_{//}^{(I)}$ were smaller than the amplitude of $U_{//\mathrm{FPI}}$, as shown in Table 3.2. The neutral-wind velocity at lower altitude tended to contribute to the phase of $U_{//\mathrm{FPI}}$ more significantly than those at higher altitude because of a downward phase propagation with time. For interval A, $U_{//}^{(I)}$ was thought to reflect all the neutral-wind motions that affected the phase relation of $U_{//\mathrm{FPI}}$, because the lower boundaries of the emission layer were always higher than the bottom of the height range covered by EISCAT radar data. This is because, for interval A, the cross-correlation coefficient was relatively high, and the time lag was relatively small, as shown in Table 3.3.

For intervals B and C, the emission layers seem to have been thinner than those for interval A, as shown in Fig. 3.3a. The thinness of the layer may have led us to expect that the amplitude and the phase of $U_{//}^{(I)}$ would be close to those of $U_{//\mathrm{FPI}}$ because the degree of height ambiguity in the FPI data would be small. The frequent expansion and downward/upward shifting of the emission layer, however, seem to have affected the amplitude and phase more seriously. The upper boundaries of the emission layer were sometimes at altitudes above 275 km, resulting in an underestimation of the amplitude of $U_{//}^{(I)}$. This is consistent with the discrepancies in the integrated amplitude in Table 3.2. The lower boundaries of the emission layer frequently shifted to altitudes below 165 km, and this results in an incorrect phase relation of $U_{//}^{(I)}$. This is because the phase relations for intervals B and C had relatively low cross-correlation coefficients and large time lags as shown in Table 3.3.

The peak-to-peak correspondences between $U_{//}^{(I)}$ and $U_{//\mathrm{FPI}}$ and between $U_{//}^{(II)}$ and $U_{//\mathrm{FPI}}$ can be seen in Fig. 3.4 for intervals A, B, and C. For instance, for interval A, the oscillations in $U_{//\mathrm{FPI}}$ had three maxima (P1, P2, and P3) and two minima (V1 and V2). These oscillations are thought to consist of two wave structures, one with a period of about 33 min, and the other with a period of about 22 min (see the top panel of Fig. 3.5). Similar wave structures were also visible in $U_{//}^{(I)}$ and $U_{//}^{(II)}$ for period A. These oscillation periods are shorter than the period of the momentum transfer from ions to neutrals. The momentum transfer from neutrals to ions is thus dominant in the observed field-aligned oscillations, rather than the momentum transfer from ions to neutrals.

3.6 Summary

Dynamical coupling between ions and neutrals in the auroral F-region has been presented using data obtained simultaneously with the EISCAT radar and the scanning FPI during the night of 8 February 1997, at Tromsø, Norway. The results obtained are summarized as

follows.

1. Our observation is the first experiment simultaneously using optical and radio techniques for targeting short time-scale oscillations of ions and neutrals in the auroral *F*-region. Field-aligned velocities of ions and neutrals obtained have sufficient quality with a time-resolution of about 1.5 min and can be used to investigate dynamical coupling between oscillations of ions and neutrals in the short time-scale.

2. The amplitude and the phase of $U_{//\mathrm{FPI}}$ have been correctly estimated using EISCAT radar data as long as the height range covered by EISCAT radar data in use overlapped the emission layer. It is concluded that the plasma oscillations observed with the EISCAT radar at different altitudes in the *F*-region are thought to be due to the motion of neutrals.

3. Because the field-aligned component of neutral-wind velocity is convoluted by the vertical and horizontal components, we cannot specify the relative importance between the vertical and the horizontal velocities for field-aligned oscillations in neutrals. *Johnson et al.* [1995] suggested that perturbations of neutrals propagated in the polar *F*-region along trajectories of the DE2 satellite with relatively large vertical amplitude ($\sim$ 100 m/s). This result may suggest that the field-aligned oscillations obtained during the simultaneous observations with the EISCAT radar and the scanning FPI were generated by vertical oscillations alone. This suggestion is, however, inconsistent with the predicted amplitude of the vertical wind with theoretical calculations of *Sun et al.* [1995] who predicted the amplitudes induced by thermal expansions are smaller than 10 m/s. To understand the reason for the discrepancies between observed and predicted results, it is necessary to observe the vertical and horizontal components of the neutral-wind velocity simultaneously. We will suggest some candidate experiments in Section 6.

Chapter 4

Field-aligned ion motions in the E- and F-region

4.1 Introduction

The aim of this chapter is to investigate the characteristics of field-aligned (FA) ion motions in the *E*- and *F*-regions and the driving mechanisms of these FA ion motions, with considering electromagnetic and particle energy inputs from the magnetosphere as well as the interaction with vertical and horizontal neutral winds. Section 4.2 describes the data set. We will show results from the statistical analysis based on two data sets. One is obtained on 20-21 April 1993 with KST (Kiruna-Sodankylä-Tromsø) UHF radar, and other is obtained on 9-12 February 1999 with ESR (EISCAT Svalbard Radar); these are described in Section 4.3. The time-dependence of the FA motion of ions and the effects of the electric-field enhancement on the FA motion are discussed in Section 4.4.

4.2 Observations

We will use two data sets in this study. The first one was obtained with the tristatic KST EISCAT radar on 20-21 April 1993. The other one was obtained with the KST radar and the ESR on 9-12 February 1999. The reasons for using these two data sets are as follows. The first data set is obtained from only one radar and therefore represents one-point observations; however, during the observation interval strong enhancements in both northward and southward electric fields are seen and the quality of the data is relatively good. On the other hand, during the acquisition of the second data set, relatively weak enhancements are seen only in the southward electric field and the quality of the data, particularly from the ESR, is poorer; however, the advantage of this data set is that it enables us to compare ion motions at different locations and to distinguish ion motions caused by a local generator from those

caused by a more global one. The KST radar and ESR are located about 1000 km apart and are aligned nearly in a geographic meridional plane as shown in Fig. 4.1.

The modes of the experiments of the two radars were the Common Program One (CP-1) mode for the KST radar and the CP-1L mode for the ESR.

Figure 4.1: *ESR and KST locations in the geographical and geomagnetic coordinates.*

4.3 Data analysis

4.3.1 April 20-21, 1993 case (KST UHF radar data only)

Figure 4.2 shows, from top to bottom, the electric field, the electron densities measured at altitudes of 120 km and 138 km, and the FA ion velocities at 234 km and 212 km, at 190 km and 168 km, and at 138 km and 120 km, respectively. The northward component of the electric field (in red) shows northward enhancements (equivalently eastward Hall current enhancements) at 12–18 UT of April 20 and at 14–18 UT of April 21 and southward enhancements (equivalently westward Hall current enhancements) from 19 UT of April 20 to 04 UT of April 21. The magnetic local time (MLT) at Tromsø is UT plus about 3 hours. The eastward component of the electric field (in blue) is much smaller in amplitude than the northward component. Note that heights where incident electrons produce the maximum ionization are 150 km, 130 km, 115 km, and 110 km for energies of 1 keV, 2 keV, 5 keV, and 10 keV, respectively [*Rees*, 1963]. Electron precipitation with energy of a few keV is stronger in the southward electric field region than in the other regions. The most intense electron precipitation is seen around 18-21 UT (21-24 MLT) of April 20 and around 18-20 UT (21-23

MLT) of April 21 where the electric field changes its direction from northward to southward (correspondingly the Hall current changes its direction from eastward to westward).

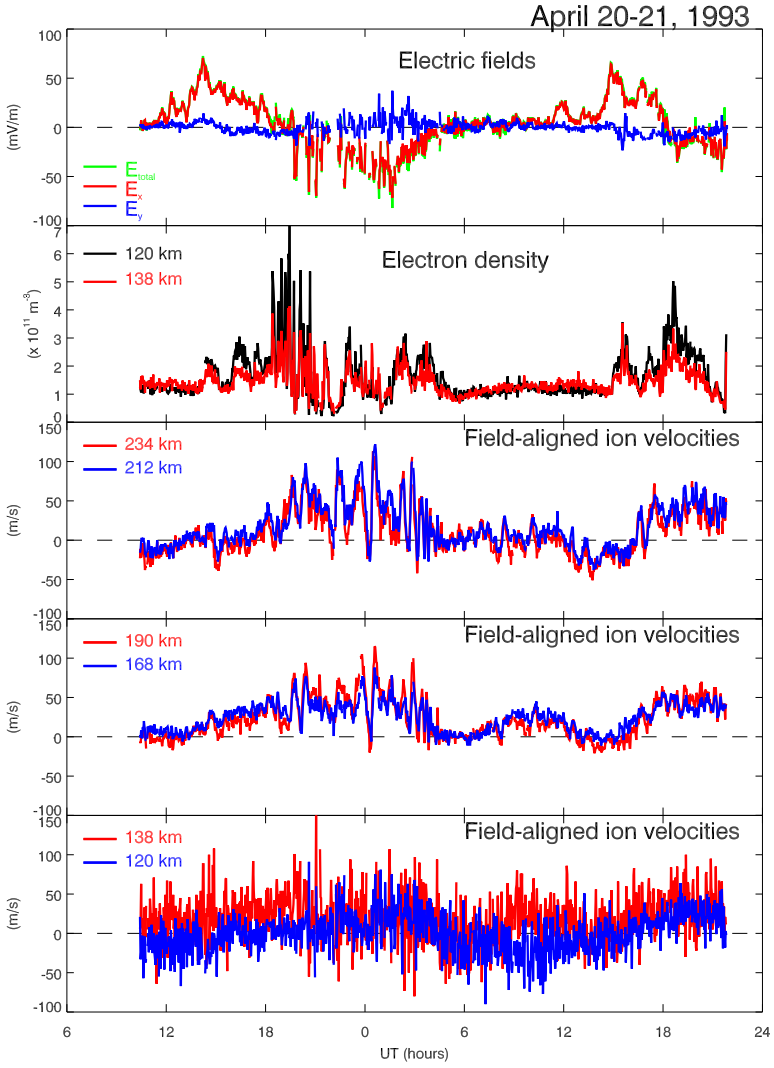

Figure 4.2: *Data obtained from EISCAT KST UHF radar on April 20-21, 1993. From top to bottom, the electric field, the electron densities at altitudes of 120 km and 138 km, and FA ion velocities at 234 km and 212 km, those at 190 km and 168 km, and those at 138 km and 120 km, respectively.*

The panels from the third to bottom of Fig. 4.2 show the FA ion velocities at several heights in the *F*- and *E*-regions. The time variations of the FA velocities at the different heights from 234 km to 168 km are well synchronized with each other even for short time variations of less than 1 hour. During the time intervals of southward electric field enhancements, fast and fluctuating upward FA flows with velocities of more than 100 m/s are frequently seen. This upward FA ion motion associated with a westward electrojet (southward electric field

enhancements) is a common characteristic seen in most of other available data sets (not shown here). On the other hand, weaker FA flows are seen during the time intervals of northward electric field enhancements; for the present data, weak downward flows (weak upward flows) at higher (lower) altitudes of 234 km and 212 km (190 km and 168 km). While FA velocities at lower altitudes, 138 km and 120 km, fluctuated much more than those at higher heights, the long-term trends appear to be still synchronized with those at higher altitudes. That is, upward velocity enhancements for the southward electric fields and relatively small FA velocities for the northward electric field are seen, although the FA velocity at the altitude of 120 km appears to be biased a little bit towards a negative values.

Figure 4.3 shows the AE index and the Tromsø magnetogram during the time period. The AE index indicates that the two days were very disturbed with magnitudes reaching or exceeding 1000 nT occurring repeatedly; in particular, the disturbance around 1800 UT reached more than 2000 nT. The H-component of the Tromsø magnetogram shows very intense positive enhancements (eastward electrojet) with maxima of more than 400 nT in the afternoon and evening and negative enhancements with minima of less than -400 nT around the midnight region.

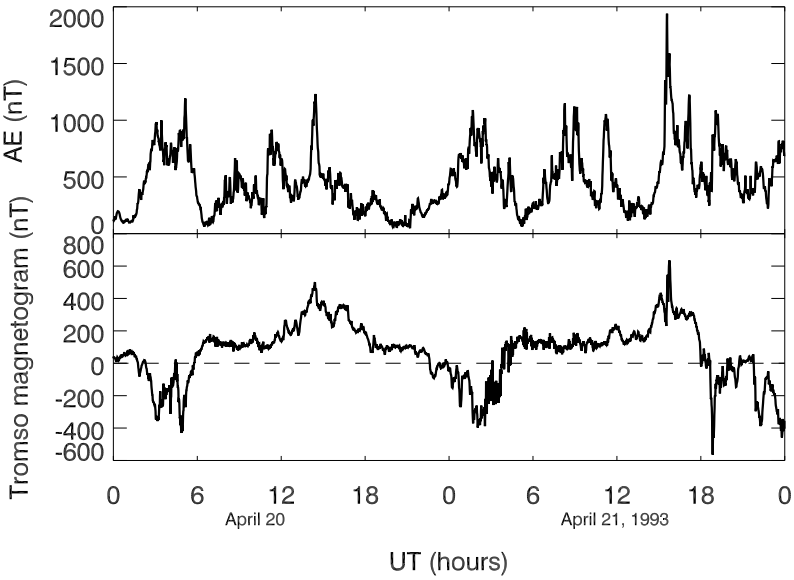

Figure 4.3: *AE index and the Tromso magnetogram on April 20-21, 1993.*

Figure 4.4 shows histograms of the FA ion velocities at several altitudes during the interval when data were acquired. The number in the parenthesis at the right top corner of each panel shows the vertical scale of the sampled number. At the lowest altitude, 108 km, the FA ion velocity is less mainly between -30 m/s and +30 m/s and the distribution is symmetrical around zero velocity. A plausible interpretation for the symmetry is that

the ions are driven predominantly by horizontal neutral winds with velocities of less than 150 m/s ($\simeq$ 30 (m/s)/cos(90°-12°)) that flow randomly both northward and southward with a statistically equal occurrence rate. At an altitude of 123 km, in the vicinity of which the Pedersen conductivity is often maximized, the velocity distribution is also symmetrical around zero velocity but the velocity range is broader (equivalently an increase of the half width of the half maximum of the distribution) than at 108 km.

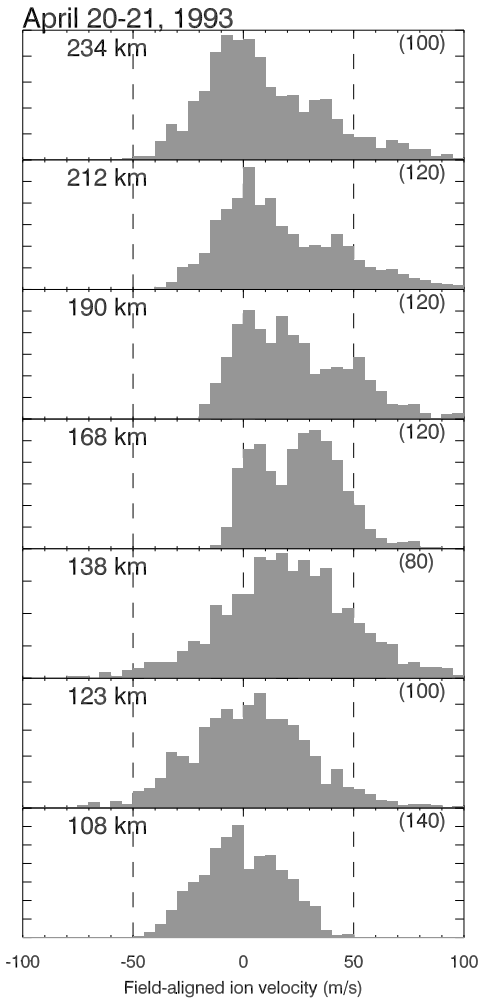

Figure 4.4: *Histograms of the FA ion velocities at 108 km, 123 km, 138 km, 168 km, 190 km, 212 km, and 234 km heights on April 20-21, 1993. The number in the parenthesis at the right upper corner of each panel shows the vertical scale of the sampled number.*

At an altitude of 138 km, the velocity distribution is broader and shifted to positive values but appears to be still symmetrical around some positive value, say 20 m/s. At an altitude of 168 km, the FA velocity is mostly positive with the velocity between 0 m/s and 50 m/s and again appears to be symmetrical around some non-zero shifted value centered

around 30 m/s in this case. This shifted center velocity at 168 km can change from one data set to another. It should be noted that the data set used here is taken at all MLTs, including around midday (midnight) region where the prevailing neutral wind is directed poleward (equatorward), tending to drag ions FA downward (upward).

At altitudes of 190 km through 234 km, the FA velocity distribution becomes asymmetrical. The velocity distribution is broader in the positive velocity range than in the negative velocity range.

Considering the observational fact that the FA ion motion depends greatly on the direction of the electric field, as shown in Fig. 4.2, we will try to determine the relationships between the FA velocity and other parameters such as ion and electron pressures and temperatures for southward electric fields and northward electric fields separately.

Figure 4.5 shows the temporal variations of the FA ion velocity and other parameters between 12 UT of April 20 and 06 UT of April 21, which covers the earlier southward electric field interval 19-04 UT. The electric field (the second panel) fluctuates greatly during the southward electric field interval 19-04 UT and shows an anti-correlation with the enhancements of the electron density (the top panel) at 138 km (that are presumably produced by 1-2 keV incident electrons). That is, the electric field strength becomes smaller with increasing electron density. The electron density is depleted and becomes even lower than the background level when a strong electric field is applied, *e.g.*, between 2010 UT and 2200 UT.

The FA ion velocity (the third panel) is upward and fluctuated very much during the southward electric field interval 19-04 UT. The velocity varies between 0 m/s and more than 100 m/s. These fluctuations are not regularly periodic but appear to have a dominant timescale of 1-2 hours. All of these three parameters, the FA ion velocity, the electric field, and electron precipitation show great enhancements with intense fluctuations during this time interval, but the time variations of the fluctuations are not synchronized in time.

The fourth panel of Fig. 4.5 shows the electron densities at four heights, 168 km, 190 km, 212 km, and 234 km. We notice that each long-term trend shows a diurnal variation. The electron density becomes larger in the daytime and smaller in the nighttime due to the change of the solar irradiation with local time.

In the region where the northward electric field is dominant, the electron density becomes monotonically larger with increasing height under the F-region electron density peak. On the contrary, during the nighttime which features mostly southward electric fields, the electron density shows large, short-duration enhancements that are well synchronized with the electron precipitation monitored at 138 km. In the region dominated by southward electric field, the electron density is temporarily more enhanced with going downward due to the ionization produced by relatively high energy precipitation. Most of the other data sets show more or less the same characteristic mentioned here.

The ion temperatures at the four altitudes (the fifth panel) have strong positive correla-

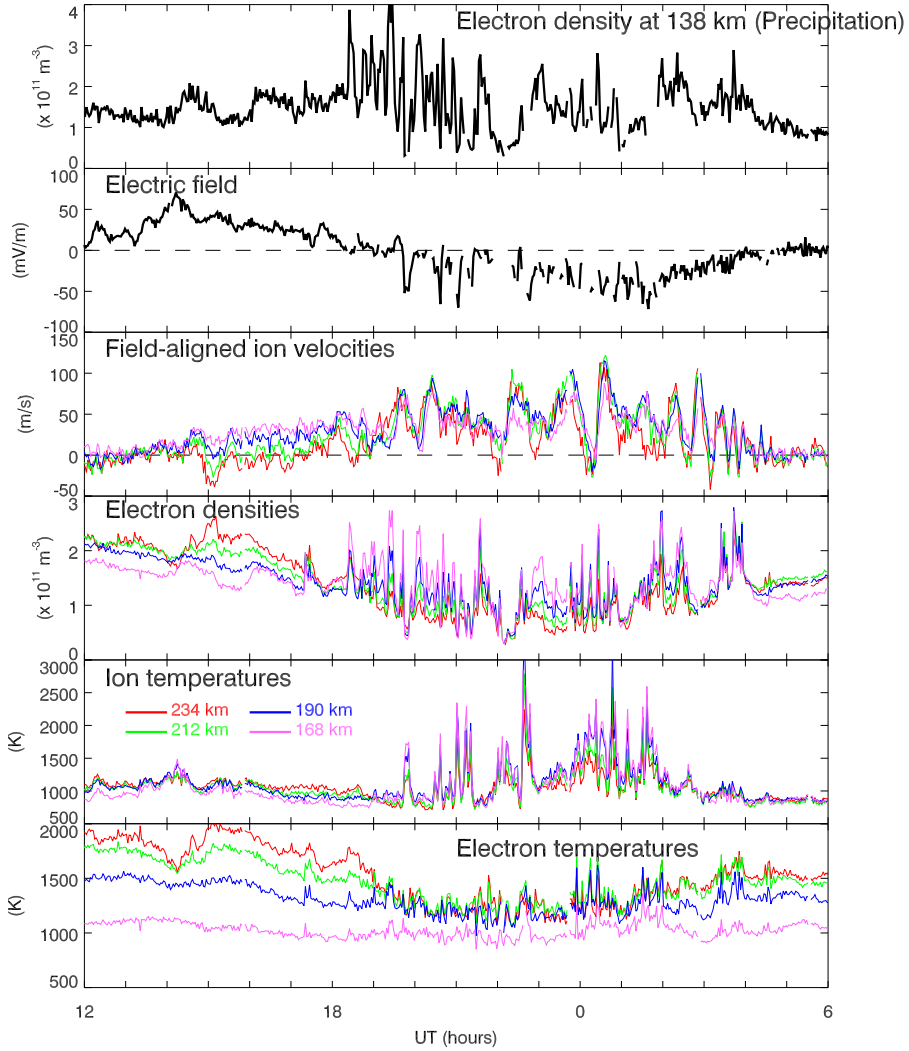

Figure 4.5: *Temporal variations of the FA ion velocity and other parameters between 12 UT of April 20 and 06 UT of April 21, which covers the earlier southward electric field interval 19-04 UT.*

tion and one-to-one correspondence to the electric field amplitude. This temperature increase is caused by frictional heating that occurs instantly (within the data time resolution, 2-min in the present analysis, see also Fig. 4.12 in Section 4.4) [*e.g.*, *Lathuillere et al.*, 1986]. The ion temperatures do not show large differences between the four altitudes, in strong contrast to the electron temperatures mentioned below. It should be noted that the increase of the ion temperature (equivalently the increase of frictional heating) is not necessarily accompanied by an enhancement of the upward FA ion motion.

Outside the region dominated by southward electric field, the electron temperatures at the four altitudes (the bottom panel) have distinct height dependent distributions. The higher the altitude, the higher the electron temperature, with a few hundred Kelvin differences

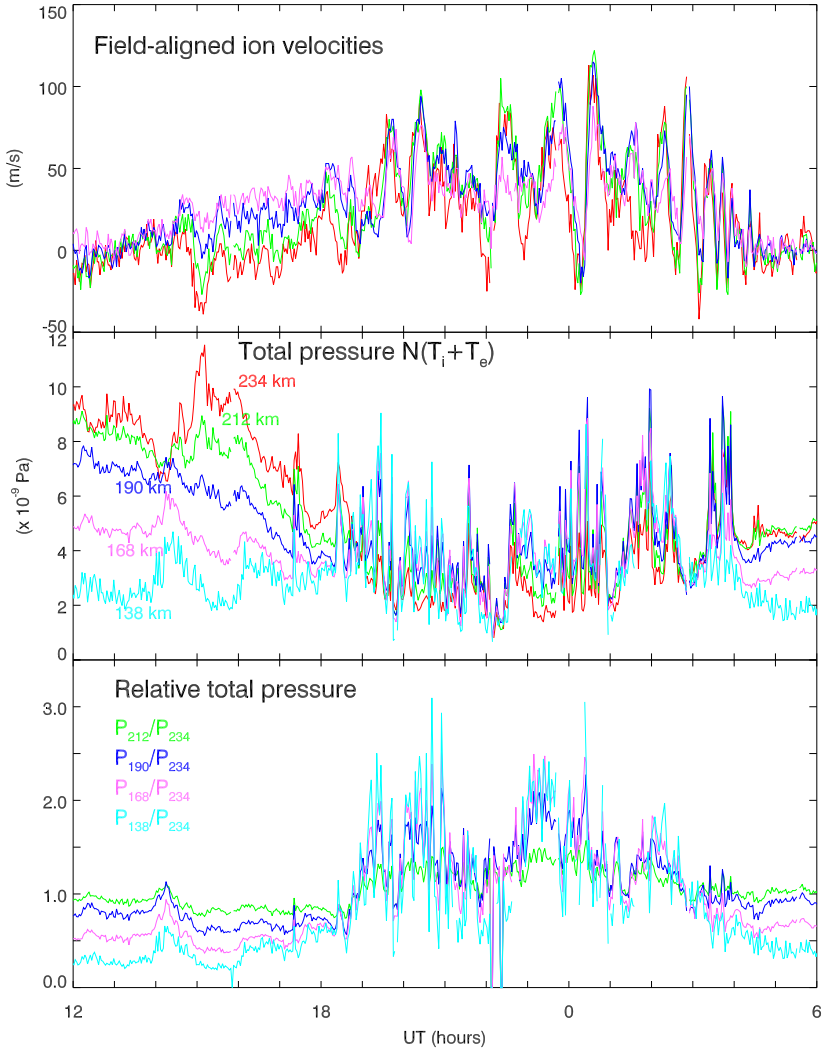

Figure 4.6: *From top to bottom, the FA ion velocities, the total pressure, and the ratios of the total pressure at 234 km to that at the other altitudes. See text for detailed description.*

between adjacent altitude ranges (22 km apart). Within the time interval of the southward electric field enhancements, however, the difference of the temperatures between the altitudes becomes much smaller. This is because the electron temperature at the altitude of 168 km does not change so much, but the electron temperatures at higher altitudes become lower with a larger decrease at a higher altitude. It is also clear from the figure that the time variations of the electron temperatures are not synchronized with those of the ion temperatures.

Figure 4.6 shows, from top to bottom, the FA ion velocities, the total pressure (the second panel) calculated from $N_e\kappa(T_e + T_i)$, and the ratios of the total pressure at 234 km to that at the other altitudes; P_{138km}/P_{234km}, P_{168km}/P_{234km}, P_{190km}/P_{234km}, and P_{212km}/P_{234km}. The Earth's gravity g plus the height gradient of the ion pressure $N_e\kappa T_i$ causes ion diffusion, while that of the electron pressure $N_e\kappa T_e$ causes ambipolar diffusion. The total diffusion

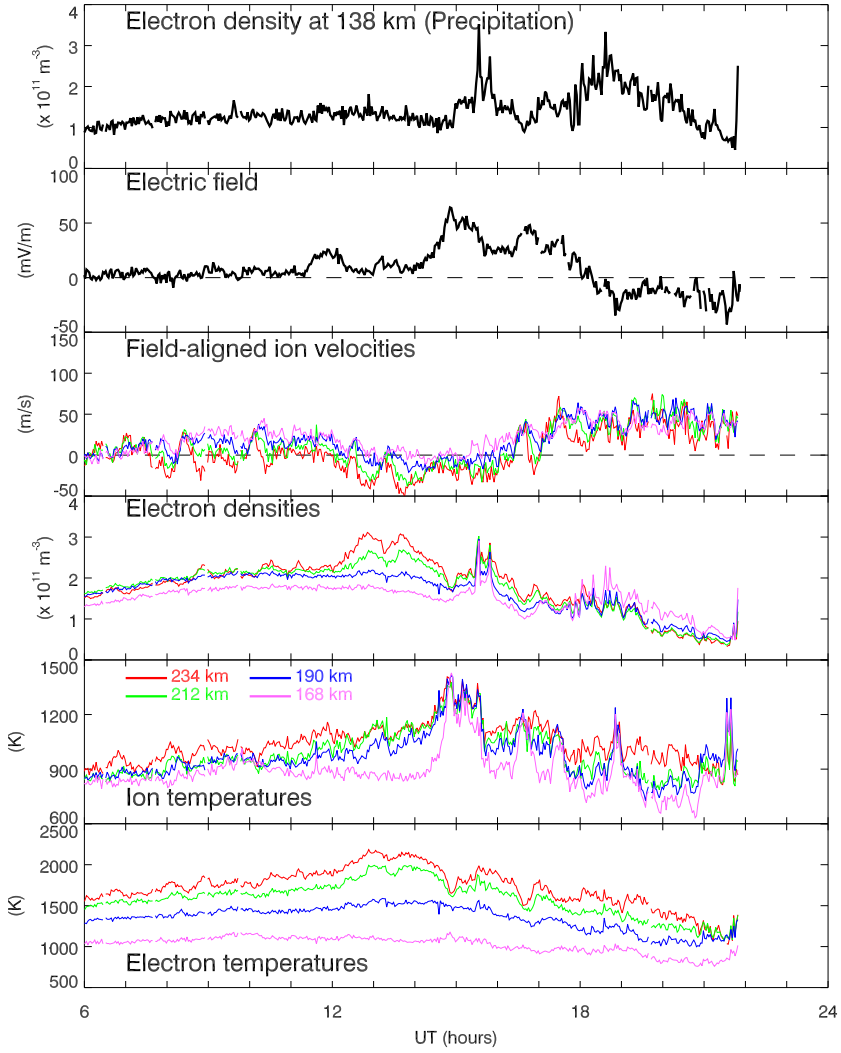

Figure 4.7: *Same as Fig. 4.5, but during the interval of the northward electric field enhancements.*

velocity along the field line is expressed by $V_{d//} = (-\frac{d(N_e\kappa(T_i+T_e))}{ds} - m_i N_e\ g_{//})/(m_i N_e \nu_{in})$. As is expected from the height profiles of the electron density and temperature in Fig. 4.5, the total pressure shows a striking difference between the northward and southward electric field enhancements. In the regions dominated by northward electric field before 1810 UT and after 0400UT, the total pressure becomes larger monotonically with increasing altitude, which makes the ions diffuse downward. This is more clearly seen in the ratios of the total pressure (defined above) in the bottom panel; that is, all ratios are less than 1 and the ratio at a higher altitude is larger than that at lower altitude. On the other hand, in the region dominated by southward electric field, the total pressure becomes smaller than that in the northward electric field dominant region and exhibits irregular increases. For these irregular increases, the total pressure becomes higher with decreasing altitude. These increases of the

total pressure are, as expected from Fig. 4.5, mainly due to the increases of the electron densities and the electron temperatures. The relative pressures in the bottom panel more clearly show this tendency, namely larger pressures at lower altitudes and a ratio that can be as large as 3. The gradient in height of the total pressure for the irregular increases makes the ions diffuse upward. Although the directions of the diffusion appear to favor the directions of the FA ion motion for both northward and southward electric field enhancements, the diffusion velocity is too small (by 1 or 2 orders of magnitude) to explain the observed FA ion velocity as will be described in Section 4.4.

Figure 4.7 shows the same parameters as in Fig. 4.5, but during the interval of the northward electric field enhancements. The FA ion velocity is mostly less than 50 m/s. Downward FA motions are occasionally seen, *e.g.*, at the altitudes of 212 and 234 km during 12 UT and 14 UT. The electron density and the electron temperature respectively show a monotonic increase with an increase of the altitude, this tendency being different from that during the southward electric field interval. The increase of the downward (negative) FA ion velocity at a certain altitude is well correlated to the enhancements of the electron density as well as the electron temperature at the same altitude. The total pressure shown in Fig. 4.8 also depicts this relation more clearly. The total pressure becomes larger with altitude when a downward FA ion motion occurs. Consequently the relative magnitude of the total pressure (bottom panel) does not change much. It should be noted that these height distributions of the electron density and ion and electron temperatures are common characteristics of the dayside ionosphere below the *F*-region density peak.

4.3.2 February 9-12, 1999 case (Simultaneous ESR and KST radar data)

The data were obtained from both KST radar and ESR for more than three consecutive days on February 9-12, 1999, when the solar zenith angle was more than 90° (*i.e.*, the ionosphere was not illuminated by sunlight) during most of the observation periods. Figure 4.8 shows several parameters obtained from the KST radar. The top panel depicts the northward component of the electric field E_N in red, the eastward component E_E in blue and the total electric field E_T ($= \mathrm{sign}(E_N)\cdot(E_N^2 + E_E^2))^{1/2}$ in green. Since the northward component E_N is at most times much larger than the eastward component E_E, the value of the total electric field E_T is almost the same as that of E_N. There are northward electric field enhancements during each afternoon, reaching more than 50 mV/m. On the other hand, there are no strong southward electric field enhancements except early in the morning of February 12.

The second panel presents the electron density at 123 km showing ionization produced mainly by incident electron precipitation during the nighttime and by the solar irradiation during the daytime. The electron density at 123 km hence shows a diurnal variation in the daytime. In the nightside region, enhancements of electron density are seen mostly associated with northward electric field enhancements in this case. The level of these electron

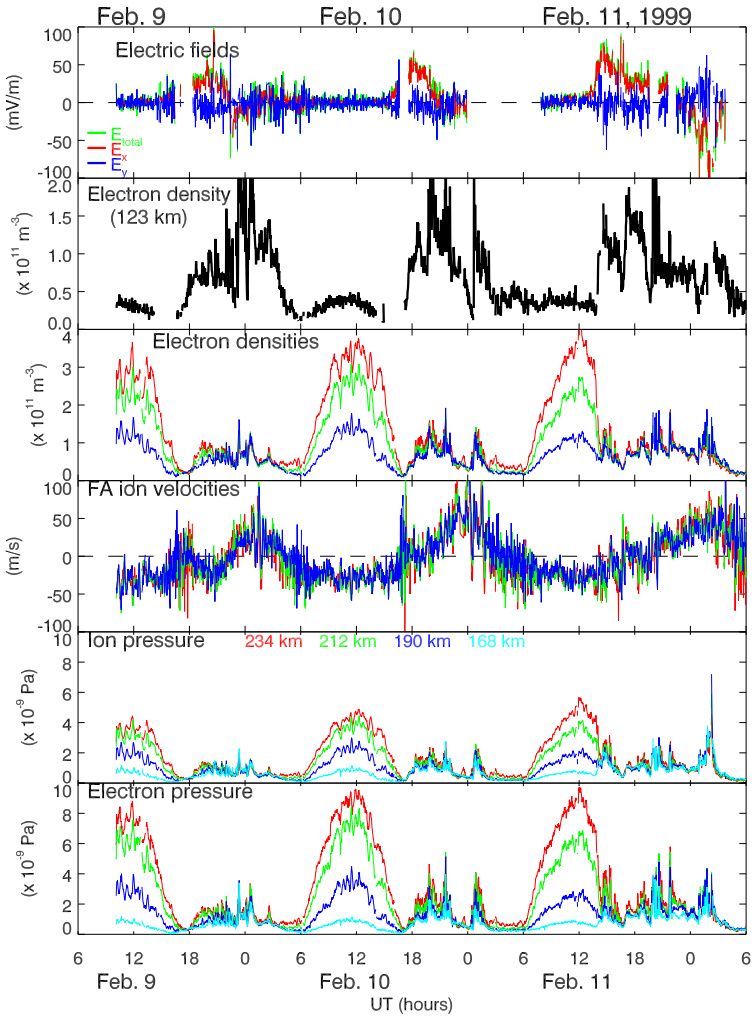

Figure 4.8: *Data obtained from EISCAT KST UHF radar on February 9-12, 1999, during which time period both the KST and ESR radars ran simultaneously. From top to bottom, the electric field, the electron density at 123 km, the electron densities at four altitudes; 168 km, 190 km, 212 km and 234 km heights, the FA ion velocities, ion pressures and electron pressures at these four altitudes.*

density enhancements is nearly the same as that associated with the northward electric field enhancements in the previous case.

The third panel shows the electron densities at 234 km (green), 212 km (blue), 190 km (red), and 168 km (light blue) in the *F*-region, respectively. The electron density at each altitude shows a clear diurnal variation in the dayside region from ∼06 to ∼18 UT with the peak around the midday local time (∼12 UT). The electron density in the dayside region also shows clear altitude dependence where the electron density becomes larger monotonically with an increase of the altitude. It is noted that the ionization level is somewhat higher than that in the previous case regardless of the higher solar zenith angle. On the other hand, in the nightside region the electron density is much lower than that in the dayside region and it

shows more irregular variations associated with the northward electric field enhancements.

The fourth panel shows the FA ion velocities at 234 km (green), 212 km (blue), 190 km (red), and 168 km (light blue), respectively. First, we notice that the FA ion velocity has a clear diurnal variation at all of these heights, that is, FA downward ion motions in the dayside region and upward ion motions in the nightside region. The time variations at these altitudes are well synchronized in phase, which is also seen in the previous case. The upward FA ion motions are seen in the region just after the time of the northward electric field enhancements (eastward Hall current enhancements) in late evening. Although the southward electric field was rather weak, the large-scale upward FA ion motions are confined in this southward electric field region, i.e., in the midnight and post-midnight regions just eastward of the northward electric field region. This characteristic was also seen in the previous case and other cases when data were available. The upward FA ion velocity shows short-term variations, which have larger fluctuations (sometimes exceeding 100 m/s peak-to-peak) than those of the downward FA ion velocity. This characteristic was also seen in the previous case and other cases (not shown here).

The fifth and sixth panels show the ion pressures ($N_e \kappa T_i$) and electron pressures ($N_e \kappa T_e$) at 234 km (green), 212 km (blue), 190 km (red), and 168 km (light blue), respectively. As is inferred from the electron density and ion and electron temperature data, the ion and electron pressures show clear diurnal variations in the downward FA ion region and they become higher with increasing altitude. It is noted that the electron pressure at each altitude is about two times larger than the ion pressure at the same altitude in the downward FA ion region. In the upward FA ion region both ion and electron pressures are smaller than those in the downward FA ion region especially at higher altitudes and hence the difference between the ion and electron pressures at two altitudes also becomes smaller than that in the downward FA ion region. The diffusion velocity due to these ion and electron pressures is directed downward in the downward FA ion motion region, while in the upward FA ion motion region it is mostly directed downward but it becomes much smaller than that in the downward FA ion region.

Figure 4.9 shows a comparison of the FA ion velocity at 212 km high obtained from the KST radar (red) to that from the ESR (blue). Since the ESR data quality is relatively poor, both KST and ESR data are 20-min running averaged data. The long-term trends of both datasets clearly show diurnal variations that are very similar to each other in phase and amplitude. Downward FA ion motions are seen in the daytime when the electron density is greatly enhanced and the ion and electron pressures are also enhanced, while upward FA ion motions are seen during the nighttime when the electron density and ion and electron pressures are depleted so that the pressure gradient of the ion and electron pressures becomes smaller. Histograms of the FA ion velocities at several altitudes in Fig. 4.10 again disclose very synchronized ion FA motions at the two locations. These well-synchronized time variations

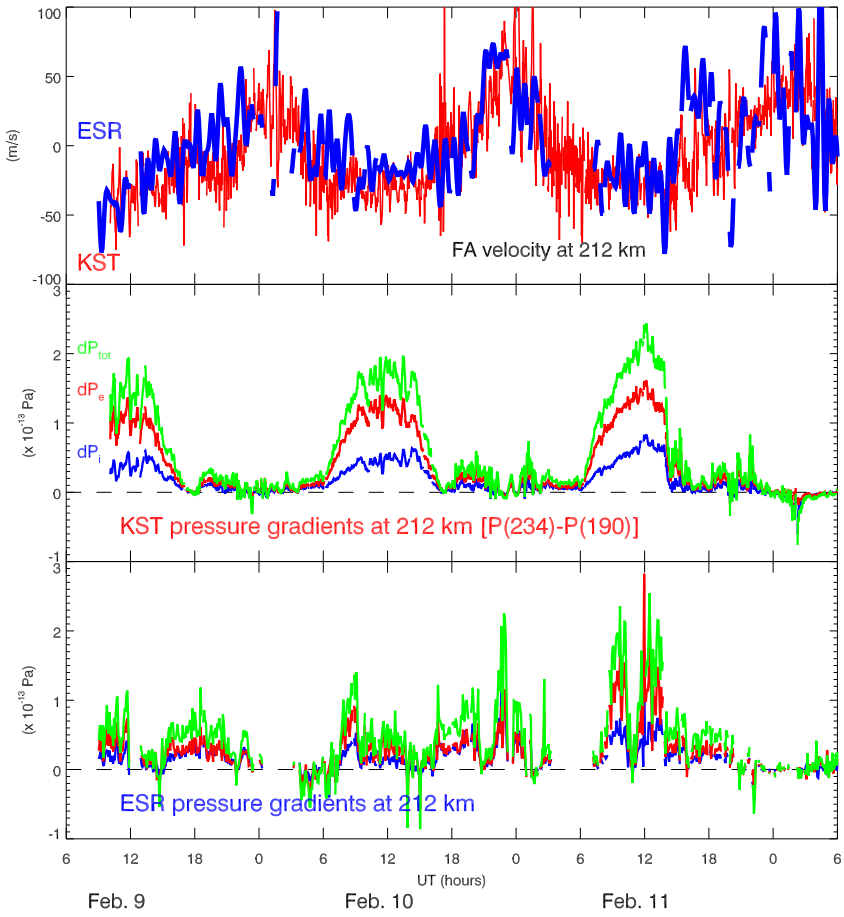

Figure 4.9: *Comparison of the FA ion velocity at 212 km high obtained from the KST radar (red) to that from the ESR radar (blue). Since the ESR data quality is relatively poor, both KST and ESR data are 20-min running averaged data.*

strongly suggest that the long-term variations of FA ion motions are driven by a large-scale neutral wind that flows from dayside to nightside.

4.4 Discussion and Conclusions

In Section 4.3, we have shown some characteristics of the FA ion motions in the ionosphere: 1) relatively stable, weak downward FA ion motions are seen in the northward electric field region, while predominantly upward ion motions with intense, sporadic upward FA velocity fluctuations are observed in the southward electric field region, 2) this sporadic upward FA flow does not have one-to-one correspondence with either the enhancement (or reduction) of the electric field (equivalently the enhancement of the ion temperature) or that of the electron density; 3) the total pressure gradient points in the direction of the FA ion motions, but the diffusion velocity due to the pressure gradient does not at all account for the observed speed of the upward FA flow, 4) an ESR and KST comparison strongly suggests that the long-term

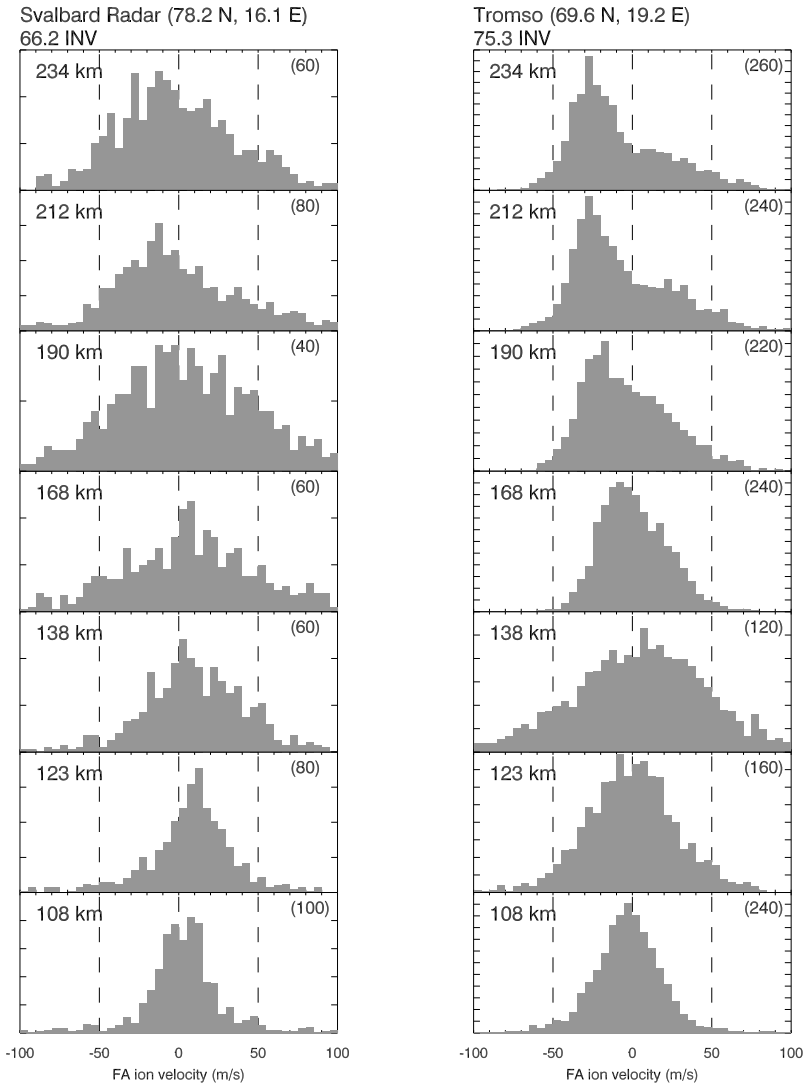

Figure 4.10: *Histograms of the FA ion velocities obtained from the ESR (left) and KST (right) radars at seven altitudes.*

FA ion motions are likely driven by the large-scale day-to-night neutral wind.

First, we will discuss the ion diffusion velocity for the case shown in Fig. 4.2. Figure 4.11 shows the relationships between the FA gradients of the plasma pressures and the FA velocity at 212 km height. The ion, electron, and total pressure gradients are defined as $\nabla P_i = P_i(234\text{km}) - P_i(190\text{km})$, $\nabla P_e = P_e(234\text{km}) - P_e(190\text{km})$, $\nabla P_T = \nabla P_i(234\text{km}) + \nabla P_e(190\text{km})$, where $P_{i,e} = N_e \kappa T_{i,e}$ and all three gradients are positive upward. Both the ion and electron pressure gradients and hence the total pressure gradient increase with a decrease of the FA ion velocity. In other words, the FA ion velocity (positive upward) increases with an increase of the upward pressure gradient force – ∇P. As shown in Figs. 4.5, 4.6 and 4.7, this is caused by dramatic changes of the electron density and of the electron and ion temperatures, particularly for upward FA flows. The degree of correlation between the FA ion velocity and

the pressures is different, however, for the ion pressure and the electron pressure. The ion pressure gradient rather linearly and monotonically decreases (in other words, upward force increases) with an increase of the FA velocity for both negative and positive velocities. The electron pressure gradient, causing the ambipolar diffusion, has a stronger correlation to the downward FA ion motion than to the upward FA ion motion. This is why the downward FA ion motion rather than the upward FA ion motion has stronger dependence on the total pressure gradient.

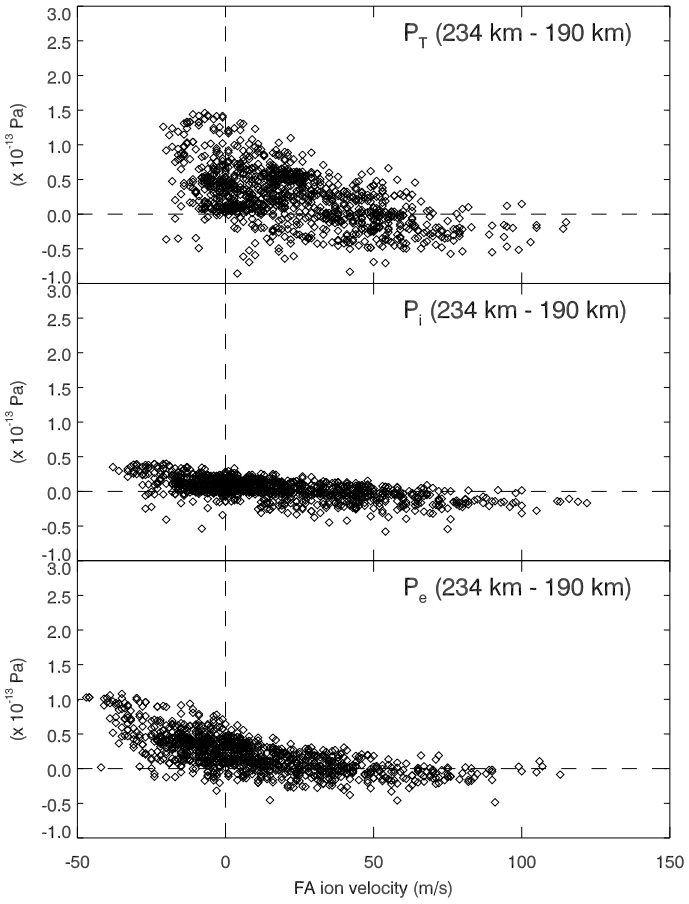

Figure 4.11: *Relationships between the FA gradients of the plasma pressures and the FA velocity at 212 km height.*

The diffusion velocity at the altitude of 190-212 km for $\nu_{in} = 1$ calculated from the CP-1 data obtained on April 20, 1993 is 1 ~10 m/s. Considering the actual collision frequency is supposed to be between 1 and 10 Hz (see Fig. 1.2), the diffusion velocity amplitude can be one-tenth of the velocity calculated here.

One of our interests is how the frictional heating can affect the FA ion motions, particularly short-term (intermittent) variations sometimes exceeding 100 m/s as shown in Fig. 4.2. The frictional heating can work at least in two ways. One way is directly heating ions,

which results in an increase of the ion pressure and hence the ion diffusion velocity. The other way is heating the neutrals, making vertical (or FA) and horizontal pressure gradients of neutrals, which drive the neutrals hence the ions through drag. The present results cannot be explained by the former possibility, since the diffusion velocity is much smaller than the FA ion velocity. It should be noted, however, that the frictional heating actually takes place in the *F*-region as shown in Fig. 4.12. Indeed, the ion temperatures at 234 km, 168 km and 138 km increase (or decrease) simultaneously with increasing (or decreasing) the electric field strength, as was already reported for one height by *Baron and Wand* [1983], clearly showing that the frictional heating occurs instantly (within the data time resolution of 2-min in the present analysis) [*e.g.*, *Lathuillere et al.*, 1986]. That is, the frictional heating does work in the *F*-region but does not drive directly the FA ion motion concerned. It should also be noted, however, that the tendency shown in Fig. 4.12 is different from a previous satellite result [*Killeen et al.*, 1988], where the frictional heating comes into effect around regions of plasma flow shear. Since the ion diffusion velocity is too small to explain the short-term FA ion motions, the only possible force to drive them is the neutral-wind drag.

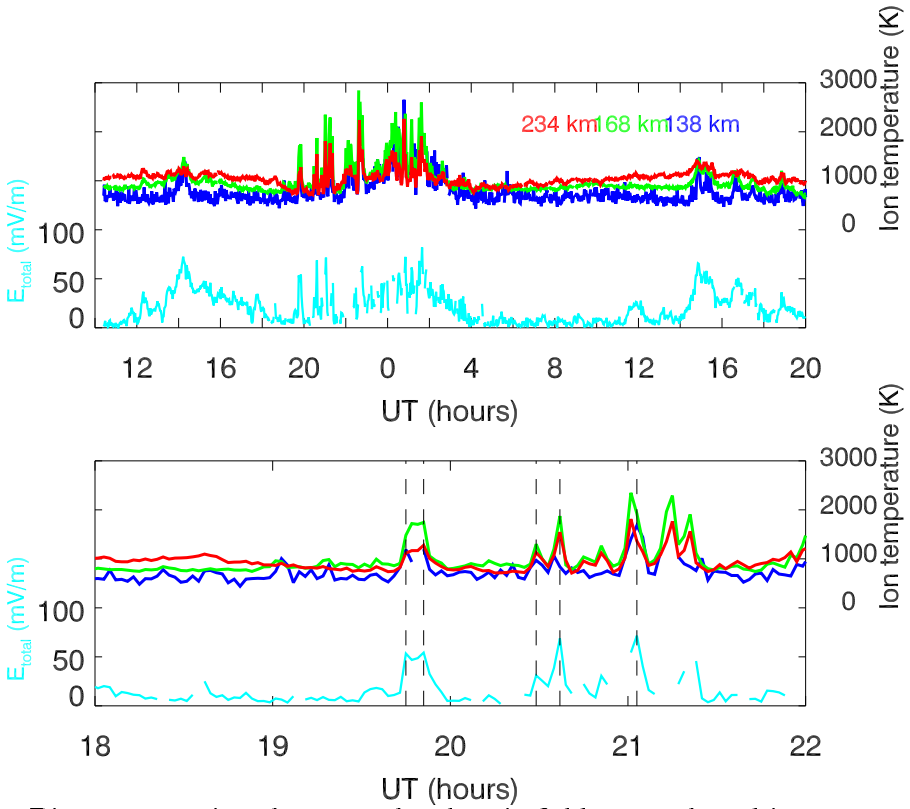

Figure 4.12: *Direct comparison between the electric field strength and ion temperatures at 138 km, 168 km and 234 km on April 20-21, 1993.*

The latter possibility, that is, heating the neutrals by frictional interactions and thereby creating a pressure gradient of neutrals, may also be difficult to realize, since the characteristic time of the energy transfer from the plasmas to the neutrals is relatively long (a few hours).

However, 3-D model calculations such as those by *Sun et al.* [1995], who showed that both ion drag and Joule heating play essential roles in generating flows and waves, may be necessary to exclude this possibility.

It should be noted that an upward or downward FA ion motion can be driven by either a purely horizontal neutral wind, a purely vertical wind, or a combination of these winds, since the magnetic field line has a 12° offset angle from the vertical at Tromsø. If a purely horizontal neutral wind drives ions in the FA direction, $V_{//} = U_{hor} \cos(90° - 12°) = 0.21\ U_{hor}$, where U_{hor} is the horizontal neutral-wind velocity. This means that the neutral-wind velocity must be about 5 times larger than the FA ion velocity and hence, for the event shown in this paper, the horizontal neutral wind should have had intermittently changed its velocity and direction between 500 m/s and -500 m/s in the *F*-region. On the other hand, if a purely vertical neutral wind drives the ions in the FA direction, $V_{//} = U_{vert} \sin(90°\text{-}12°) = 0.98\ U_{vert}$, where U_{vert} is the vertical neutral-wind velocity, then the neutral-wind velocity will be nearly the same as the FA ion velocity. It is unfortunately not possible only from the ion motion to distinguish whether the FA ion motion concerned is driven by a horizontal or vertical neutral wind.

There are several possible physical processes that drive these horizontal and/or vertical motions of neutrals. One is the large-scale thermospheric motion from day to night primarily due to the pressure gradient between the day and night [*e.g.*, *Smith and Sweeney*, 1980; *Dickinson et al.*, 1984]. This day-to-night thermospheric motion is thought to drive large-scale downward FA ion motions in the dayside and upward FA ion motions in the nightside, and it is modified considerably by plasma convection [*Dickinson et al.*, 1984]. The comparison of the FA ion motions between the ESR and KST strongly suggest this mechanism is responsible for the long-term trend of the FA ion motions. However, this day-to-night thermospheric motion itself may not produce the intermittent variations of the FA upward velocity considered here.

One of the possible mechanisms to create the short-term upward FA ion motions in the southward electric field region is blocking of the large-scale day-to-night horizontal neutral-wind that penetrates into the southward electric field region by a high pressure of neutrals (Fig. 4.13). This blocking of the neutral wind may result in its slowing down (Fig. 4.13b) or even stopping (Fig. 4.13c) the neutral wind beyond the blocking region depending on relative location between the blocking area and the observation point, and hence the FA ion flow is decreased or ceased. This blocking of the neutral wind can also enhance upward FA ion motions when a high pressure area is created somewhere else and blocked non-compressible neutral winds get around the high pressure area and stream towards the observation point. The high pressure region of neutrals can be created either by frictional heating or by incident electron heating, both of which frequently occur in the southward electric field region around midnight. This mechanism shown in Fig. 4.13 can explain why the fast, short-term FA ion motions seen in the southward electric field region do not have one-to-one correspondence to

Figure 4.13: *One of the possible mechanisms to create short-term upward FA motions in the southward electric field region by blocking of the large-scale day-to-night neutral-wind motion penetrating into the southward electric field region by a high pressure area of neutrals, resulting in (b) slowing down or (c) even stopping the neutral wind beyond the blocking region.*

the local frictional heating.

4.5 Summary

We have determined the characteristics of the FA ion motions in the *E*-and *F*-region (below the *F*-region peak) ionosphere based on an analysis of ESR and KST data. The results obtained are summarized as follows.

1. Sporadic/burst upward FA ion motions are observed in the regions of southward electric field enhancement, while relatively stable downward FA ion motions are seen in regions of northward electric field enhancement.

2. The long-term (diurnal) variations of these upward and downward FA flow of ions are likely driven by the large-scale day-to-night thermospheric wind, but the driving mechanism(s) of each short-lived upward flow is not yet understood. Each short-lived

upward FA flow has neither one-to-one correspondence to an enhancement (or depletion) of the electric field nor to a change of electron density.

3. The total pressure gradient is likely favorable for the direction of the FA ion motions, but the diffusion velocity due to the pressure gradient does not account for the observed speed of the upward FA flow.

4. The speed of the ambipolar diffusion is significantly stronger in the downward FA flow than in the upward flow.

Chapter 5

Generation of the wavelike structures during auroral activity

5.1 Introduction

In this chapter, we investigate the relations between gravity waves (GWs) and auroral activity by comparing data on auroral morphology that was obtained with an all-sky auroral camera with data that was obtained simultaneously with the EISCAT radar. The field-aligned neutral-wind velocity is estimated using Eq. (1.6) on the basis of data from the EISCAT radar and MSIS model.

The data set used here was restricted to geomagnetically quiet intervals. During geomagnetically disturbed intervals, at high latitudes, all waves that have oscillation periods longer than the Brunt-Väisälä period are not recognized as GWs. If particle precipitation and the electric field are enhanced periodically, thermal expansions of the local atmosphere can cause periodic neutral-wind oscillations synchronized with enhancements of the geomagnetic activity. It is thus important to consider effects of the disturbances in the ionosphere to investigate GWs at high latitudes.

Section 5.2 describes the instrumentation. Section 5.3 describes the theoretical model for GWs that was presented by *Francis* [1974]. Section 5.3 also describes the analysis method we used for estimating the distance to the region in which the GWs were generated. Data provided by the EISCAT radar and the all-sky auroral camera are shown in Section 5.4. We try to identify the source region in which the GWs were generated using all-sky images and GW models in Section 5.5.

5.2 Instrumentation

Simultaneous observations with the EISCAT radar, an all-sky auroral camera, and the IMAGE magnetograms were conducted in Northern Scandinavia on 1 and 29 March, 1995. The observation mode of the EISCAT radar in use was CP-1-K, which provided a three-dimensional velocities of ions at an altitude of 275 km using the three receivers (at Tromsø, Kiruna, and Sodankylä). The electric field is derived from the velocity vectors of the ions, under the assumption that the ions and electrons are moving according to $\boldsymbol{E}\times\boldsymbol{B}$ drift alone. The ionospheric values were obtained from an incoherent scatter spectrum integrated over 2 min. All-sky auroral camera records obtained at Kilpisjärvi (60.0° N, 20.8° E) were used. The CP-1-K antenna beam intersected the ionosphere at an altitude of 110 km about 77 km northwest of Kilpisjärvi.

5.3 Analysis method

5.3.1 Model of atmospheric gravity waves by Francis [1974]

Thermal expansions due to frictional and particle heating as well as ion drag due to the Lorentz force are known to contribute to the generation of GWs, but their relative importance is still not fully understood [*Williams et al.*, 1988]. Here, we estimate wave characteristics using the two-dimensional, meridional (x) and vertical (z), model of *Francis* [1974], assuming that the Lorentz force alone generates GWs.

In this model, the equations of momentum, energy, and mass conservation with respect to neutrals are used to calculate neutral-wind oscillations generated by the Lorentz force. The Lorentz force is a function of the auroral-electrojet current, which has a simple time variations in this model; it is null at time $t \leq 0$ then remains constant at time $t > 0$. The auroral-electrojet current in this model is assumed to be zonal as a line source. The Coriolis force in the momentum equation is neglected. The neutral atmosphere is assumed to have two layers with different temperatures; the height (z_0) of the boundary between them is at 150 km. The altitude (z_s) of the peak auroral current is assumed to be 110 km. The background neutral-wind velocity is set to zero throughout the calculation.

The three equations in the GW model are linearized through Fourier transformation in time, assuming perturbations of pressure and mass density of neutrals. This linearization gives a single equation for $p^{'}/p_0$ ($p^{'}$ is the perturbation term of pressure of neutrals, and p_0 is the equilibrium one) [*Chimonas and Hines*, 1970]. *Francis* [1974] found that when a source function that is representative of the Lorentz force is convolved with Green's function, $p^{'}/p_0$ satisfies

$$\frac{p^{'}(x,z,t)}{p_0(z)} = \left(\frac{p_0(z_s)}{p_0(z)}\right)^{1/2} |\overline{T}| \frac{J\gamma\omega_{b1}B_{z_s}t}{2\pi {C_1}^2\rho_0(z_s)x} \frac{sin[\omega_{c2}t + \omega_{c1}(t^2 - {t_L}^2)^{1/2} + \phi]}{\omega_{c2}(t^2 - {t_L}^2)^{1/2} + \omega_{c1}t}, \tag{5.1}$$

where J is the total auroral current integrated along the line source, γ is the ratio of specific heats ($\simeq$ 1.66), ω_b is the Brunt-Väisälä frequency, B_{z_s} is the magnitude of the geomagnetic field at an altitude of z_s, C is the speed of sound, ρ_0 is the equilibrium term of mass density of neutrals, and x is the distance from the source along the meridional direction. $|\overline{T}|$ is the magnitude of the transmission coefficient for waves at z_0, and ϕ is defined by the equation $\overline{T} = |\overline{T}| \exp(i\phi)$. Subscripts 1 and 2 respectively represent the layers below and above the boundary height z_0. The terms ω_{c1}, ω_{c2}, and t_L are defined as

$$\omega_{c1} = \omega_{b1}(z_0 - z_s)/x, \tag{5.2}$$

$$\omega_{c2} = \omega_{b2}(z - z_0)/x, \tag{5.3}$$

and

$$t_L = (\omega_{a1}/C_1\omega_{b1})\,x, \tag{5.4}$$

where ω_a is the acoustic-cutoff frequency. We focused on the velocity perturbation due to a GW, which is related to $p^{'}/p_0$, shown in Eq. (5.1), with the simple formula,

$$u^{'}(x,z,t) = \frac{{C_2}^2\overline{k_x}}{\gamma\overline{\omega}} \frac{p^{'}(x,z,t)}{p_0(z)}, \tag{5.5}$$

where

$$\overline{\omega} = \omega_{c2} + \frac{\omega_{c1}t}{(t^2 - {t_L}^2)^{1/2}} \tag{5.6}$$

and

$$\overline{k_x} = \frac{\overline{\omega}t_L(\overline{\omega} - \omega_{c2})}{x[(\overline{\omega} - \omega_{c2})^2 - {\omega_{c1}}^2]^{1/2}}. \tag{5.7}$$

In the present work we assumed C_1 = 310 m/s, C_2 = 900 m/s, ω_{b1} = 1/600 s^{-1}, and ω_{b2} = 1/900 s^{-1}. Because we did not compare modeled and observed amplitudes of $u^{'}$, J was simply set to 10^5 A.

The ray path of $u^{'}$ can be either direct or earth-reflected, but we took into account only direct waves in our calculation on neutral-wind oscillations because the earth-reflected waves disperse their energy before reaching the F-region [*Francis*, 1974].

5.3.2 Distance to the source

Bertin et al. [1983] showed that the distance Ds between the observing point and the source region to generate neutral-wind oscillations can be expressed as,

$$Ds = \frac{z_{obs} - z_s}{tan\,\theta}, \tag{5.8}$$

where z_{obs} is the altitude at which neutral-wind oscillations are observed, and θ is the upward-propagation angle from the horizontal plane. If the wave packet is assumed to propagate straight from the source region, θ is defined as the ratio of the meridional-group velocity to the vertical one.

The phase for GWs shifts linearly with height above about 200 km because of the small vertical gradient of the temperature of neutrals. This suggests a stable vertical phase velocity v_{pz} with altitude. The vertical wave number k_z is expressed as $2\pi\omega/v_{pz}$. To derive the meridional wave number k_x, we substituted k_z into the equation of the dispersion relation for GWs given by *Hines* [1960] (see Appendix A):

$$k_x{}^2 = \frac{\omega^2}{\omega_b{}^2 - \omega^2} k_z{}^2 + \frac{\omega^2}{C^2} \frac{\omega_a{}^2 - \omega^2}{\omega_b{}^2 - \omega^2}. \tag{5.9}$$

The meridional and vertical group velocities, v_{gx} and v_{gz}, were derived from $\partial\omega/\partial k_x$ and $\partial\omega/\partial k_z$, respectively.

5.4 Results

We investigated relations between characteristics of neutral-wind oscillations observed with the EISCAT radar and auroral activities for two observation intervals: 1800 to 2200 UT on 1 March 1995 (case 1) and 1130 to 1600 UT on 29 March 1995 (case 2). All-sky auroral images obtained at Kilpisjärvi were available for case 1, but because of daylight not for case 2.

5.4.1 Case 1 (1800 – 2200 UT on 1 March 1995)

Electromagnetic energies that related to the generation of neutral-wind oscillations detected with the EISCAT radar cannot be observed directly with the radar itself in the CP-1-K mode because the source region is far from the observing point. One can, however, investigate relations between characteristics of the observed oscillations and the auroral distributions using EISCAT CP-1-K radar data together with all-sky images.

Some of the all-sky images for case 1 are shown in Fig. 5.1. They show that, from 1857 to 1907 UT, at least two auroral arcs were present aligned in the east-west direction the brighter one being $\simeq$ 100 km south of the zenith and the fainter one being in the zenith. At 1908 UT the arc in the zenith brightened significantly and became distorted through a poleward motion of $\simeq$ 50 km. After this time the all-sky image showed diffuse aurora

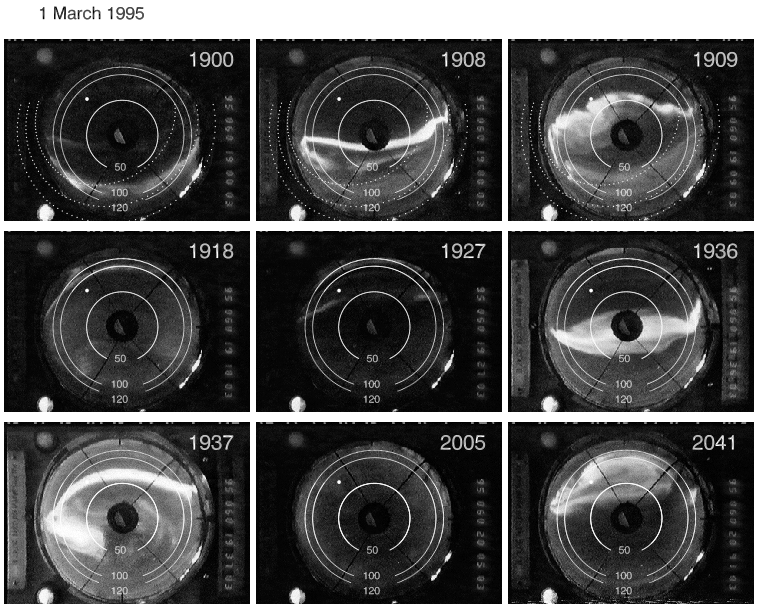

Figure 5.1: *All-sky camera images taken at Kilpisjärvi at 1900, 1908, 1909, 1918, 1927, 1936, 1937, 2005, and 2041 UT. North is toward the top of the page; east is to toward the right. The white dot indicates the Tromsø field line at an altitude of 110 km. The three circles shown with solid lines indicate distances of 50, 100, and 120 km from the zenith at Kilpisjärvi. The dotted curves indicate distances of 140, 200, and 290 km from the Tromsø field line at an altitude of 110 km.*

until 1918 UT when several east-west aligned arcs appeared and began to drift steadily equatorward at a few hundred meters per second. The most equatorward arc appeared to cross the EISCAT beam at 1924 UT (not shown here) while the most poleward arc appeared to cross the beam at 1927 UT. At 1936 UT, the most equatorward arc in the EISCAT field of view broke up and a new arc appeared $\simeq$ 70 km poleward of the zenith; subsequently diffuse auroras were seen over the field of view of the all-sky camera from 1945 to 2040 UT. At 2041 UT, another breakup occurred a little poleward from the region where the 1936 UT breakup had occurred, and a relatively intense aurora covered almost half the field-of-view shortly thereafter. This breakup was not accompanied by rapid motion of the auroras.

Figure 5.2 shows time variations in electric field, electron density, and electron and ion temperatures as well as the field-aligned component of the neutral-wind velocity derived from Eq. (1.6). The Lomb periodogram [*Hernandez*, 1999] was applied to the field-aligned neutral-wind velocities, shown in Fig. 5.2d, in an altitude range from 165 to 253 km, in which oscillation periods shorter than 13 min (the typical Brunt-Väisälä period in the *F*-region) were filtered out. The thick solid and dash-dotted lines in Fig. 5.2d are discussed in

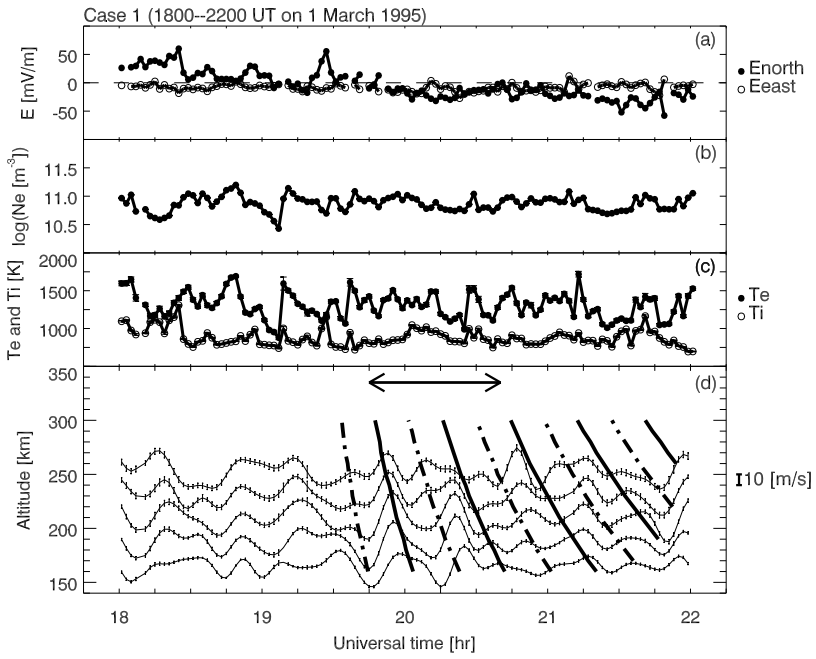

Figure 5.2: *For case 1: (a) Electric field derived from EISCAT radar data between 1800 and 2200 UT on 1 March 1995. Solid circles indicate the meridional component; open circles indicate the zonal component. Positive values are northward and eastward. (b) Electron density at an altitude of 209 km derived from the EISCAT radar. (c) Electron (solid circles) and ion (open ones) temperatures at an altitude of 209 km derived from the EISCAT radar. (d) Superposition of modeled phase surfaces on observed oscillations in field-aligned neutral-wind velocity. The modeled phase surfaces with a minimum value are plotted with thick dash-dotted lines, and those with a maximum value are plotted with thick solid lines. The base line of the observed oscillations at an altitude of 165 km corresponds to a height of 165 km, and the base lines for the other altitudes correspond in the same way. Positive wind is upward, along the field line.*

Section 5.5.1. When the brightening region moving steadily poleward (from 1857 to 1907 UT) and equatorward (from 1918 to 1935 UT) crossed the EISCAT radar observing point, the electric field had peak values, which increased the ion temperature due to frictional heating.

Around 2000 UT, when diffuse aurora were observed, the field-aligned neutral-wind velocities oscillated with relatively large amplitudes. Downward propagation of the phase with time was seen in the field-aligned neutral-wind velocities. The velocity at an altitude of 165 km had a peak near 2000 UT, whereas that at 231 km had a peak about 7 min earlier.

To investigate the wave characteristics in more detail, the Lomb periodogram was applied to the velocities observed from 1945 to 2040 UT (shown in Fig. 5.2 with an arrow). Figure 5.3 shows the spectra obtained at altitudes of 209 (solid line) and 231 km (dashed line). The spectra at the other altitudes have peaks at the same oscillation periods with different amplitudes. The vertical dotted line shows the typical Brunt-Väisälä period in the *F*-region. While the spectra for both altitudes are relatively broad, they have a peak amplitude at an

Figure 5.3: *Spectra from the Lomb periodogram applied to field-aligned neutral-wind velocities at altitudes of 209 km (solid line) and 231 km (dashed line). Open circles show results for case 1, and solid circles show results for case 2. The vertical dotted line at a period of 13 min shows the typical Brunt-Väisälä period in the F-region.*

oscillation period of 24 min, obviously longer than the typical Brunt-Väisälä period.

The downward propagation of the phase with time and the oscillation period longer than the typical Brunt-Väisälä period are general characteristics of GWs, which imply that the observed oscillations from 1945 to 2040 UT are GWs.

Figure 5.4 shows the height profile of the phase at an oscillation period of 24 min. The vertical phase velocity is almost stable with height because the phase shifts approximately proportionally with height. The vertical phase velocity for the oscillation period of 24 min was about 190 m/s based on a linear fit, as shown by the dashed line in Fig. 5.4 (The cross-correlation coefficient was 0.973.). Height profiles of the phase at oscillation periods of 27 and 22 min (not shown here) also showed shifts proportional with height. The vertical phase velocities for oscillation periods of 27 and 22 min were respectively about 170 and about 190 m/s.

We could derive the distance between the observing point and the region generating the observed oscillations using the method described in Section 5.3.2, although we could not estimate the propagating direction of the observed oscillations because of the observation being fixed to look along the geomagnetic-field line. This distance is listed in Table 5.1, along with the values of the other wave parameters. The meridional wavelength λ_x $(= 2\pi/k_x)$ and the phase velocity v_{px} $(= 2\pi\omega/k_x)$ were about 160 km and about 110 m/s. Distances for oscillation periods of 27 and 22 min were about 290 and about 140 km, respectively. Compared with the distance for an oscillation period of 24 min, the differences are about 90 and about 60 km.

From 1800 to 1945 UT the electric field varied considerably with time, as shown in

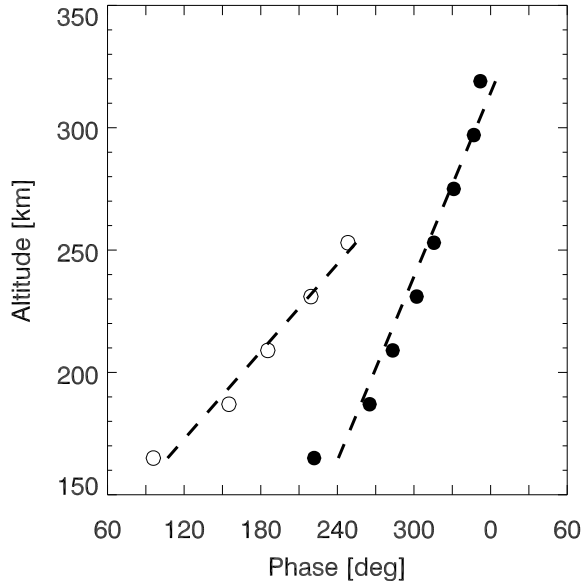

Figure 5.4: *Height profile of the phase for cases 1 (open circles) and 2 (solid circles). Dashed lines show the height profiles used in this paper.*

Fig. 5.2a. The neutral-wind oscillations observed during this interval may have resulted from not only local heating but also propagation of some neutral-wind perturbations from distant sources. From 1945 to 2040 UT, when the all-sky images showed diffuse auroras, the perturbations in the electric field were smaller than those in the disturbed interval. This suggests that wave propagation from distant sources was more important for the neutral-wind oscillations observed from 1945 to 2040 UT than local heating.

Table 5.1: *Results of Lomb periodogram analysis from 1945 to 2040 UT for case 1 and from 1230 to 1400 UT for case 2.*

		Case 1	Case 2
Dominant period	[min]	24	32
Distance	[km]	$\simeq$ 200	$\simeq$ 260
Meridional wavelength		$\simeq$ 160	$\simeq$ 230
– phase velocity	[m/s]	$\simeq$ 110	$\simeq$ 120
Vertical wavelength	[km]	$\simeq$ 270	$\simeq$ 510
– phase velocity	[m/s]	$\simeq$ 190	$\simeq$ 270

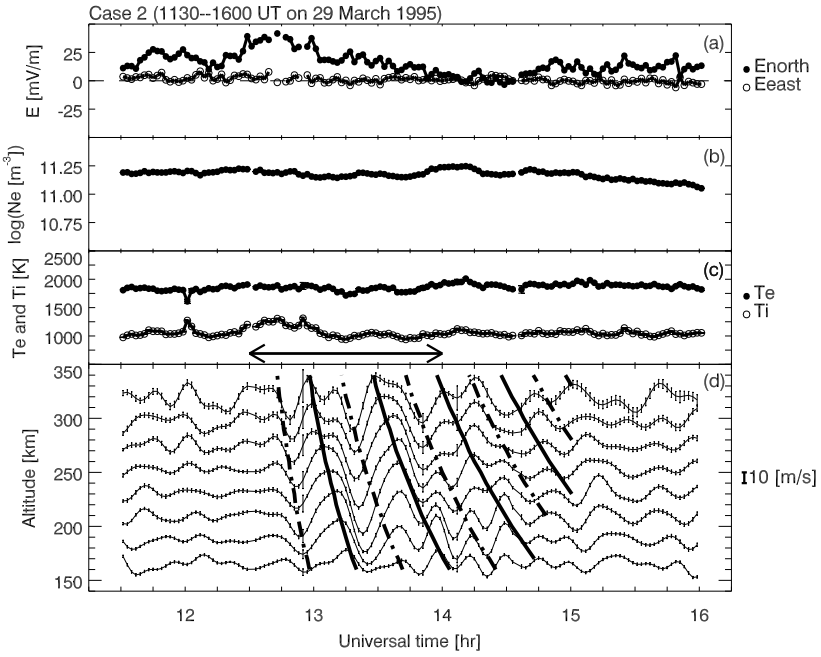

Figure 5.5: *As for Fig. 5.2, but for case 2 (between 1130 and 1600 UT on 29 March 1995). The altitude range for the field-aligned neutral-wind velocity is from 165 to 319 km.*

5.4.2 Case 2 (1130-1600 UT on 29 March 1995)

We could not identify the auroral distributions around the source region because of daylight. There is, however, a method that can be used to investigate the relationship between the characteristics of observed neutral-wind oscillations and geomagnetic activity, as explained in the following.

The electric field increased, from 1145 to 1200 UT and from 1230 to 1300 UT (Fig. 5.5a). The electric field during the latter period reached about 40 mV/m, a level which (by frictional-energy dissipation) significantly increased the ion temperature in the *F*-region (Fig. 5.5c). According to the IMAGE magnetograms [*Lühr et al.*, 1998 and references therein], the frictional energy seemed to dissipate in the ionosphere not only over the EISCAT radar site but also in the other regions. From 1230 to 1300 UT the Y-components (EW-components) measured from Bjørnøya (BJN; 74.5° N, 19.2° E) to Oulujärvi (OUJ; 64.5° N, 27.2° E) had comparatively large amplitudes, which seemed to decrease going equatorward and poleward.

After 1300 UT the field-aligned neutral-wind velocity in the *F*-region began to oscillate with remarkably large amplitudes, as shown in Fig. 5.5d. The oscillations were observed from altitudes of 165 to at least 319 km, and their amplitude increased gradually with increases of altitude. While they were observed, the electric-field magnitude decreased gradually, and the electron density and electron temperature in the *F*-region did not show any remarkable enhancements due to energetic-particle precipitation. Periodic perturbations in the auroral-

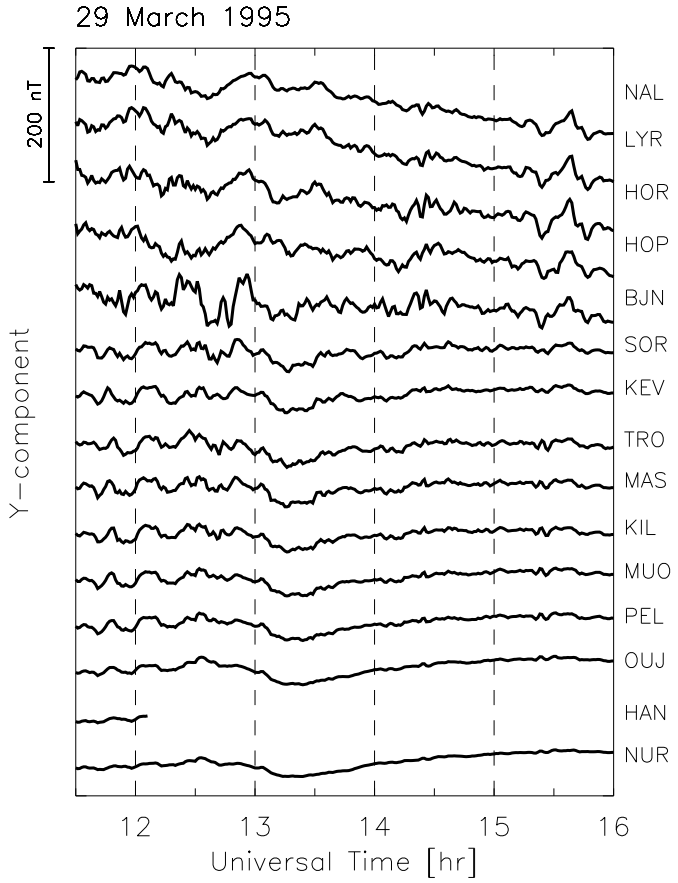

Figure 5.6: *For case 2, the Y-components, i.e., EW-components, of magnetograms from the IMAGE network.*

particle precipitation and the electric field thus contributed little to the generation of the observed neutral-wind oscillations. The oscillations appear to have a downward propagation of the phase with time. Figure 5.3 shows that the Lomb periodogram spectra of the oscillations observed from 1230 to 1400 UT (shown in Fig. 5.5 with an arrow) at altitudes of 209 (solid line) and 231 km (dashed line) had a peak amplitude at an oscillation period of 32 min, which was obviously longer than the typical Brunt-Väisälä period. These results show that observed oscillations had the general characteristics of GWs.

The vertical phase velocity for an oscillation period of 32 min, which was obtained using the height profile shown in Fig. 5.4, was about 270 m/s (The cross-correlation coefficient between the observed phase and fitted line was 0.986.). The estimated distance between the observing point and the source region for generating observed oscillations was about 260 km (Table 5.1). The meridional wavelength was about 230 km, and the meridional phase velocity was about 120 m/s. For oscillation periods of 35 and 29 min, the vertical phase velocities were about 200 and about 370 m/s, respectively, and the distances were about 430 and about

150 km, respectively. The distances differed from that for an oscillation period of 32 min by about 170 km and about 110 km, respectively.

5.5 Discussion

5.5.1 Assessing the validity of the hypothesis about the wave-source region

The neutral-wind velocity estimated from EISCAT radar data in the *F*-region oscillated with periods of 20-30 minutes, and neutral-wind oscillations had wavelengths of several hundred kilometers. These values are typical for medium-scale GWs according to the classification by *Hunsucker* [1982]. These oscillations were associated with increases in the plasma temperature and density. To assess the validity of the hypothesis that the observed neutral-wind oscillations were generated in the expected source region, we used three analysis techniques. First, we investigated the auroral activity around the expected source region for case 1 using all-sky auroral images. Second, the distance between the observing point and the generation region was calculated for case 1 using the model of *Kato et al.* [1977], and it was compared with the distance tabulated in Table 5.1. Finally we compared, for both cases, the observed phase line with that calculated using the model of *Francis* [1974].

- Using all-sky auroral images

  The estimated distance from the observing point to the source region for case 1 was 140-290 km. The meridional phase velocity was about 110 m/s, and thus the front of the oscillations observed from 1945 to 2040 UT should have reached the observing point 21-44 min after leaving the source region if the phase velocity remained constant during the propagation. Hence, the source should have appeared at 1900-1920 UT at a distance of about 140-290 km.

  According to the all-sky auroral images obtained between 1900 and 1920 UT, the auroral arc extended in an almost zonal direction from 1900 to 1908 UT appears to be the generator of the neutral-wind oscillations observed with the EISCAT radar. The distance between the observing point and the auroral arc is roughly consistent with the estimated distance, as shown in Fig. 5.1. Although it is difficult to estimate effects of the thermal expansions and the momentum transfer between ions and neutrals on motions of neutrals quantitatively using the present data set, we can presume that Joule and particle heating and the Lorentz force enhance in the vicinity of the auroral arc, and that these mechanisms are candidate generator of the observed oscillations. The rapid motion of the auroral arc at 1908 UT is also the candidate generator of the observed oscillations. Although the relative importance in the three mechanisms – Joule and particle heating, the Lorentz force, and the rapid motion – for the generation of the observed oscillations was not found from the present observation, it is concluded

that the auroral arc appeared from 1900 to 1908 UT has affected the generation of the observed oscillations strongly.

- Using the model of *Kato et al.* [1977]

  Within two minutes from 1907 to 1909 UT on 1 March 1995, the position of the intense arc changed dramatically poleward as described in Section 5.4.1. There are several possible explanations on these changes. Because the electromagnetic energy dissipated into the arc must be driven from wave and particle energy stored within flux-tubes in the magnetotail, the relative movement of the arc with respect to the flux-tubes must be one of the candidate hypotheses of the change in the observed-arc position [*Elphinstone et al.*, 1996]. Another candidate hypothesis is with respect to the background convection of plasma flow. If there are several flux-tubes in which the energy flux of the precipitating electron fluctuates with time, the arc can be seen as moving like an electric newsboard. Thus we cannot identify which physical process dominated in the present case only using data from the all-sky camera. In this paragraph, we assume that the flux-tubes have moved poleward rapidly. If this motion is the generator of the observed oscillations, we can estimate the distance between the observing point and the generation region using the model of *Kato et al.* [1977]. The position where a line source moving at a speed of Vo can generate GWs with a phase velocity of Cs can be expressed by the following equation [*Kato et al.*, 1977]:

$$\frac{r}{Cs} = \frac{r\ cos\ \alpha + D}{Vo}, \tag{5.10}$$

  where r is the distance between the observing point and the generation region, and $(\pi$ - $\alpha)$ is the angle between the direction of the source motion and a line between the observing point and the generation region. An intense auroral arc extending in an almost zonal direction is the most likely candidate for the line source in the present observation. The motion of the line source in the model agrees well with the actual change of the auroral-arc position. In this model, the line source is assumed to drift without any time variations in the magnitude. Although the auroral emission intensity may not be directly proportional to the magnitude of the auroral-electrojet current and to the Joule heating rate, this assumption may be inconsistent with actual time-variations in the magnitude of the line source according to the all-sky camera images (see Fig. 5.1).

  For case 1, when the rapid change of the intense auroral-arc position occurred at 1908 UT, the arc was on the equator side of the EISCAT observing point, thus an angle α of 0° corresponds to equatorward from the observing point. If the arc moves poleward at a constant velocity, it arrives at a distance D from the observing point after a time t. According to the all-sky auroral images, the Vo for case 1 was about

800 m/s. The estimated distance between the observing point and the arc just before the rapid change in position of the arc was about 200 km. Thus after 21-44 min, D is about 800-1900 km. The Cs for case 1 was about 110 m/s (see Table 5.1) thus at α = 0° the distance r is $\frac{11}{69}D$, or about 160-330 km. This range includes the estimated distances listed in Table 5.1.

- Using the model of *Francis* [1974]

  In Figs. 5.2d and 5.5d, the neutral-wind oscillations calculated using the model of *Francis* [1974] are compared with the observed ones for cases 1 and 2. The distances between the observing point and the source region, which were used for calculating the modeled phase lines, were 200 km for case 1 and 260 km for case 2. These values were estimated from the dispersion relation applied to the observed oscillations during limited intervals: from 1945 to 2040 UT for case 1 and from 1230 to 1400 UT for case 2. The wave source was assumed to be the Lorentz force in the model. This assumption seems to be acceptable because the characteristics of observed oscillations were categorized in medium-scale GWs, which can be generated by the Lorentz force more effectively than by Joule heating [*Jing and Hunsucker*, 1993].

  For case 1, from 1945 to 2040 UT there were approximate peak-to-peak correspondences between the modeled phase line and the one observed at altitudes from 165 to 253 km. For case 2, from 1230 to 1400 UT the modeled phase line seems to agree with the one observed at altitudes from 165 to 319 km. These agreements suggest that the line source in the model can reproduce the phase line similar to the observed one. For case 1, the auroral arc extended in an almost zonal direction from 1900 to 1907 UT, which could be identified as the line source in the model. The agreements also suggest that the generator of the observed oscillations has some consistent properties with ones of the wave source in the model. Effective parameters of the wave source in characterizing neutral-wind oscillations will be discussed in next section.

5.5.2 Effective parameters of the wave source in characterizing neutral-wind oscillations

An evaluation of the consistency of the assumptions with the observations can be directly related to a prediction of some properties of the wave source. This suggests that if the characteristics of GWs – period, wavelength, amplitude, etc. – are measured, we can estimate the wave source, but that is generally quite difficult.

We used two models to assess the validity of the hypothesis regarding the wave-source region under some assumptions. Prediction from these models agreed with results from the observations, although the time variation and the motion of the wave source for both models were considerably simplified using different assumptions. The consistency of these

assumptions for the observations should be discussed.

For case 1, the auroral arc that was estimated as the wave source almost stayed at about 200 km equatorward from the Tromsø site (from 1857 to 1907 UT), then it was seen as changing its position poleward rapidly at 1908 UT. If the observed oscillations were generated in association with the stationary arc, not with the rapid change in position, the motion assumed in the *Francis* model may be more suitable than that in the *Kato* model. If the observed oscillations were generated by the rapid change in position, the motion assumed in the *Kato* model may be more suitable. The wave source was estimated to have turned on at 1900–1920 UT. The above two motions occurred during this interval, thus we cannot identify which motions of the auroral arc were effective in generating the observed oscillations.

The *Francis* model assumes simplified time variations in the auroral-electrojet current, but the current remains constant after its appearance. The wave source assumed in the *Kato* model had no time variations. Electromagnetic energy associated with the auroral arc, however, seems to vary with time according to the emission intensity obtained from the all-sky camera images. Both models may not be suitable with respect to the time variations in the wave source.

For case 2, discussions on time variations in the wave source may be possible using IMAGE magnetometer data (Fig. 5.6), although any discussions on the motion is not possible. The magnetometer at Bjørnøya showed at least two negative peaks during 1230 to 1300 UT, which suggests that auroral-electrojet current had fluctuated with some amplitude and that the time variations assumed in both models may not be suitable.

We cannot discuss the merits of the two model based on the consistency of the assumptions with observation. It is concluded, from the agreement between the predictions and the observations, that the effective parameters of the wave source in characterizing the observed oscillations will be the horizontal distribution of the wave source and the distance between the observing point and the source region. This is because both models use same assumptions for these parameters of the wave source.

5.5.3 Differences between predictions and observations

The models used here did not reproduce all the observed oscillations. Figures 5.2d and 5.5d show that discrepancies between the phase lines from observations and those from calculations using the *Francis* model gradually became obvious with time. One reason for these discrepancies is that the modeled oscillations were reproduced using the distance estimated from the oscillations observed during limited intervals. For the other candidates, we will discuss three explanations for the discrepancies: (i) local ionospheric-perturbations associated with enhancements of the plasma temperature and density, (ii) assumptions of the GW model, and (iii) the propagation of waves from other source regions.

(i) Effects of local ionospheric perturbation: For case 1, the amplitudes of the oscillations observed at altitudes of 165, 187, and 209 km suddenly decreased after about 2040 UT, as shown in Fig. 5.2d. The all-sky auroral image at 2041 UT (Fig. 5.1) showed an auroral intensification, which resulted in the enhancement of the plasma density and temperature and the electric field (Figs. 5.2a-c). This can activate the thermal expansion of the atmosphere and the ion-neutral momentum transfer thus produce neutral-wind oscillations. The oscillations have relatively broad band spectra in the vicinity of the generation source because permitted spectra, as determined by viscous damping, can survive due to the short distance they propagate from the generation source. Neutral-wind oscillations originated from an auroral intensification at 2041 UT might be superimposed on the neutral-wind oscillations observed before an auroral intensification, which can modulate the wave characteristics of the phase and the period.

Even during relatively quiet intervals, from 1945 to 2040 UT for case 1 and from 1230 to 1400 UT for case 2, the electric field and the electron density showed perturbations with small amplitudes. These perturbations may cause discrepancies between the modeled and observed phase lines through local thermospheric heating.

(ii) Assumptions of the GW model: As mentioned in Section 5.3.1, the *Francis* model makes various assumptions. While any of them could produce discrepancies between predictions and observations, here we consider some that are likely to be important.

The model assumes that the Lorentz force is the only source generating GWs, though frictional and particle energy dissipation have also been thought to be a source of GWs. If particle heating significantly affect motions of neutrals in the *F*-region, the source region in the model should be shifted upward from the 110 km altitude given in the model. An upward shift of the source altitude in the model decreases the distance to the source according to Eq. (5.8), and tends to decrease the oscillation period of the modeled GWs.

Background neutral-winds may affect wave characteristics, such as the frequency and the ray-path. For case 1, the mean value of the field-aligned neutral-wind velocity in the *F*-region is positive thus upward along the geomagnetic-field line, which suggests that the background neutral-wind velocity appears to be equatorward. This is consistent with previous works, from FPIs and the EISCAT radar, that equatorward winds are generally dominant during nighttime in the upper thermosphere [*Aruliah et al.*, 1996; *Witasse et al.*, 1998]. The estimated wave-source located at equator side of the EISCAT radar site. This suggests that the observed oscillations propagated poleward, and that the group velocity of the observed oscillations has a component anti-parallel to the background neutral-wind. Evidence for this anti-parallel component can be seen for case 2. The mean neutral-wind velocity is negative, which suggests that the poleward winds appear to be dominant. The magnetograms in Fig. 5.6 show that, from 1230 to 1300 UT, the amplitude of the Y-component seems to have a peak around Bjørnøya (BJN), which is poleward of the EISCAT radar site. This suggests

that the observed oscillations propagated equatorward opposite in direction to the poleward background winds.

The anti-parallel direction of propagation of the wavelike structures causes an upward Doppler-shift of the oscillation frequency and an upward shift of the direction of the group velocity. The effect on the group velocity may reduce the distance between the observing point and the wave-source region in terms of the wavelength. The anti-parallel direction is considered to be one of the reasons for discrepancies between the observed and predicted phase lines.

The model assumes that the height profile of the temperature of neutrals has no vertical gradient above 150 km, and thus that the speed of sound and the Brunt-Väisälä frequency are almost constant regardless of height. This assumption may cause large differences between the assumed and actual temperatures, especially in the lower F-region (150-200 km). This could result in discrepancies between the modeled and observed phase line because the phase and the oscillation frequency are a function of the temperature of neutrals.

The simplifying assumptions required to derive Eq. (5.9) from *Hines* [1960] may also cause discrepancies. This equation is based on the assumption that the horizontal wave number k_x is purely real, which indicates that viscous damping is ignored. This is not held precisely in proportion to the distance from the wave source. Numerical simulations show that GWs generated by Joule energy dissipation attenuate as they propagate with a component in the horizontal direction [*Fujiwara et al.*, 1996]. Interactions among multiple waves are also not considered. *Hines* [1960] assumed an idealized atmosphere taken to be stationary in the absence of waves. The actual atmosphere, however, always has some fluctuations.

(iii) Effects of propagation from other source regions: For case 2 there are notable differences between the modeled phase line and the observed ones after 1400 UT, although significant ionospheric heating was not observed from 1300 to 1600 UT. Thus local heating cannot be the reason for the discrepancy. A possible reason for the difference is that other sources might be generating neutral-wind oscillations. If oscillations propagating from several sources are superimposed at the observing point, the observed oscillations cannot be reproduced by a model that assumes a single source.

5.5.4 Was it possible to generate the observed GWs by the auroral activity at 1927 and 1937 UT for case 1?

Figure 5.1 shows that the region where emission intensity was significantly high changed from being equatorward of the Tromsø radar site to being poleward at 1937 UT, and that the auroral arc extended in an almost zonal direction appeared to move at a few hundred meters per second crossed the EISCAT observing point at 1927 UT. These auroral arc motions affected the local ionosphere. Figure 5.2a-c shows significant enhancements of the electric field, the ion temperature, and the electron density and temperature at those times. These

auroral arc motions, however, are thought not to be significantly related to the generation of neutral-wind oscillations observed from 1945 to 2040 UT. This is because wave characteristics depend on the distance between the observing point and the source region, as concluded in Section 5.5.2. The distance estimated from the spectrum analysis of the observed oscillations is about 200 km, which is obviously different from that at 1927 and 1937 UT.

5.6 Summary

Relations between auroral activity and the generation of neutral-wind oscillations in the auroral *F*-region have been presented using data from the EISCAT radar, the all-sky auroral camera, and the IMAGE magnetometers. The results obtained are summarized as follows.

1. When the ionospheric perturbations were relatively small, the field-aligned neutral-wind velocity estimated from EISCAT radar data oscillated at periods of 24 min for case 1 (from 1945 to 2040 UT on 1 March 1995) and 32 min for case 2 (from 1230 to 1400 UT on 29 March 1995). These oscillation periods were longer than the typical Brunt-Väisälä period in the auroral *F*-region ($\simeq$ 13 min). The observed oscillations showed the downward propagation of the phase with time. Although we could not find conclusive evidence that the observed oscillations were GWs, the wave parameters of observed oscillations were typical for medium-scale GWs according to *Hunsucker* [1982].

2. The values of the wave parameters were derived from the equation of the dispersion relation for GWs applicable to the observed oscillations. These values were used to estimate the distance between the observing point and the source region where the oscillations were generated: about 200 km for case 1 and about 260 km for case 2. For case 1 the all-sky auroral images obtained at Kilpisjärvi showed that the auroral arc extended in an almost zonal direction near the estimated position of the source. Although we could not rule out the possibility of generating the observed oscillations by meteorological sources (see Section 1.2.4), enhancements of electromagnetic energy are considered to be strong candidate source to generate the observed oscillations.

3. The comparison of observed phase lines with predicted ones using models by *Francis* [1974] and *Kato et al.* [1977] showed agreement between the two for both cases. Results from the comparison suggested that effective parameters of the wave source in characterizing neutral-wind oscillations will be the horizontal distribution of the wave source and the distance between the observing point and the source region. This implies that geomagnetic activity at high latitudes is important in generating GWs, as indicated by previous theoretical studies.

Chapter 6

Conclusion and suggestions for future studies

Three investigations on the coupling between the thermosphere and ionosphere in the auroral *F*-region were carried out using data from the EISCAT KST radar, ESR, a scanning FPI, an all-sky camera, and IMAGE magnetometers. The simultaneous observation with the EISCAT radar and the FPI represent the first experiment using optical and radio techniques for targeting on short time-scale oscillations of ions and neutrals in the auroral *F*-region. The comparison between the neutral-wind velocities observed with the FPI and those estimated on the basis of EISCAT radar data suggests that, in the *F*-region, the field-aligned oscillations in ion velocity were due to collisions of ions with neutrals. In the *E*-region, plasma motions are tightly controlled by collisions of ions with neutrals; field-aligned ion velocities observed with the EISCAT radar in the *E*-region almost correspond to the field-aligned component of the neutral-wind velocity. Hence, collisions between neutrals and ions provide the main process to determine the field-aligned ion motions in the *E*- and *F*-regions.

Little frictional energy will thus result from the differences between field-aligned ion and neutral-wind velocities. The ion temperature can be elevated by the relative velocity perpendicular to the geomagnetic field line between ions and neutrals (frictional heating), which is attributed to the electromagnetic force on ions.

According to the statistical analysis of the field-aligned ion velocity in the auroral *E*- and *F*-region, sporadic/burst upward field-aligned ion motions are related to the enhancement of the electric-field strength in the region of southward electric field. The diffusion velocity due to the total pressure gradient in this region does not account for the observed speed of the field-aligned ion velocity. This suggests that motions of neutrals disturbed by the electromagnetic energy in the region of southward electric field enhancement contribute strongly to the sporadic/burst upward field-aligned ion motions.

According to the results of simultaneous observation from the EISCAT radar and the

all-sky camera, the momentum and energy of ions activated in association with auroral arc are considered to contribute strongly to the generation of wavelike oscillations of neutrals. The field-aligned neutral-wind velocities estimated on the basis of EISCAT radar data oscillated with periods of 20-30 minutes when almost no significant perturbations in the electric field were observed. The spectrum analysis of the observed oscillations of neutrals showed the characteristics of propagation of the oscillations. Substituting the parameters of the observed oscillations into the equation representing the dispersion relation for GWs suggested that oscillations of neutrals had been generated at about 200 km from the observing position and had propagated from that source region to the observing position. The all-sky images showed that around that time the auroral arc extended almost zonal direction close to the estimated distance of the source. The comparison of the phase lines as predicted by models of *Francis* [1974] and *Kato et al.* [1977] and observation showed agreement between the two.

The conclusions from three investigations that the basis of this thesis are valuable for understanding the effect of the input of electromagnetic energy from the magnetosphere on the motion of neutrals in the auroral thermosphere. This thesis shows the collision process between ions and neutrals, which is one of the fundamental physical mechanisms in the ionosphere, and relations between thermospheric motions and the auroral activity that is representative of the electromagnetic energy deposited from the magnetosphere. Thus the conclusions of this thesis contribute to our knowledge on thermosphere-ionosphere dynamical coupling. Of course other approaches are necessary for further this knowledge. Electromagnetic energy originating in the magnetosphere is frequently deposited into a localized region of the ionosphere at high latitudes, which causes steep horizontal gradients in the plasma density and temperature. These horizontal gradients cause a divergent flow of neutrals and lead to the growth of the wavelike structures in the motions of neutrals. Because the amplitude and the propagation direction of the waves depend on the magnitude and the horizontal gradient of the electromagnetic energy, it is important to observe horizontal distributions of the energy as well as those of the perturbations of neutrals. We propose three experiments through which one can obtain these horizontal distributions.

1. Simultaneous observation with several optical instruments

   All-sky FPIs detect neutral-wind velocities at several points in the field-of-view, and this information can be used to estimate the horizontal motion of neutrals. All-sky imagers are best tool with which check auroral morphology. Furthermore, they may provide information about the horizontal structure of the electromagnetic energy from the magnetosphere. Because the auroral emission intensity is a function of the energy flux of the precipitating particles, the horizontal structure of the auroral emission intensity observed with the imager at different wavelengths can provide information about the energy flux. The height profile of electron density calculated from the energy flux using an inversion method can be used to obtain the Pedersen conductivity. If the

electric field distributions are given from a model or from observations using VHF and HF radars, we can estimate the horizontal variation of the frictional heating rate.

2. Simultaneous observation with two IS radars

   The ESR observatory has two IS radars; one is fixed to look along the local geomagnetic field line, while it is possible to sweep the other to scan the ionosphere. The field-aligned neutral-wind velocity can be estimated using data from the fixed radar. The field-aligned motions of neutrals calculated from the fixed radar data provide the wave characteristics required to estimate the source region in which the observed waves are generated. Enhancements of ion temperature around the estimated source region are representative of those of the electromagnetic energy from the magnetosphere. It is possible to use the scanning radar to observe enhancements in the ion temperature as long as the field-of-view of the scanning radar covers the estimated source region for the observed waves. While the Joule heating rate cannot be directly calculated using data from the scanning radar, the meridional and height profiles of the ion temperature would allow an estimation of the distributions of source energies for the waves.

3. Comparison between the results of modeled and observed dynamic behavior of thermospheric winds

   Simultaneous observations as described above can be used to estimate the horizontal distributions of electromagnetic energy and of neutral-wind velocity in the auroral thermosphere. IS radars and optical instruments are capable of obtaining data with a time resolution that is shorter than the typical Brunt-Väisälä period, so it is possible to estimate wave characteristics of neutral winds around the observed position. It is, however, difficult to estimate how waves propagate and attenuate from the observational data because the horizontal scale that can be covered with observations may be shorter than the wavelengths. Model-based calculations with a larger horizontal scale are effective for the investigation of the propagation and attenuation.

   The horizontal distribution of electromagnetic energy and the neutral-wind velocity based on observations provides a description of the initial ionospheric and thermospheric conditions required to generate waves. Substituting these initial conditions into models of the dynamic behavior of the neutrals provides the temporal and spatial variations in the neutral-wind velocity. Comparison of observed and modeled perturbations in the neutral wind will improve our understanding of thermosphere-ionosphere coupling for electromagnetic energy input.

Many other experiments may also be useful in the study of the thermospheric response to auroral activity, *e.g.*, IS radar observations in combination with those from optical instruments. All instruments have their advantages and disadvantages in terms of thermospheric

and ionospheric observations. It is important to define precisely what the target of the experiment is.

Appendix A

Dispersion relation for gravity waves

The equation of continuity, momentum, and state for the neutral atmosphere are

$$\frac{\partial \rho}{\partial t} = -\nabla\cdot(\rho \boldsymbol{U}), \tag{A.1}$$

$$\rho\frac{d\boldsymbol{U}}{dt} = -\nabla p + \rho \boldsymbol{g} + \eta\nabla^2\boldsymbol{U} - \nabla\cdot\boldsymbol{\pi}_w - 2\rho\boldsymbol{\Omega}\times\boldsymbol{U} - \rho\nu_{ni}(\boldsymbol{U}-\boldsymbol{V}), \tag{A.2}$$

and

$$p = \rho\kappa T_n/m_n, \tag{A.3}$$

where η is the dynamic viscosity coefficient, $\boldsymbol{\pi}_w$ is the tensor of the momentum flux-density due to waves, and Ω is the constant angular velocity due to the earth's rotation. To derive the dispersion relation for the linear modes of a non-rotating neutral atmosphere on a flat earth, we use several assumptions. First is zero velocity of the vertical neutral-winds: thus $\boldsymbol{U}$ = (v, w, 0). Although this assumption may cause significant errors in wave characteristics derived from the dispersion relation in the case of high geomagnetic activity as mentioned in Section 1.2.4, this assumption is widely used in model calculations. Second is that perturbations of the pressure of neutrals (δp) and density of neutrals ($\delta\rho$) are defined by

$$\delta p = p - p_0 \tag{A.4}$$

and

$$\delta\rho = \rho - \rho_0, \tag{A.5}$$

where p_0 and ρ_0 are the ambient pressure and density, respectively. Eqs. (A.1)-(A.3) can be expressed under these two assumptions retaining terms up to first order in $\delta\rho$ and δp:

$$\frac{\partial(\delta\rho)}{\partial t} + \boldsymbol{U}\cdot\nabla\rho_0 + \rho_0\nabla\cdot\boldsymbol{U} = 0, \tag{A.6}$$

$$\rho_0\frac{\partial v}{\partial t} + \frac{\partial(\delta p)}{\partial y} = 0, \tag{A.7}$$

$$\rho_0\frac{\partial w}{\partial t} + \frac{\partial(\delta p)}{\partial z} + \delta\rho g = 0, \tag{A.8}$$

and

$$\frac{\partial(\delta p)}{\partial t} + \boldsymbol{U}\cdot\nabla p_0 - C^2\frac{\partial(\delta\rho)}{\partial t} - C^2\boldsymbol{U}\cdot\nabla\rho_0 = 0. \tag{A.9}$$

To derive Eq. (A.9) from Eq. (A.3), we use the total time derivative

$$\frac{d}{dt} = \frac{\partial}{\partial t} + \boldsymbol{U}\cdot\nabla. \tag{A.10}$$

This equation yields the time rate of change of a quantity moving with the flow of neutrals. Solutions of the set of Eqs. (A.6)-(A.9) may be found in complex Fourier form as

$$\delta\rho/\rho_0, \delta p/p_0, v, w \quad \propto \quad exp\, i(\omega t - k_y y - k_z z), \tag{A.11}$$

where ω is the angular frequency of the wave, and k is the wave number. Using Eq. (A.11), the condition for hydrostatic equilibrium, and the expression for the scale height H, Eqs. (A.6)-(A.9) can be rewritten as a matrix equation:

$$\begin{pmatrix} i\omega & 0 & -ik_y & -1/H - ik_z \\ 0 & -ik_y C^2/\gamma & i\omega & 0 \\ g & -C^2(1/H + ik_z)/\gamma & 0 & i\omega \\ -i\omega C^2 & i\omega C^2/\gamma & 0 & (\gamma-1)g \end{pmatrix} \cdot \begin{pmatrix} \delta\rho/\rho_0 \\ \delta p/p_0 \\ v \\ w \end{pmatrix} = 0. \tag{A.12}$$

Setting the determinant of the 4×4 matrix equal to zero yields the dispersion relation of wave,

$$\omega^4 - \omega^2 C^2(k_y^2 + k_z^2) + (\gamma-1)g^2 k_y^2 + i\gamma g\omega^2 k_z = 0. \tag{A.13}$$

If there are no sources of energy of dissipation, which is equivalent to ignoring the viscosity, waves will not grow or decay in time at a fixed point in space so we can assume ω is purely real. If we include gravity, there are no solutions of Eq. (A.13) with both k_y and k_z purely real and different from zero. If we assume that a wave does not attenuate as it propagates horizontally, we can obtain the solutions of Eq. (A.13) with k_y and k_z real:

$$\omega^4 - \omega^2 C^2(k_y^2 + k_z^2) + (\gamma-1)g^2 k_y^2 - \gamma^2 g^2\omega^2/4C^2 = 0. \tag{A.14}$$

Eq. (5.9) can be obtained from this equation.

Appendix B

Scattering from an ionospheric plasma

B.1 Thomson scattering

Thomson scattering is the process in which incident electromagnetic energy is scattered by the free electrons in the ionosphere. The cross-section of the scattering of a free electron, σ_T, is approximated by

$$\sigma_T = 4\pi r_e^2, \tag{B.1}$$

as defined in terms of an equivalent spherical scattering target, where r_e is the effective radius of the electron; r_e is about 2.8×10^{-15} m thus σ_T is about 6×10^{-29} m^2.

If the electron density is 10^{11} m^{-3} in a scattering volume of about 6×10^{11} m^3 (a cylinder with a radius of 3 km and a height of 22 km), the total cross-section of scattering becomes about 3.6×10^{-6} m^2. This is equivalent to a circle with a radius of about 1 mm. In the lower ionosphere, the electron density decreases with height, reaching about 10^{10} m^{-3} in the *D*-region. In this case, the radius for a round target is about 0.04 mm.

B.2 Spectra

In the early days of the application of Thomson scattering to radar technology for observations of the ionosphere, random thermal motions of electrons were considered to scatter signals with a wide variety of Doppler shifts. However, the bandwidths of observed echoes were considerably more narrow than had been expected because scattering from the ions in the plasma narrowed the effective spectrum width [*Bowles*, 1958].

In the ionosphere, the difference between the ion and electron temperatures increases with height. The ion acoustic velocity increases with the ratio T_e/T_i. This indicates that the

component of the spectrum due to ions will have a double-humped shape. Figure B.1 shows the dependence of this ionic spectral component on the ratio T_e/T_i [*Evans*, 1969].

IS radar can directly provide four important parameters that describe the ionosphere – electron density, electron and ion temperatures, and ion velocity along the field-of-line – with excellent height resolution. The IS spectrum depends on all of these parameters. The echo power P_s is proportional to the electron density. The shape of the IS spectrum is controlled by the temperatures of electrons and ions. The Doppler shift of the IS spectrum gives a bulk plasma drift along the line-of-sight.

The electron density at an altitude z is expressed as [*Evans*, 1969]

$$N_e(z) = Const.\frac{P_s\ z^2}{\sigma_R(z)}, \tag{B.2}$$

where σ_R is the scattering cross-section. When the electrons and ions are at different temperatures, σ_R is given by

$$\sigma_R(z) = \frac{\sigma_e}{(1+\alpha(z))(1+T_e(z)/T_i(z)+\alpha(z)^2)}, \tag{B.3}$$

where σ_e is the radar cross section of an electron, and α is the ratio of the Debye length to the wavelength of the radio wave. The constant of proportionality can be estimated directly by careful determination of the radar parameters, or indirectly using some other instrument such as an ionosonde to make an absolute determination of the electron density. The radar wavelength of the EISCAT radar ($\simeq$ 0.3 m) is much longer than the Debye length in the ionosphere, so Eq. (B.3) can be modified to

$$\sigma_R(z) = \frac{\sigma_e}{1+T_e(z)/T_i(z)}. \tag{B.4}$$

The ion and electron temperatures can be determined using a least-squares fit of the theoretical spectrum to the observed one, and the electron density can thus be obtained from Eq. (B.2). The ratio T_e/T_i in the lower ionosphere (< 90 km) is thought to be $\simeq$1, so the electron density can be estimated independently on the ion and electron temperatures.

If there is an overall drift of electrons and ions towards the transmitter site at a velocity of v_d, the observed Doppler shift with a radar wavelength λ_R will be

$$\Delta f_d = \frac{2v_d}{\lambda_R}. \tag{B.5}$$

If the electrons and ions are drifting away from the transmitter site, the sign of Δf_d will be negative. The Doppler shift does not alter the shape of the IS spectrum. If, however, the ions are moving relative to the electrons, the IS spectrum becomes asymmetric (Fig. B.2) [*Lamb*, 1962].

Figure B.1: *Dependence of the ionic spectrum on T_e/T_i (after Evans, 1969).*

Figure B.2: *Spectra for different values of the ratio of the drift velocity v_d to the mean thermal velocity of the electrons (after Lamb, 1962).*

Appendix C

Theoretical fringe profile

Consider planar waves successively reflected between plane parallel surfaces S1 and S2 shown in Fig. C.1. The incident ray i with unit amplitude represents the direction of propagation of the incident planar wave and θ is the angle of incidence of the beams on the surfaces within the space between the surfaces (the interspace). The effective refractive index of the interspace is μ, and we suppose the light to have a wavelength of λ_0 in a vacuum. We consider the sets of successively reflected waves a, b, c,... and transmitted waves α, β, γ,... shown in Fig. C.1. The surface reflection and transmission coefficients for an incident ray travelling from left to right are labeled $+$, and those for an incident ray travelling right to left are labeled $-$. The optical delay for successive reflections gives an additional phase difference, which, for adjacent members of each set, obviously corresponds to a double passage through the interspace. The phase lag φ is given by

$$\varphi = 2\pi(2\mu d \cos\theta)/\lambda_0. \tag{C.1}$$

Both sets of beams form a geometrical progression with the same factor $r_1^-\ r_2^+ e^{i\varphi}$, with the exception of the first reflection. The amplitude $E_t(m)$ of the resultant electric field vector of the light first transmitted, m, is given by

$$E_t(m) = t_1^+ t_2^+ \left\{1 + r_1^- r_2^+ e^{i\varphi} + \cdots + \left(r_1^- r_2^+ e^{i\varphi}\right)^{m-1}\right\}. \tag{C.2}$$

For an infinite number of beams as, *i.e.* $m \to \infty$, this becomes

$$E_t(m\to\infty) = \frac{t_1^+ t_2^+}{1 - r_1^- r_2^+ e^{i\varphi}}. \tag{C.3}$$

The corresponding transmitted intensity I_t is found from the square modulus $E_t E_t^*$:

$$I_t = \frac{|t_1^+ t_2^+|^2}{1 + |r_1^- r_2^+|^2 - 2|r_1^- r_2^+| \cos\psi}, \tag{C.4}$$

where $\psi = \varphi + \epsilon$, and ϵ is given by

Figure C.1: *Planar waves being successively reflected back and forth between two planar parallel surfaces.*

$$\epsilon = arg\ r_1^- + arg\ r_2^+. \tag{C.5}$$

For a single surface, coefficients for the intensity of reflection and transmission by the surface, R and T respectively, may be summarized by

$$T = t_1^+ t_2^+, \qquad R = |r^+|^2 = |r^-|^2, \quad and \qquad R + T = 1. \tag{C.6}$$

Substituting these into Eq. (C.4), we obtain

$$\begin{aligned} I_t &= \frac{T^2}{1 + R^2 - 2R\ cos\ \phi} \\ &= (\frac{T}{1-R})^2 \left\{1 + F sin^2(\phi/2)\right\}^{-1} \\ &= (\frac{T}{1-R})^2 A(\phi), \end{aligned} \tag{C.7}$$

where F is given by $4R/(1\text{-}R)^2$ and $A(\phi)$ is the Airy function. The periodic form of the fringes arises from the Airy function, as shown in Fig. C.2.

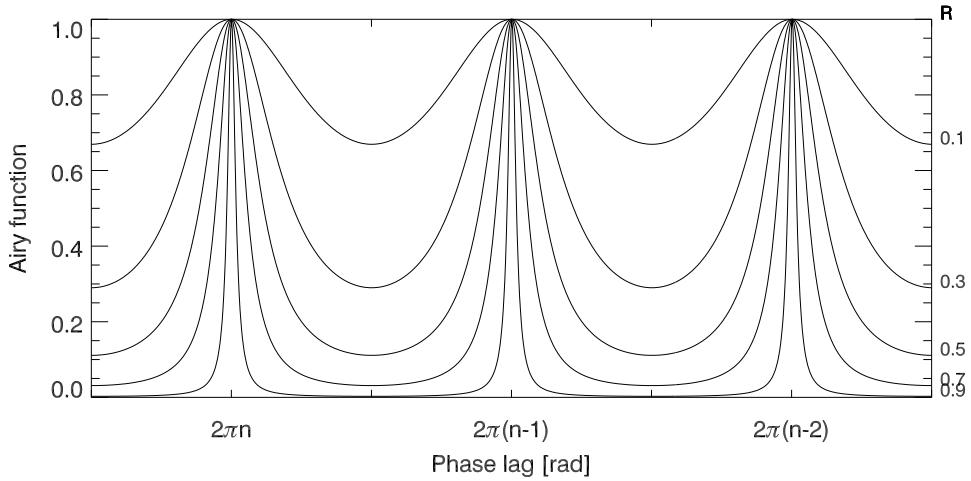

Figure C.2: *Fringe profiles for $A(\phi)$ at various values of R.*

References

[1] Abe, T., Whalen, B. A., Yau, A. W., Horita, R. E., Watanabe, S., and Sagawa, E., EXOS D (Akebono) suprathermal mass spectrometer observations of the polar wind, *J. Atmos. Solar-Terr. Phys.*, **98**, 11,191-11,203, 1993.

[2] Aruliah, A. L., A. D. Farmer, and D. Rees, The seasonal behavior of high-latitude thermospheric winds and ion velocities observed over one solar cycle, *J. Geophys. Res.*, **101**, 15,701-15,711, 1996.

[3] Avery, S. K., R. A. Vincent, A. Phillips, A. H. Manson, and G. J. Fraser, High-latitude tidal behavior in the mesosphere and lower thermosphere, *J. Atmos. Solar-Terr. Phys.*, **51**, 595-608, 1989.

[4] Balthazor, R. L., R. J. Moffett, and G. H. Millward, A study of the Joule and Lorentz inputs in the production of atmospheric gravity waves in the upper thermosphere, *Ann. Geophysicae*, **15**, 779-785, 1997.

[5] Banks, P. M., Observations of joule and particle heating in the auroral zone, *J. Atmos. Terr. Phys.*, **39**, 179-193, 1977.

[6] Baron, M. J., and R. H. Wand, F region ion temperature enhancements resulting from Joule heating, *J. Geophys. Res.*, **88**, 4114-4118, 1983.

[7] Bertin, F., J. Testud, and L. Kersley, Medium scale gravity waves in the ionospheric F-region and their possible origin in weather disturbances, *Planet. Space Sci.*, **23**, 493-507, 1975.

[8] Bertin, F., W. Kofman, and G. Lejeune, Observations of gravity waves in the auroral zone, *Radio Sci.*, **18**, 1059-1065, 1983.

[9] Bowles, K. L., Observations of vertical incidence scatter from the ionosphere at 41 Mc/sec, *Phys. Rev. Lett.*, **1**, 454-455, 1958.

[10] Brekke, A., On the relative importance of Joule heating and the Lorentz force in generating atmospheric gravity waves and infrasound waves in the auroral electrojets, *J. Atmos. Terr. Phys.*, **41**, 475-479, 1979.

[11] Brekke, A., C. Hall, and T. L. Hansen, Auroral ionospheric conductances during disturbed conditions, *Ann. Geophysicae*, **7**, 269-280, 1989.

[12] Bristow, W. A. and R. A. Greenwald, Identification of high-latitude acoustic gravity wave sources using the Goose Bay HF radar, *J. Geophys. Res.*, **99**, 319-331, 1994.

[13] Bristow, W. A. and R. A. Greenwald, Multiradar observations of medium-scale acoustic gravity waves using the Super Dual Auroral Radar Network, *J. Geophys. Res.*, **101**, 24,499-24,511, 1996.

[14] Chimonas, G. and C. O. Hines, Atmospheric gravity waves launched by auroral currents, *Planet. Space Sci.*, **18**, 565-582, 1970.

[15] Conde, M. and P. L. Dyson, Thermospheric vertical winds above Mawson, Antarctica, *J. Atmos. Terr. Phys.*, **57**, 589-596, 1995.

[16] Dickinson, R. E., E. C. Ridley, and R. G. Roble, Thermospheric general circulation with coupled dynamics and composition, *J. Atmos. Sci.*, **41**, 205-219, 1984.

[17] Elphinstone, R. D., J. S. Murphree, and L. L. Cogger, What is a global auroral substorm?, *Rev. Geophys.*, **34**, 169-232, 1996.

[18] Evans, J. V., Theory and practice of ionosphere study by Thomson scatter radar, *Proc. IEEE*, **57**, 496-530, 1969.

[19] Evans, J. V., J. M. Holt, and R. H. Wand, A differential-Doppler study of traveling ionospheric disturbances from Millstone Hill, *Radio Sci.*, **18**, 435-451, 1983.

[20] Folkestad, K., T. Hagfors, and S. Westerlund, EISCAT: An updated description of technical characteristics and operational capabilities, *Radio Sci.*, **18**, 867-879, 1983.

[21] Francis, S. H., A theory of medium-scale traveling ionospheric disturbances, *J. Geophys. Res.*, **79**, 5245-5260, 1974.

[22] Fujii, R., S. Nozawa, S. C. Buchert, N. Matuura, and A. Brekke, The motion of ions in the auroral ionosphere, *J. Geophys. Res.*, **103**, 20,685-20,695, 1998.

[23] Fujiwara, H., S. Maeda, H. Fukunishi, T. J. Fuller-Rowell, and D. S. Evans, Global variations of thermospheric winds and temperatures caused by substorm energy injection, *J. Geophys. Res.*, **101**, 225-239, 1996.

[24] Garcia, R. and S. Solomon, The effect of breaking gravity waves on the dynamics and chemical composition of the mesosphere and lower thermosphere, *J. Geophys. Res.*, **90**, 3850-3868, 1985.

[25] Hajkowicz, L. A. and R. D. Hunsucker, A simultaneous observation of large-scale periodic tides in both hemispheres following an onset of auroral disturbances, *Planet. Space Sci.*, **35**, 785-791, 1987.

[26] Hedin, A. E., Extension of the MSIS thermosphere model into the middle and lower atmosphere, *J. Geophys. Res.*, **96**, 1159-1172, 1991.

[27] Hernandez, G., Time series, periodograms, and significance, *J. Geophys. Res.*, **104**, 10,355-10,368, 1999.

[28] Hines, C. O., Internal atmospheric gravity waves at ionospheric heights, *Can. J. Phys.*, **38**, 1441-1481, 1960.

[29] Hunsucker, R. D., Atmospheric gravity waves generated in the high-latitude ionosphere: A review, *Rev. Geophys. Space Phys.*, **20**, 293-315, 1982.

[30] Innis, J. L., P. L. Dyson, and P. A. Greet, Further observations of the thermospheric vertical wind at the auroral oval/polar cap boundary, *J. Atmos. Terr. Phys.*, **59**, 2009-2022, 1997.

[31] Ishii, M., S. Okano, E. Sagawa, S. Watari, H. Mori, I. Iwamoto, and Y. Murayama, Development of Fabry-Perot Interferometers for airglow observations, *Proc. NIPR symp. Upper Atmos. Physics*, **10**, 97-108, 1997.

[32] Jing, N. and R. D. Hunsucker, A theoretical investigation of sources of large and medium scale atmospheric gravity waves in the auroral oval, *J. Atmos. Terr. Phys.*, **55**, 1667-1679, 1993.

[33] Johnson, R. M., V. B. Wickwar, R. G. Roble, and J. G. Luhmann, Lower-thermospheric winds at high latitude: Chatanika radar observations, *Ann. Geophysicae*, **5A**, 383-404, 1987.

[34] Johnson, R. M. and T. S. Virdi, High-latitude lower thermospheric neutral winds at EISCAT and Sondrestrom during LTCS 1, *J. Geophys. Res.*, **96**, 1099-1116, 1991.

[35] Johnson, F. S., W. B. Hanson, R. R. Hodges, W. R. Coley, G. R. Carignan, and N. W. Spencer, Gravity waves near 300 km over the polar caps, *J. Geophys. Res.*, **100**, 23,993-24,002, 1995.

[36] Kato, S., T. Kawakami, and D. St. John, Theory of gravity wave emission from moving sources in the upper atmosphere, *J. Atmos. Terr. Phys.*, **39**, 581-588, 1977.

[37] Killeen, T. L. and R. G. Roble, An analysis of the high-latitude thermospheric wind pattern calculated by a thermospheric general circulation model, *J. Geophys. Res.*, **89**, 7509-7522, 1984.

[38] Killeen, T. L. and R. G. Roble, Thermosphere dynamics: Contributions from the first 5 years of the Dynamics Explorer program, *Rev. Geophys.*, **26**, 329-367, 1988.

[39] Killeen, T. L. and R. G. Roble, Thermosphere dynamics: Contributions from the first 5 years of the Dynamics Explorer program, *Rev. Geophys.*, **26**, 329-367, 1998.

[40] Killeen, T. L., P. B. Hays, G. R. Carignan, R. A. Heelis, W. B. Hanson, N. W. Spencer, and L. H. Brace, Ion-neutral coupling in the high-latitude F region: Evaluation of ion heating terms from Dynamics Explorer 2, *J. Geophys. Res.*, **89**, 7495-7508, 1984.

[41] Killeen, T. L., R. A. Heelis, P. B. Hays, N. W. Spencer, and W. B. Hanson, Neutral motions in the polar thermosphere for northward interplanetary magnetic field, *Geophys. Res. Lett.*, **12**, 159-162, 1985.

[42] Killeen, T. L., F. G. McCormac, A. G. Burns, J. P. Thayer, R. M. Johnson, and R. J. Niciejewski, On the dynamics and composition of the high-latitude thermosphere, *J. Atmos. Terr. Phys.*, **53**, 797-815, 1991.

[43] Kirchengast, G., Characteristics of high-latitude TIDs from different causative mechanisms deduced by theoretical modeling, *J. Geophys. Res.*, **102**, 4597-4612, 1997.

[44] Lamb, G. L., The scattering of electromagnetic waves by non-equilibrium plasma, Los Alamos Sci. Lab., Los Alamos, N. Mex., Rept. LA 2715, 1962.

[45] Lathuillere, C., F. Glangeaud, and Z. Y. Zhao, Ionospheric ion heating by ULF Pc 5 magnetic pulsations, *J. Geophys. Res.*, **91**, 1619-1626, 1986.

[46] Lilensten, J., G. Thuillier, C. Lathuillere, W. Kofman, V. Fauliot, and M. Herse, EISCAT-MICADO coordinated measurements of meridional wind, *Ann. Geophysicae*, **10**, 603-618, 1992.

[47] Lilensten, J. and C. Lathuillere, The meridional thermospheric neutral wind measured by the EISCAT radar, *J. Geomag. Geoelectr.*, **47**, 911-920, 1995.

[48] Lühr, H., A. Aylward, S. C. Buchert, A. Pajunpää, K. Pajunpää, T. Holmboe, and S. M. Zalewski, Westward moving dynamic substorm features observed with the IMAGE magnetometer network and other ground-based instruments, *Ann. Geophysicae*, **16**, 425-440, 1998.

[49] Manson, A. H., J. B. Gregory, and C. E. Meek, Atmospheric waves (> 10 min-30 days) in the mesosphere and thermosphere at Saskatoon (52° N, 107° W), October 1978-September 1979, *Planet. Space Sci.*, **29**, 615-625, 1981.

[50] Manson, A. H. and C. E. Meek, Winds and tidal oscillations in the upper middle atmosphere at Saskatoon (52° N, 107° W, L=4.3) during the year June 1982-May 1983, *Planet. Space Sci.*, **32**, 1087-1099, 1984.

[51] Manson, A. H., C. E. Meek, H. Teitelbaum, F. Vial, R. Schminder, D. Kurschner, M. J. Smith, G. J. Fraser, and R. R. Clark, Climatologies of semi-diurnal and diurnal tides in the middle atmosphere (70-110 km) at middle latitudes (40-55°), *J. Atmos. Solar-Terr. Phys.*, **51**, 579-593, 1989.

[52] McCormac, F. G., T. L. Killeen, E. Gombosi, P. B. Hays, and N. W. Spencer, Configuration of the high-latitude thermosphere neutral circulation for IMF B_y negative and positive, *Geophys. Res. Lett.*, **12**, 155-158, 1985.

[53] McLandress, C., On the importance of gravity waves in the middle atmosphere and their parameterization in general circulation models, *J. Atmos. Solar-Terr. Phys.*, **60**, 1357-1383, 1998.

[54] Meier, R. R., D. J. Strickland, J. H. Hecht, and A. B Christensen, Deducing composition and incident electron spectra from ground-based auroral optical measurements: A study of auroral red line processes, *J. Geophys. Res.*, **94**, 13,541-13,552, 1989.

[55] Nozawa, S. and A. Brekke, Studies of the auroral E region neutral wind through a solar cycle: Quiet days, *J. Geophys. Res.*, **104**, 45-66, 1999.

[56] Ogawa, T., K. Igarashi, K. Aikyo, and H. Maeno, NNSS satellite observations of medium-scale traveling ionospheric disturbances at southern high-latitudes, *J. Geomag. Geoelectr*, **39**, 709-721, 1987.

[57] Ogawa, Y., R. Fujii, S. C. Buchert, S. Nozawa, S. Watanabe, and A. P. van Eyken, Simultaneous EISCAT Svalbard and VHF radar observations of ion upflows at different aspect angles, *Geophys. Res. Lett.*, **27**, 81-84, 2000.

[58] Opgenoorth, H. J., I. Haggstorm, P. J. S. Williams, and G. O. L. Jones, Regions of strongly enhanced perpendicular electric fields adjacent to auroral arcs, *J. Atmos. Terr. Phys.*, **52**, 449-458, 1990.

[59] Oyama, S., S. Nozawa, S. C. Buchert, M. Ishii, S. Watari, E. Sagawa, W. Kofman, J. Lilensten, and R. Fujii, Effects of atmospheric oscillations on the field-aligned ion motions in the polar *F*-region, *Ann. Geophysicae*, **18**, 1145-1153, 2000.

[60] Price, G. D., R. W. Smith, and G. Hernandez, Simultaneous measurements of large vertical winds in the upper and lower thermosphere, *J. Atmos. Terr. Phys.*, **57**, 631-643, 1995.

[61] Rees, D., N. Lloyd, P. J. Charleton, M. Carlson, J. Murdin, and I. Haggstrom, Comparison of plasma flow and thermospheric circulation over northern Scandinavia using EISCAT and a Fabry-Perot interferometer, *J. Atmos. Solar-Terr. Phys.*, **46**, 545-565, 1984.

[62] Rees, D., T. J. Fuller-Rowell, R. Gordon, J. P. Heppner, N. C. Maynard, N. W. Spencer, L. E. Wharton, P. B. Hays, and T. L. Killeen, A theoretical and empirical study of the response of the high-latitude thermosphere to the sense of the "Y" component of the interplanetary magnetic field, *Planet. Space Sci.*, **34**, 1-40, 1986.

[63] Rees, M. H., Auroral ionization and excitation by incident energetic electrons, *Planet. Space Sci.*, **11**, 1209-1218, 1963.

[64] Richmond, A. D. and S. Matsushita, Thermospheric response to a magnetic substorm, *J. Geophys. Res.*, **80**, 2839-2850, 1975.

[65] Rino, C. L., A. Brekke, and M. J. Baron, High-resolution auroral zone E region neutral wind and current measurements by incoherent scatter radar, *J. Geophys. Res.*, **82**, 2295-2304, 1977.

[66] Roble, R. G., R. E. Dickinson, and E. C. Ridley, Seasonal and solar cycle variations of the zonal mean circulation in the thermosphere, *J. Geophys. Res.*, **82**, 5493-5504, 1977.

[67] Roble, R. G. and B. A. Emery, On the global mean temperature of the thermosphere, *Planet. Space Sci.*, **6**, 597-614, 1983.

[68] Samson, J. C., R. A. Greenwald, J. M. Ruohoniemi, A. Frey, and K. B. Baker, Goose Bay radar observations of earth-reflected, atmospheric gravity waves in the high-latitude ionosphere, circulation in the thermosphere, *J. Geophys. Res.*, **95**, 7693-7709, 1990.

[69] Smith, R. W. and P. J. Sweeney, Winds in the thermosphere of the northern polar cap, *Nature*, **284**, 437-438, 1980.

[70] Smith, R. W., and G. Hernandez, Vertical winds in the thermosphere within the polar cap, *J. Atmos. Terr. Phys.*, **57**, 611-620, 1995.

[71] Smith, R. W., Vertical winds: a tutorial, *J. Atmos. Solar-Terr. Phys.*, **60**, 1425-1434, 1998.

[72] Sofko, G. J. and C. S. Huang, SuperDARN observations of medium-scale gravity wave pairs generated by Joule heating in the auroral zone, *Geophys. Res. Lett.*, **27**, 485-488, 2000.

[73] Spencer, N. W., L. E. Wharton, G. R. Carignan, and J. C. Maurer, Thermosphere zonal winds, vertical motions and temperature as measured from Dynamics Explorer, *Geophys. Res. Lett.*, **9**, 953-956, 1982.

[74] Strickland, D. J., D. L. Book, T. P. Coffey, and J. A. Fedder, Transport equation techniques for the deposition of auroral electrons, *J. Geophys. Res.*, **81**, 2755-2764, 1976.

[75] Strickland, D. J., R. R. Meier, J. H. Hecht, and A. B. Christensen, Deducing composition and incident electron spectra from ground-based auroral optical measurements: Theory and model results, *J. Geophys. Res.*, **94**, 13,527-13,539, 1989.

[76] Sun, Z. P., R. P. Turco, R. L. Walterscheid, S. V. Venkateswaran, and P. W. Jones, Thermospheric three-dimensional simulations, *J. Geophys. Res.*, **100**, 23,779-23,793, 1995.

[77] Swift, D. W., The generation of infrasonic waves by auroral electrojets, *J. Geophys. Res.*, **78**, 8205-8221, 1973.

[78] Tetenbaum, D., S. K. Avery, and A. C. Riddle, Observations of mean winds and tides in the upper mesosphere during 1980-1984, using the Poker Flat, Alaska, MST radar as a meteor radar, *J. Geophys. Res.*, **91**, 14,539-14,555, 1986.

[79] Thayer, J. P., T. L. Killeen, F. G. McCormac, C. R. Tschan, J.-J. Ponthieu, N. W. Spencer, Thermospheric neutral wind signatures dependent on the east-west component of the interplanetary magnetic field for northern and southern hemispheres as measured from Dynamics Explorer-2, *Ann. Geophysicae*, **5A**, 363-368, 1987.

[80] Thuillier, G., C. Lathuillere, M. Herse, C. Senior, W. Kofman, M. L. Duboin, D. Alcayde, F. Barlier, and J. Fontanari, Co-ordinated EISCAT-MICADO interferometer measurements of neutral winds and temperatures in *E*- and *F*-regions, *J. Atmos. Terr. Phys.*, **52**, 625-636, 1990.

[81] Walterscheid, R. L. and L. R. Lyons, The neutral circulation in the vicinity of a stable auroral arc, *J. Geophys. Res.*, **97**, 19,489-19,499, 1992.

[82] Wedde, T., J. R. Doupnik, and P. M. Banks, Chatanika observations of the latitudinal structure of electric fields and particle precipitation on November 21, 1975, *J. Geophys. Res.*, **82**, 2743-2751, 1977.

[83] Whiteway, J. A., T. J. Duck, D. P. Donovan, J. C. Bird, S. R. Pal, and A. I. Carswell, Measurements of gravity wave activity within and around the arctic stratospheric vortex, *Geophys. Res. Lett.*, **24**, 1387-1390, 1997.

[84] Wickwar, V. B., J. W. Meriwether, Jr. P. B. Hays, and A. F. Nagy, The meridional thermospheric neutral wind measured by radar and optical techniques in the auroral region, *J. Geophys. Res.*, **89**, 10,987-10,998, 1984.

[85] Williams, P. J. S., G. Crowley, K. Schlegel, T. S. Virdi, I. McCrea, G. Watkins, N. Wade, J. K. Hargreaves, T. Lachlan-Cope, H. Muller, J. E. Baldwin, P. Warner, A. P. van Eyken, M. A. Hapgood, and A. S. Rodger, The generation and propagation of atmospheric gravity waves observed during the Worldwide Atmospheric Gravity-wave Study (WAGS), *J. Atmos. Terr. Phys.*, **50**, 323-338, 1988.

[86] Wilson, C. R., Auroral infrasonic wave-generation mechanism, *J. Geophys. Res.*, **77**, 1820-1843, 1972.

[87] Winser, K. J., A. D. Farmer, D. Rees, and A. Aruliah, Ion-neutral dynamics in the high latitude ionosphere: first results from the INDI experiment, *J. Atmos. Terr. Phys.*, **50**, 369-377, 1988.

[88] Witasse, O., J. Lilensten, C. Lathuillere, and B. Pibaret, Meridional thermospheric neutral wind at high latitude over a full solar cycle, *Ann. Geophysicae*, **16**, 1400-1409, 1998.

[89] Yau, A. W. and M. André, Sources of ion upflow in the high latitude ionosphere, *Space Sci. Rev.*, **80**, 1-25, 1997.